Sensitivity to anomalous triple gauge couplings in the $W\gamma$ channel and a calibration study on the level-1 calorimeter trigger of the ATLAS detector

John Richard Alan Booth

Thesis submitted for a degree of Doctor of Philosophy

Particle Physics Group,
School of Physics and Astronomy,
University of Birmingham.

February, 2008.

Synopsis

Reported in this thesis are tests carried out on the ATLAS level-1 calorimeter trigger, a description of a prototype calibration mechanism for a module in the the ATLAS level-1 calorimeter trigger and a physics analysis based on the ATLAS detector.

The installation of the ATLAS level-1 calorimeter trigger is almost complete. The collection of hardware that it is composed of has undergone rigorous testing by a variety of institutes. Part of the hardware built and tested at Birmingham was the cluster processor module. Detailed here is how the cluster processor module and one of its daughter modules was affected by temperature.

Due to the need to calibrate the level-1 calorimeter trigger hardware for successful trigger operation a prototype calibration mechanism for the common merger module was developed. This prototype is described here.

Anomalous triple gauge couplings will be constrained at ATLAS through a variety of physics channels. Of interest here is how well the sensitivity to the $\Delta\kappa_\gamma$ and λ_γ coupling, arising from the $WW\gamma$ vertex in the $W\gamma$ channel, could be measured. This was a Monte Carlo study using data corresponding to a luminosity of 0.5 fb^{-1} and where the W could decay leptonically to electron or muon flavours.

Author's Contribution

Several years before my Ph.D began the ATLAS detector was being designed and constructed by many collaborators. Throughout the course of my Ph.D, due to the highly collaborative nature of ATLAS, direct and indirect input was received from many collaborators. I therefore acknowledge that although the work presented in this thesis is my own, it was only possible because of the aforementioned. I now make explicit the work I was responsible for.

The construction, installation and running of the level-1 calorimeter trigger is being undertaken by several institutes. While working in this local collaboration I carried out two experiments to measure how temperature effects the electronics. For this work I am indebted to the people who built the hardware and software systems. I also undertook the role of implementing a prototype calibration package for one module in the system. This involved investigating the possibilities and writing the analysis code to implement it within the already existing software framework. The results of this work are detailed in chapter 4.

In the physics analysis contained herein I generated and fully simulated all the signal $W\gamma$ datasets. In order to do this I had to make substantial use of the distributed computing facilities available to ATLAS. I am also grateful to the SHERPA authors for implementing the anomalous triple gauge coupling model. The results from my analysis in chapters 6 and 7 originate from code written by myself, but without the 'ROOT' or 'ATHENA' developers this work would not have been possible.

Acknowledgements

I would like to thank Dave Charlton and Norman Gee for the guidance and supervision that I received throughout my PhD.

My time at Birmingham and RAL has been made enjoyable by many people and I would especially like to thank those that I have shared an office with. Finally I would like to thank Juergen Thomas for the friendly and frequent discussions (on physics to politics) that have livened up the office.

Contents

List of Figures

List of Tables

Chapter 1

Introduction

One of the attributes of the human civilisation is its continuing curiosity of how nature works. Part of this curiosity has been focused towards the seemingly basic question of what is the fundamental structure of matter. Perhaps the earliest documented answer to this question is by the ancient Greeks who proposed that the core elements that made up the world were earth, fire, air and water. Scientific advancement over the two and a half millennia since the ancient Greeks' prediction have shown us that the fundamental structure of matter is far more complex than this. The current status of our understanding of matter is built upon several decades of experimentation and theory in the field of high energy particle physics and has resulted in a theory known as the Standard Model. A more detailed description of this theory is discussed in chapter 2.

A new experimental facility called the Large Hadron Collider (LHC) will soon allow the accuracy of the Standard Model to be tested to an unprecedented level and thus further probe the structure of matter. The LHC is a particle accelerator that operates by colliding protons together at a centre of mass energy of 14 TeV. By using a high centre of mass energy the LHC should enable rare processes, that are not observed at lower centre of mass energies, to be observed. These processes

can subsequently be studied in the four detectors that are located around the LHC. This Ph.D was based on one of the four detectors of the LHC, called ATLAS.

Substantial time throughout the Ph.D was spent on the two different topics that will now be briefly described. The first topic was related to work carried out on the ATLAS level-1 calorimeter trigger while the second was a physics study on $W\gamma$ anomalous triple gauge couplings.

The work detailed on the level-1 calorimeter trigger was done during a time of rapid building and installation of the trigger systems. As a result the main work was on the development of a prototype calibration mechanism for one of the pieces of hardware. In addition to this, testing of some of the timing critical hardware was undertaken.

Anomalous triple gauge couplings in the $W\gamma$ channel have been studied in the past at ATLAS (1; 2; 3). However, the most comprehensive of these studies was at the level of a fast simulation (2). The study undertaken here has tried to improve the accuracy with which a prediction can be made on the anomalous couplings by performing a full simulation for the signal and relevant backgrounds. This is of importance as a full simulation allows a more detailed modelling of how the particles interact. This study also differs from previous ones in that it is probing the anomalous couplings with an amount of data that corresponds to a short period of the experiment's running.

The differing subject matter described in this thesis does not lend itself to creating a continuous piece of prose. A brief outline of this thesis is therefore given to explain when the different topics are discussed. In order to give a general overview of triple gauge couplings their theory is first discussed. After this a description of the ATLAS detector is given as it is the basis of the physics measurement and hardware work. As the work connected to the level-1 calorimeter was heavily based on the hardware it is natural at this point to describe it. The remaining chapters detail

the work done for the analysis of anomalous triple gauge couplings.

Chapter 2

Theory

In this chapter a description of the Standard Model is given as it is the basis of current experimental particle physics. After the necessary physics has been introduced a review of the phenomenology of triple gauge couplings relevant to the $W\gamma$ channel is made.

2.1 The Standard Model

The Standard Model (SM) is the currently accepted model of particle physics that predominantly provides a description of how matter interacts (4). The types of matter observed so far are the three generations of quarks and leptons (5). The Standard Model proposes that these quarks and leptons can interact through the exchange of an intermediary particle. From experimental observations three differing types of interaction occur - the strong interaction that is mediated by the gluon; the weak interaction that is mediated by the W and Z bosons; and the electromagnetic interaction that is mediated by the photon. The ranges and properties of the various interactions are determined by the intermediary particles and their couplings to either matter or themselves. In the next few paragraphs a more detailed description

of these interactions is given so that the physics under study can be described appropriately.

A description of nuclear decay via the weak interaction was originally put forward by Fermi (6). Based on the decay process $n \rightarrow p + e + v$ Fermi proposed a theory based on a four fermion interaction vertex. However, the approach was flawed on the counts that the theory was non-renormalisable and that it violated unitarity at high energy[1]. To overcome these problems physicists turned to Yukawa theory (7), where the strong interaction was mediated by a boson, with the idea that the weak decay could also be mediated by a boson. By approaching the problem in this way physicists were able to overcome the unitarity problem and also determine that the mass of the boson would be approximately 50 to 100 GeV. However, even though this theory did predict the right mass range of the mediating particle it was not renormalisable. The solution to this problem came in the form of Weinberg-Salam theory (8) that overcame the problem of renormalisation and suggested the existence of the Z^0 boson in addition to the W^+ and W^- bosons. This explained the two types of weak interaction, 'charged currents' and 'neutral currents'. For charged current interactions the W boson (that has a charge of ± 1) can couple to a quark or lepton. The $W^{\pm}$ can then couple to a $l^{\pm}\nu$ pair or a $q_i\bar{q}_j$ pair as defined by the Cabibbo-Kobayashi-Maskawa (CKM) matrix (4). In neutral currents the neutral Z boson can couple to a quark pair ($q_i\bar{q}_i$) or a lepton pair ($l_i\bar{l}_i$). Experimental evidence from CERN in 1983 confirmed the existence of these particles and was an important test of the theory. The most important aspect of the Weinberg-Salam theory was that it allowed a combined description of the weak and electromagnetic forces. This was possible due to the non-abelian gauge structure at the core of the theory, by imposing local gauge invariance and applying the Higgs mechanism (9). The implementation

[1] A four fermion vertex is non-renormalisable because the interaction is accompanied by a dimensionful coupling constant. The unitarity violation can be seen when considering the differential cross section in the high energy regime of a weak s-wave process where $\frac{d\sigma}{d\Omega} \rightarrow \frac{G_F^2}{4\pi}s$. This contradicts unitarity where an s-wave process obeys $\frac{d\sigma}{d\Omega} \rightarrow \frac{1}{s}$.

of these steps is not discussed any further, however, it is important to discuss the various interactions between the photon, W^+, W^- and Z bosons that arise due to the non-abelian gauge theory. By considering a pure non-abelian gauge invariant Lagrangian (9) the interactions that form the basic structure of the electroweak theory can be defined:

$$L = \frac{1}{4g^2}\left[(\partial_\mu A^a_\nu - \partial_\nu A^a_\mu)^2 + f^{abc}A^{b\mu}A^{c\nu}(\partial_\mu A^a_\nu - \partial_\nu A^a_\mu) + (f^{abc}A^b_\mu A^c_\nu)^2\right]. \qquad (2.1)$$

The structure constant is 'f^{abc}' where abc take the numbers 1 to 3 respectively. The non-abelian four vector gauge field is 'A_μ' and '∂_μ' is a derivative. The Yang-Mills coupling constant is 'g'. The first term represents the propagation of a massless boson while the cubic and quartic terms (in powers of the field) represent the triple self-interaction and the quartic self-interaction of massless bosons. Importantly the structure constant 'f^{abc}' is fixed by the gauge structure and therefore the strength of the cubic and quartic interactions is fixed by symmetry (in the case of electroweak theory the SU(2)xU(1) symmetry). This is an incomplete description of electroweak theory as the Higgs mechanism (10) still needs to be applied to the massless gauge bosons in order to produce the photon, W^+, W^- and Z bosons that describe the physics we see. However, it is the overall consequence of the non-abelian gauge structure, as shown above, that specifies how the photon, W^+, W^- and Z bosons can couple at either a triple gauge boson vertex or quartic gauge boson vertex. As the triple self-interaction is the focus of the physics in this thesis the following sections detail its phenomenology and relevance to the $W\gamma$ channel.

Quantum Chromodynamics (QCD) is the name of the theory that describes the strong interaction (8). It is a "colour" interaction meaning that only quarks and gluons that carry colour charge feel it. The theory allows for the confinement of quarks and explains their asymptotic freedom at high energy. In this thesis the strong interaction is of importance because the experiment is based on a proton-proton collider and a lot of the underlying physics is therefore due to this interaction. Of particular relevance is that the proton is a composite particle made of quarks and

gluons. When two protons collide, as in the case of the LHC (11), it is some combination of these particles that are involved in the hard collision. These constituent particles will also only share a fraction of the energy/momentum of the proton and hence the reduced centre of mass energy $\sqrt{\hat{s}}$ that can be reached is lower than the proton-proton centre of mass energy $\sqrt{s}$. It should also be noted that it is not possible to know what $\sqrt{\hat{s}}$ is for an event as we only know the proton-proton centre of mass energy $\sqrt{s}$. This is regrettable as it is useful to apply energy and momentum conservation to understand the different kinematical processes. A solution to this problem is found by ignoring the longitudinal collision direction and examining the transverse components of energy and momentum that will balance to zero (as there was no transverse component in the initial state). Therefore when defining the beam pipe as the z-axis the transverse momentum P_T, transverse energy E_T, missing transverse energy E_T^{miss} and other transverse variables are defined in the x-y plane. The current understanding of which of the particles in the proton are most likely to be involved in a collision is described by the parton density functions (PDF) (12; 13; 14). These PDFs have been obtained by fitting theoretical predictions to experimental data. The uncertainties in the knowledge of the PDFs used in this study are discussed in section 7.5.2 as they will introduce a systematic uncertainty into this analysis.

2.2 Triple gauge couplings

Triple gauge couplings (TGC) describe the interaction of three gauge bosons. Depending on the charge of the vector bosons involved a further description of the coupling as either charged or neutral can be made. The charged type couplings must have two W bosons to maintain charge conservation. It is important to study both types of couplings to test the Standard Model (15). It is the charged type of coupling that is present in the $W\gamma$ channel and hence under study here (figure 2.1). The charged type couplings are predicted in the Standard Model and their

existence has already been proven by the LEP experiments (the results of which are examined in section 2.6). For reasons to be explained in the following sections the LHC will allow a more precise measurement of these couplings to be made and hence an improved test to see if they are correctly predicted by the Standard Model.

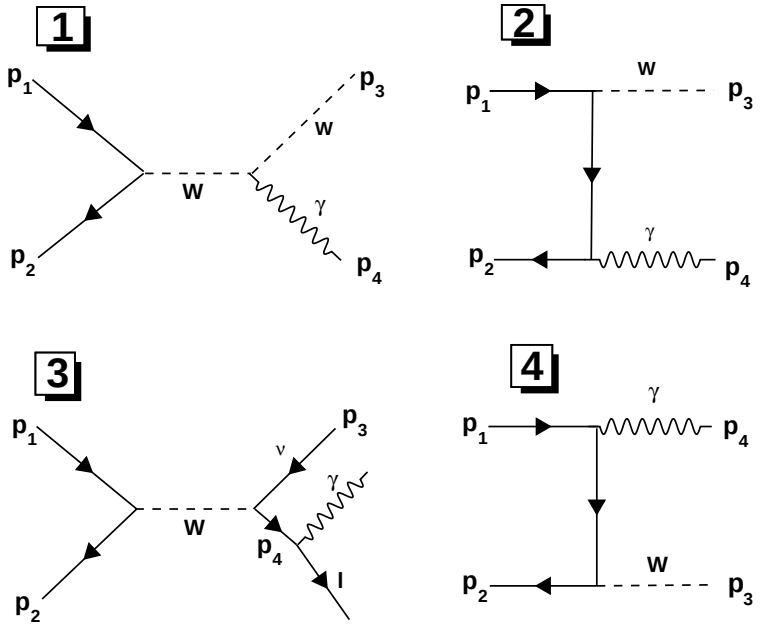

Figure 2.1: The Born level Feynman diagrams for the $W\gamma$ signal. These diagrams can be described in terms of the Mandelstam variables $s = (p_1 + p_2)^2$, $t = (p_1 - p_3)^2$ and $u = (p_1 - p_4)^2$ with p_i the momenta of the particle as labelled in the diagram. Diagram 1 is the s-channel process for $W\gamma$ production and contains the TGC vertex. The t and u channel processes are represented in diagrams 2 and 4. They do not contain the TGC vertex. Diagram 3, which also does not contain the TGC vertex, represents the production of a photon by radiation from a lepton.

2.2.1 Theory of anomalous triple gauge couplings

The $WW\gamma$ triple gauge coupling can be described most generally by the effective Lagrangian (16):

$$\begin{aligned} L_{WW\gamma}/g_{WW\gamma} =& i(1+\Delta g_1^\gamma)(W^\dagger_{\mu\nu}W^\mu A^\nu - W^\dagger_\mu A_\nu W^{\mu\nu}) + i(1+\Delta\kappa_\gamma)W^\dagger_\mu W_\nu A^{\mu\nu} \\ &+ \frac{i\lambda_\gamma}{M_W^2}W^\dagger_{\lambda\mu}W^\mu{}_\nu A^{\nu\lambda} - g_4^\gamma W^\dagger_\mu W_\nu(\partial^\mu A^\nu + \partial^\nu A^\mu) \\ &+ g_5^\gamma \epsilon^{\mu\nu\rho\sigma}(W^\dagger_\mu \overleftrightarrow{\partial_\rho} W_\nu)A_\sigma + i\tilde{\kappa}_\gamma W^\dagger_\mu W_\nu \tilde{A}^{\mu\nu} \\ &+ \frac{i\tilde{\lambda}_\gamma}{M_W^2}W^\dagger_{\lambda\mu}W^\mu_\nu \tilde{A}^{\nu\lambda}. \end{aligned} \tag{2.2}$$

In the above equation M_W is the W boson mass, $A^\mu (= A^{\mu\dagger})$ the photon field, W^μ the W field, $g_{WW\gamma} = -e$, $W_{\mu\nu} = \partial_\mu W_\nu - \partial_\nu W_\mu$, $A_{\mu\nu} = \partial_\mu A_\nu - \partial_\nu A_\mu$, $A\overleftrightarrow{\partial_\rho}B = A(\partial_\rho B) - (\partial_\rho A)B$, $\tilde{A}_{\mu\nu} = \frac{1}{2}\epsilon_{\mu\nu\rho\sigma}A^{\rho\sigma}$, $\epsilon_{\mu\nu\rho\sigma}$ in the Bjorken-Drell metric is $\epsilon_{0123} = -\epsilon^{0123} = +1$, and $\dagger$ represents the hermitian conjugate. The parameters Δg_1^γ, $\Delta\kappa_\gamma$, λ_γ, g_4^γ, g_5^γ, $\tilde{\kappa}_\gamma$ and $\tilde{\lambda}_\gamma$ are the anomalous couplings. Further explanation of the anomalous couplings and the extra kinematics that occur due to their inclusion is given in the following paragraphs. Most of this discussion is at a leading order approximation for simplicity. The necessary higher order effects are considered in section 2.3.

In the Standard Model all the anomalous couplings are zero. Some symmetries also suggest the value of some of the anomalous couplings should be zero. In order to obey electromagnetic gauge invariance the parameter $\Delta g_1^\gamma = 0$. It has been shown (16) that the parameters g_4^γ and g_5^γ are proportional to the photon four-momentum squared (P_γ^2) and are therefore zero for on shell photons in this channel, where the photons are final state particles. In this analysis a further simplifying assumption has been made to ignore the CP violating $\tilde{\kappa}_\gamma$ and $\tilde{\lambda}_\gamma$ anomalous couplings. This leaves the $\Delta\kappa_\gamma$ and λ_γ anomalous couplings that are studied here. Due to the inclusion of any anomalous couplings, electroweak gauge invariance is broken and the theory becomes non-renormalisable (16). The physical significance of these couplings has traditionally been described by their presence in the magnetic moment (μ_W) and

electric quadrupole moment (Q_W) of the W^+ (16), as shown:

$$\mu_W = \frac{e}{2M_W}(2 + \Delta\kappa_\gamma + \lambda_\gamma) \tag{2.3}$$

$$Q_W = \frac{e}{{M_W}^2}(1 + \Delta\kappa_\gamma - \lambda_\gamma). \tag{2.4}$$

The dynamics of the Lagrangian in equation (2.2) can be interpreted by examining the effect that the addition of anomalous triple gauge couplings has on the quantum mechanical matrix element amplitudes. The change in the quantum mechanical matrix elements ($\Delta M_{H_\gamma,H_W}$ where H_γ is the photon helicity and H_W is the W boson helicity) at leading order is (16; 17):

$$\Delta M_{\pm,0} = \frac{\sqrt{\hat{s}}}{2M_W}(\Delta\kappa_\gamma + \lambda_\gamma)\frac{1}{2}(1 \mp \cos\theta^\star_\gamma) \tag{2.5}$$

$$\Delta M_{\pm,\pm} = \left(\frac{\hat{s}}{2{M_W}^2}\lambda_\gamma + \frac{1}{2}\Delta\kappa_\gamma\right)\frac{1}{\sqrt{2}}\sin\theta^\star_\gamma. \tag{2.6}$$

In equations 2.5 and 2.6 the angle $\theta^\star_\gamma$ is the production angle in the parton centre of mass frame of the photon relative to the incoming quark. Several things are interesting to observe in the above equations. First of all, as the cross section for the process is proportional to the matrix element squared so the inclusion of anomalous couplings can increase the event rate. The behaviour at high $\sqrt{\hat{s}}$ also differs: the λ_γ coupling may have an enhancement up to $\frac{\hat{s}}{2M_W^2}$ while the $\Delta\kappa_\gamma$ coupling has an enhancement of at most $\frac{\sqrt{\hat{s}}}{2M_W}$. For both couplings the anomalous effects will start to be enhanced when the parton centre of mass energy $\sqrt{\hat{s}}$ is greater than the mass M_W. The dependence of the anomalous coupling sensitivity on the parton centre of mass energy will assist the LHC in probing them to a much higher level than lower energy colliders such as the Tevatron or LEP.

Another interesting feature in equation 2.6 is the role that $\sin\theta^\star_\gamma$ has when determining the anomalous couplings. As $\sin\theta^\star_\gamma$ is a maximum (at leading order) when perpendicular to the incoming beam, it implies that photons produced transverse to the beam (i.e. incoming quark direction) will be favoured. This is in the region that can be best measured by the detector (the "central region").

2.3 Higher order effects in the $W\gamma$ channel

At the LHC all the Feynman diagrams corresponding to $pp \rightarrow W\gamma + X$, where '$X$' represents every possible addition, will be involved. Due to practical limitations in describing all these diagrams the traditional approach of using Feynman diagrams up to a fixed order in the strong coupling constant (α_s) and electroweak coupling constant (α_{QED}) is used. The Born level diagrams, in figure 2.1, represent the lowest order of such diagrams with up to two electroweak vertices (hence of second order in α_{QED}). By using only these diagrams to predict the physics of $W\gamma$ events a basic description can be found. A more precise description is obtained by going to the next-to-leading order (NLO) as events can now contain more particles than just the $W\gamma$ bosons. The effect of increasing the electroweak order is a factor of 10 smaller on the $W\gamma$ cross section compared to increasing the strong order and it is thus the strong NLO correction that is of interest here (18). The NLO QCD corrections include all the Feynman diagrams which represent the virtual and real subprocesses.

For the case of studying anomalous triple gauge couplings in the $W\gamma$ channel it has been shown that a NLO calculation must be performed as the QCD corrections have a large impact in the same regions that the triple gauge couplings would appear (17). The principal reason for this effect is that the quark gluon fusion channel (figure 2.2) opens up when the photon transverse momentum is larger than the mass of the W boson ($P_T^{\gamma} >> M_W$) due to the cross section having a $ln^2[\frac{P_T^{\gamma 2}}{M_w^2}]$ enhancement. One of the consequences of the quark gluon fusion channel is that a high P_T photon is produced that can recoil against the quark, which can radiate an approximately collinear W boson. A simple generator level plot, shown in figure 2.3, illustrates all the NLO effects at LHC energies. Due to the quark gluon fusion channel not having a triple gauge coupling the QCD corrections do not enhance any anomalous feature and possibly even hide it.

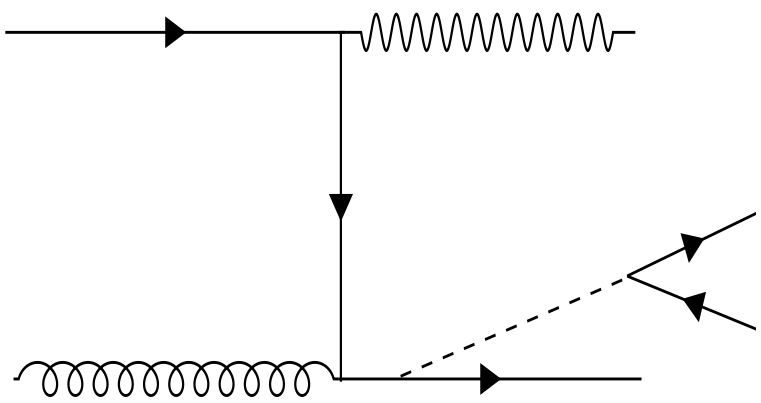

Figure 2.2: The quark gluon fusion channel Feynman diagram. The dashed line represents a W boson. The wavy line represents a photon. The looping line represents a gluon. The incoming solid line that flows out of the diagram on the right-hand side is a quark. The other two solid lines represent the decay products of the W boson and in this case are a lepton neutrino pair.

2.4 Observing anomalous triple gauge couplings

At ATLAS it is possible that the anomalous triple gauge couplings will either be observed to be non-zero or found to be consistent with the SM prediction. In order to make that evaluation, event properties that are sensitive to anomalous triple gauge couplings must be studied. By using the features described in the previous section this can be done and several methods are explained here.

2.4.1 Event rate

The most simple method to observe anomalous triple gauge couplings is to apply selection cuts to the event sample and to try to observe a difference between the numbers of events observed and predicted by theory in the $W\gamma$ channel. Should an anomalous coupling be non-zero a difference from the SM prediction would be expected as the matrix elements have been modified and the cross section for the

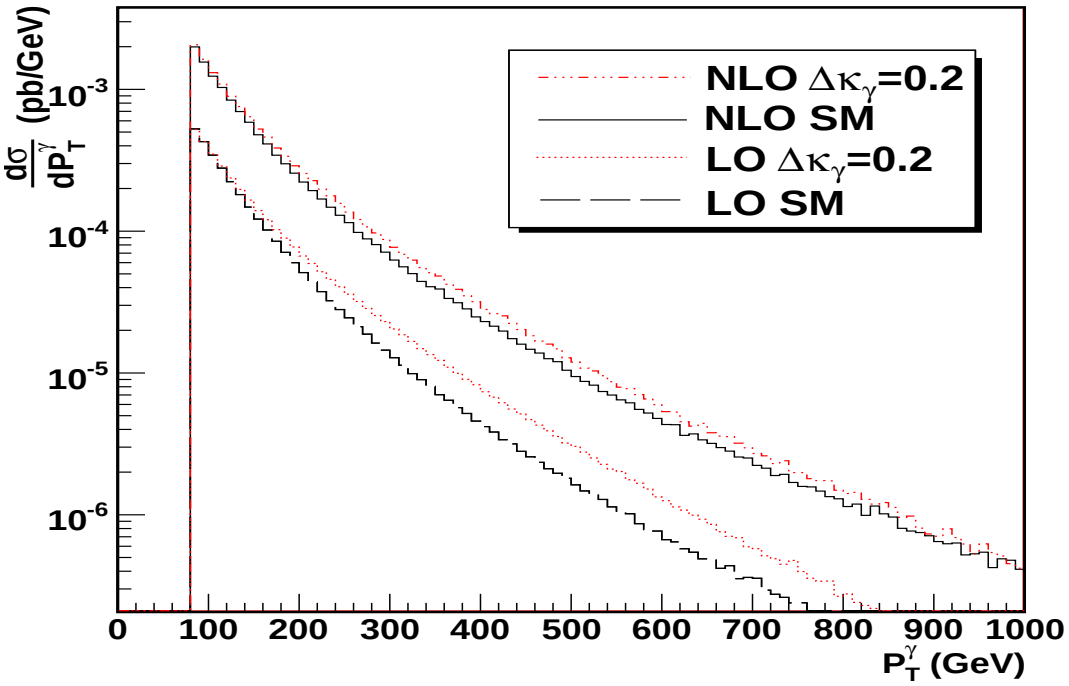

Figure 2.3: LO and NLO photon P_T distributions for the SM and with $\Delta\kappa_\gamma = 0.2$. The lower pair of lines illustrate the large sensitivity at leading order between the SM case and with $\Delta\kappa_\gamma = 0.2$. When the NLO effects are included the fractional sensitivity between the SM and $\Delta\kappa_\gamma = 0.2$ is greatly reduced as shown in the top two lines. This plot and subsequent generator level plots in this chapter, unless explicitly stated, were produced using the BHO NLO generator (17) with the following cuts $P_T^\gamma > 80$ GeV, lepton transverse momentum $P_T^l > 20$ GeV, the lepton pseudorapidity $|\eta_l| < 2.5$, the photon pseudorapidity $|\eta_\gamma| < 2.5$ and other cuts as the BHO program default. The pseudorapidity is defined as $\eta = -ln\left[tan\frac{\theta}{2}\right]$ and the polar angle θ is the angle from the beam pipe.

process is proportional to the matrix element squared. To examine this in more detail it can be seen that because the modified matrix elements depend linearly on the anomalous triple gauge couplings then the cross section has a bilinear dependence:

$$\sigma^{pp\to W\gamma+jet}(\Delta\kappa_\gamma, \lambda_\gamma) = \sigma_{00} + \Delta\kappa_\gamma\sigma_{0\kappa} + \lambda_\gamma\sigma_{0\lambda} + \Delta\kappa_\gamma\lambda_\gamma\sigma_{\kappa\lambda} + \Delta\kappa_\gamma^2\sigma_{\kappa\kappa} + \lambda_\gamma^2\sigma_{\lambda\lambda}. \quad (2.7)$$

The differing parton centre of mass energy enhancement factors for $\Delta\kappa_\gamma$ and λ_γ also mean, for a selection of high-P_T events, that the cross section variation for the latter would be greater for a similar shift in the anomalous coupling value, as shown in figure 2.4.

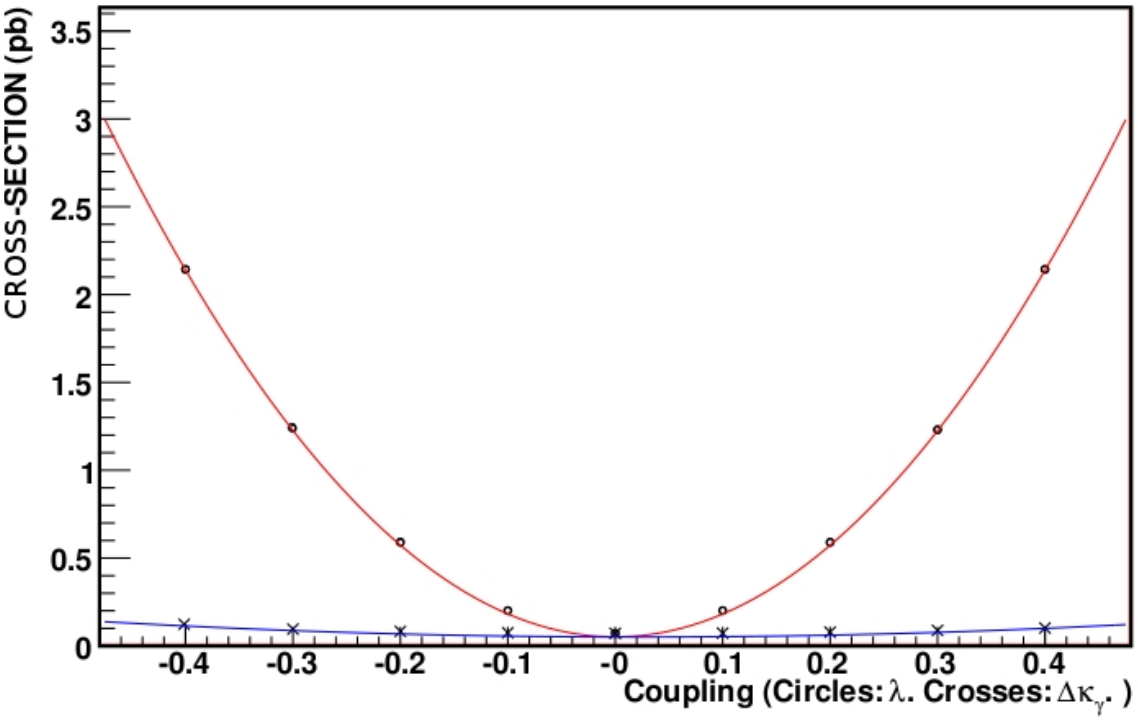

Figure 2.4: The parabolic nature of the cross section for a change in an anomalous triple gauge coupling. The circles (o) represent λ_γ on the x-axis and show a much larger increase in cross section compared to a similar change of $\Delta\kappa_\gamma$ (x). Produced by the SHERPA Monte Carlo generator (19) with the following cuts $P_T^\gamma > 80$ GeV, $P_T^l > 20$ GeV, $|\eta_l| < 2.5$, $|\eta_\gamma| < 2.5$ and other cuts as the SHERPA LHC program default.

From an experimental stance this method is difficult to use as it is highly sensitive to any uncertainty in the normalisation of both signal and background. For a measurement with early data where the systematics will still be under study and statistics will be low this problem is compounded. Using this method it is also not possible to separate the potential effects due to anomalous values of $\Delta\kappa_\gamma$ and λ_γ.

Therefore, this method is not used.

2.4.2 Energy sensitivity

It was described in section 2.2.1 how the anomalous couplings are enhanced when the parton centre of mass energy is high. In the $W\gamma$ s-channel (figure 2.1) this has the effect of increasing the cross section as the parton centre of mass energy increases. This is evident by studying the invariant mass of the $W\gamma$ system $M_{W\gamma}$ as shown in figure 2.5. It can also be deduced that the transverse momentum (and other energy dependent) distributions of the W and γ, as a result of the triple gauge coupling vertex, will display a similar increase in cross section in the tails of the distribution (figure 2.5). When a distribution such as the photon P_T is used the sensitivity to the λ_γ coupling should be enhanced as this combines the energy information of the triple gauge coupling and the angular effects in equation 2.6 that favour the central region of the detector. In chapter 7 the various sensitivities to these distributions are examined.

2.4.3 Production angle and the Radiation Amplitude Zero

The $W\gamma$ channel cross section is predicted by the Standard Model to be suppressed in the central region at a leading order approximation (20; 21; 22). The nature of the suppression is demonstrated when examining the differential cross section $\frac{d\sigma}{d\cos\theta_{\bar{q},\gamma^\star}} \propto (\cos\theta_{\bar{q},\gamma^\star} + \frac{1}{3})^2$ where $\cos\theta_{\bar{q},\gamma^\star}$ is the angle of the photon with respect to the antiquark in the $q\bar{q}$ centre of mass system. The cross section falls to zero at $\cos\theta_{\bar{q},\gamma^\star} = -\frac{1}{3}$. This feature is known as the Radiation Amplitude Zero. One of the effects of production angle enhancements by the anomalous couplings is to destroy the Radiation Amplitude Zero (17). Therefore, by studying the Radiation Amplitude Zero any anomalous couplings present should be highlighted as indicated by Monte Carlo simulation (23).

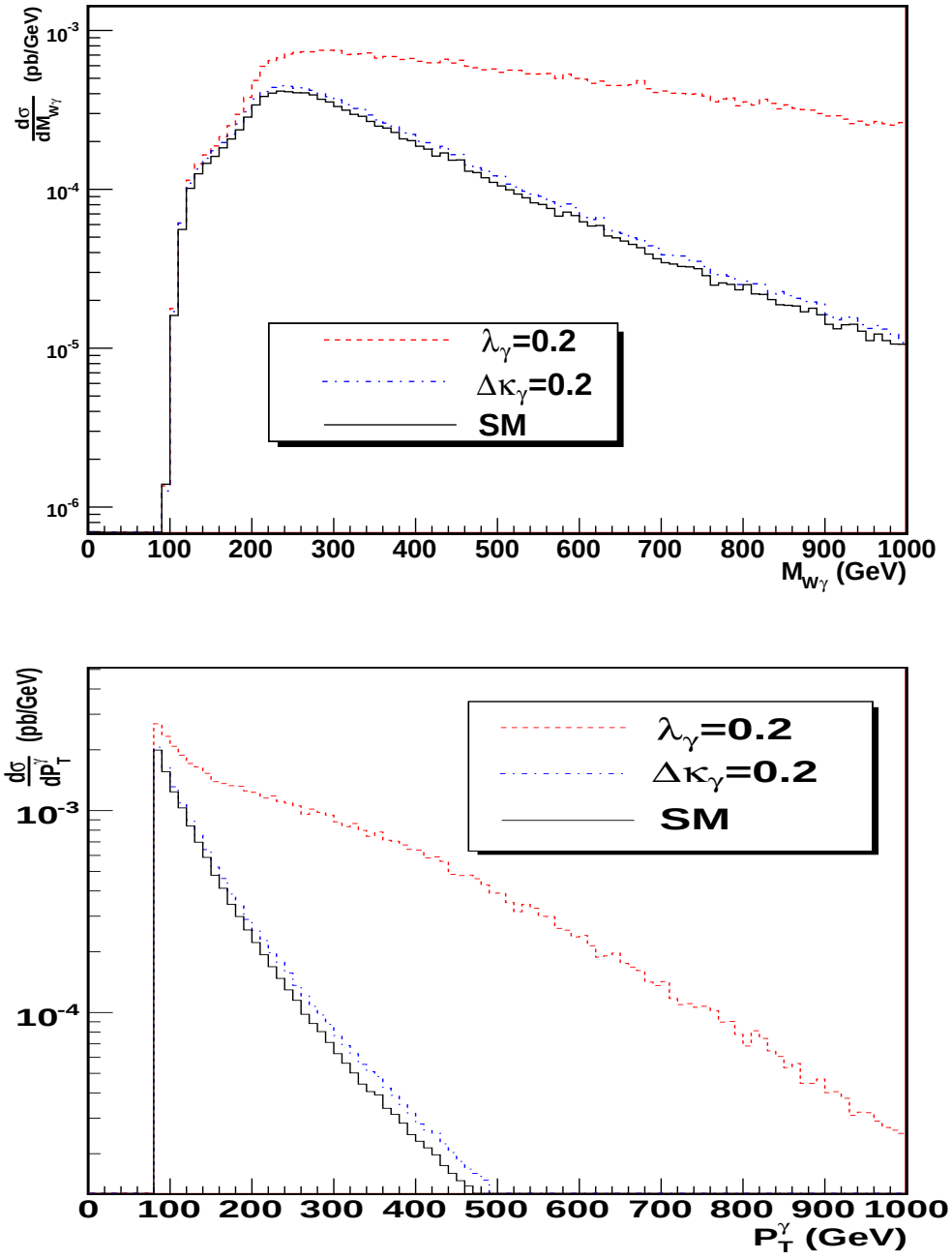

Figure 2.5: Top: a generator level plot of the $M_{W\gamma}$ distribution at NLO for the SM, $\lambda_\gamma = 0.2$ and $\Delta\kappa_\gamma = 0.2$ cases. Bottom: a generator level plot of the P_T^γ distribution at NLO for the SM, $\lambda_\gamma = 0.2$ and $\Delta\kappa_\gamma = 0.2$ cases.

As the radiation amplitude zero has not yet been observed at the Tevatron, due to complications with NLO effects washing it out, this technique of probing triple gauge couplings is viewed as a complementary approach that is best combined with predictions made from the energy behaviour of triple gauge couplings. It is also important to realise that the variable $\cos\theta_{\bar{q},\gamma^\star}$ is not directly observable as it is impossible to tell which beam the antiquark was in. To observe the radiation amplitude zero the production angle of the photon with respect to the beam $|\cos\theta_\gamma|$, in the centre of mass frame has to be used instead. The effect this has is that the two cancellations at $\cos\theta_\gamma = \pm\frac{1}{3}$ are superimposed to give a dip at $\cos\theta_\gamma = 0$. However, studying this distribution is problematic as assumptions have to be made in order to find the longitudinal momentum of the neutrino (see section 7.3). Another alternative has been found (23) that is solely based on the pseudorapidity ($\eta = -ln\left[tan\frac{\theta}{2}\right]$ where the polar angle θ is the angle from the beam pipe) of the photon minus the pseudorapidity of the lepton ($\eta_\gamma - \eta_l$). Experimentally this is quite practical to observe and is sensitive to the filling in of the central region of the detector as shown in figure 2.6.

2.5 Unitarity violation

The anomalous couplings only occur in the s-channel diagram that corresponds to the J=1 partial wave amplitude. As a consequence of unitarity (or more simplistically probability conservation) the cross section for the J=1 partial wave is bounded and will decrease as the partonic centre of mass energy rises. However, when anomalous couplings are included it has been shown that the cross section increases with parton centre of mass energy. Thus at large parton centre of mass energies the model with anomalous couplings becomes unitarity violating. The effective description of the theory therefore breaks down. This does not preclude the fact that anomalous couplings can exist but requires that unknown physics or cancellations between the couplings must be present to maintain unitarity.

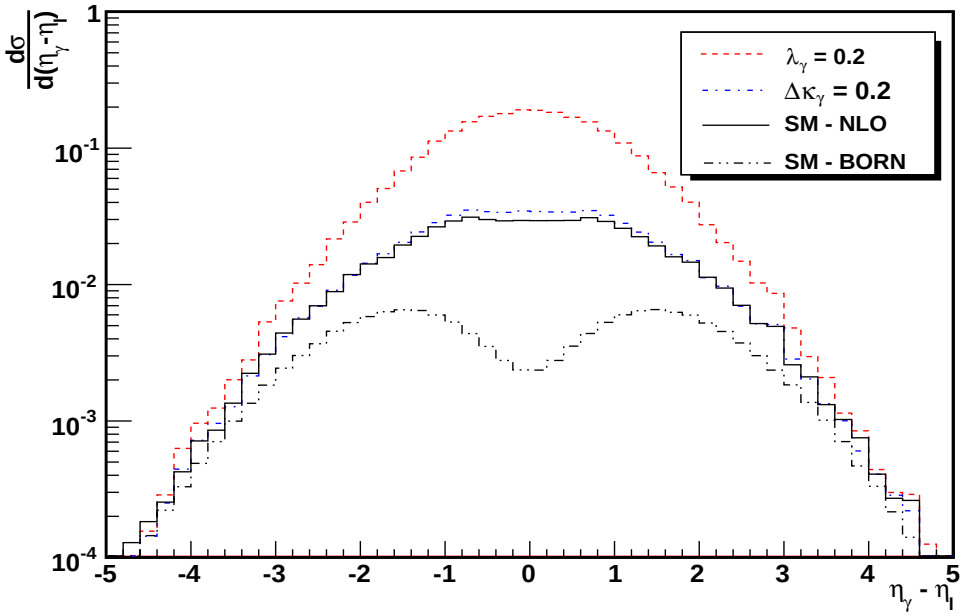

Figure 2.6: The effect of the radiation amplitude zero is observed in this figure via the pseudorapidity difference $\eta_\gamma - \eta_l$. The SM (solid line) and anomalous $\lambda_\gamma = 0.2$ and $\Delta\kappa_\gamma = 0.2$ cases have been plotted at NLO. For reference the leading order SM case has also been plotted to show how the higher order effects make the dip at $\eta_\gamma - \eta_l = 0$ much less evident.

The scale at which unitarity is violated, Λ, has been shown (1) to be:

$$\Lambda^2 = 1.86\,\mathrm{TeV}^2/|\Delta\kappa_\gamma| \tag{2.8}$$

$$\Lambda^2 = 0.99\,\mathrm{TeV}^2/|\lambda_\gamma|. \tag{2.9}$$

One way to ensure that unitarity is not violated is to introduce a form factor that effectively scales an anomalous coupling down as the parton centre of mass energy increases. A conventional form factor that rescales an anomalous coupling $\tilde{A}_0$ to a unitary safe value $\tilde{A}$ is shown below:

$$\tilde{A} = \frac{\tilde{A}_0}{\left(1 + \frac{M^2_{W\gamma}}{\Lambda^2_{FF}}\right)^2}. \tag{2.10}$$

What can be seen in this equation is that the anomalous coupling $\tilde{A}_0$ is reduced when $M_{W\gamma}$ approaches, or is larger than, a preset scale Λ_{FF}, as shown in figure 2.7. By using the rescaled anomalous coupling $\tilde{A}$ in the Lagrangian of equation 2.2 with an appropriate Λ_{FF} the anomalous model can be made unitarity conserving. For the case of $\Lambda_{FF} = 10$ TeV this corresponds to unitarity limits of $|\lambda_\gamma| \leq 0.038$ and $\Delta\kappa_\gamma \leq 0.072$ (24; 25).

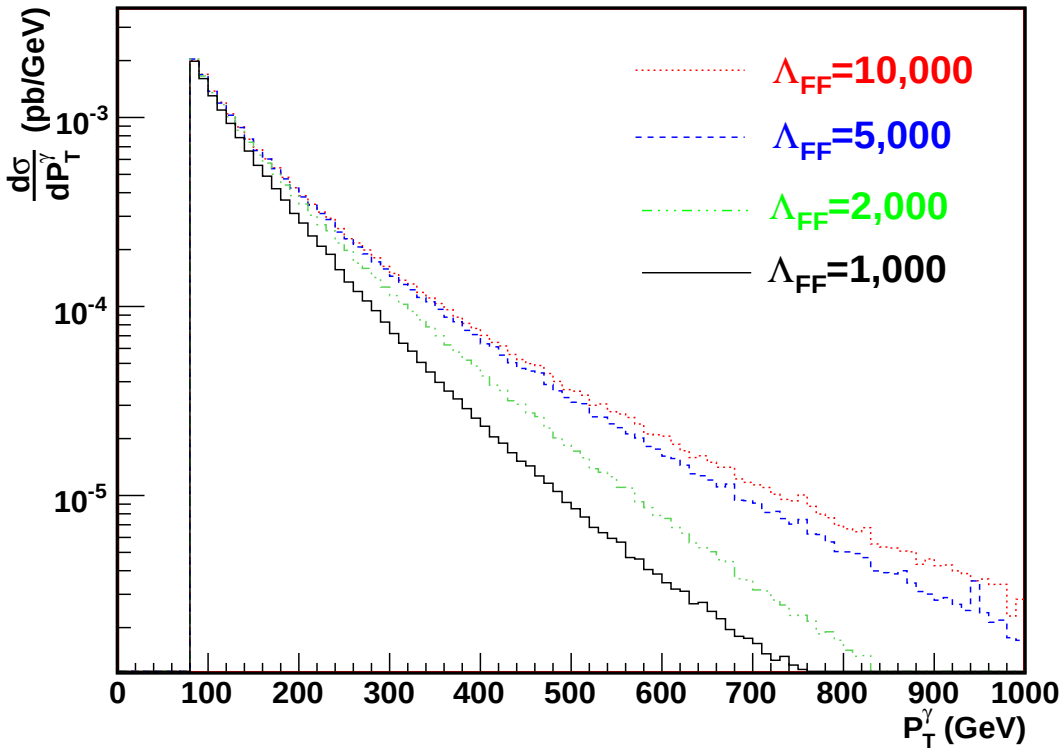

Figure 2.7: The effect of the form factor in equation 2.10 on the photon P_T distribution with $\Delta\kappa_\gamma = 0.5$. The smaller that Λ_{FF} is the more the anomalous effect is suppressed and the distribution approaches the SM limit at approximately $\Lambda_{FF} = 1000$ GeV.

The form factors so far suggested may provide a suitable method of avoiding unitarity violation but there is no compelling physical reason to choose any particular form factor. A consequence of this is that using the different form factors leads to different measured anomalous coupling values or limits. Due to this, the approach

suggested by (26) is adopted where a form factor of 1 is used up to a cut off value on the diboson invariant mass $M_{W\gamma}$. Therefore, any event with a measured $M_{W\gamma}$ greater than a specified value is vetoed from the analysis. This removes the arbitrary nature of the form factor and may be applied directly to the data. A suitable unitarity safe value at which to set the upper cut on $M_{W\gamma}$ was found in (2) to be 3 TeV for pp collisions at $\sqrt{s} = 14$ TeV and is used here.

2.6 Review of current measurements and predictions of anomalous triple gauge couplings

Triple gauge couplings have been probed directly by several experiments most notably at LEP and the Tevatron. In this section the measurements made by LEP are briefly reviewed before examining the latest results from the Tevatron. After this the predictions made from an ATLAS fast simulation study in the $W\gamma$ channel are assessed (2).

The LEP collider allowed the study of triple gauge couplings through the $e^+e^- \rightarrow W^+W^-$, $We\nu$ and $\gamma\nu\bar{\nu}$ channels up to a centre of mass energy of 209 GeV. The results of the ALEPH, DELPHI, L3 and OPAL experiments have been combined (27). It was found that the results were consistent with the Standard Model within the 95 percent confidence intervals shown below:

$$-0.105 < \Delta\kappa_\gamma < 0.069 \tag{2.11}$$

$$-0.059 < \lambda_\gamma < 0.026. \tag{2.12}$$

More recent measurements (28; 29; 30; 31) have been made by the Tevatron experiments CDF and D0 at a proton-antiproton centre of mass energy of $\sqrt{s} = 1.96$ GeV. One of the latest measurements made in the $W\gamma$ channel by D0 (30) constrains the anomalous couplings at the 95 percent confidence level and with a $\Lambda_{FF} = 2$ TeV

to be:

$$-0.88 < \Delta\kappa_\gamma < 0.96 \tag{2.13}$$

$$-0.20 < \lambda_\gamma < 0.20. \tag{2.14}$$

The predictions made from the ATLAS fast simulation study (2) indicate the potential that the LHC, with its higher parton centre of mass energy, has over previous experiments. The limits shown below correspond to a luminosity of 30 fb^{-1} and indicate what could be achieved after three years of running within a 95 percent confidence limit and assuming that no anomalous couplings are found:

$$-0.098 < \Delta\kappa_\gamma < 0.083 \tag{2.15}$$

$$-0.0045 < \lambda_\gamma < 0.0045. \tag{2.16}$$

Chapter 3

The ATLAS Detector at the Large Hadron Collider

As one of the four detectors at the Large Hadron Collider, ATLAS will be fundamental to the discovery of new physics. One important discovery would be proving the existence of the Higgs boson. The ATLAS experiment will be able prove its existence because the Standard Model constrains its mass to lie within the experimentally observable limits. The aim of this chapter is to examine the various features of ATLAS (32) that will exploit this new realm and in particular the $W\gamma$ channel. Furthermore, this chapter will serve as a foundation for the work done on the trigger in the following chapter.

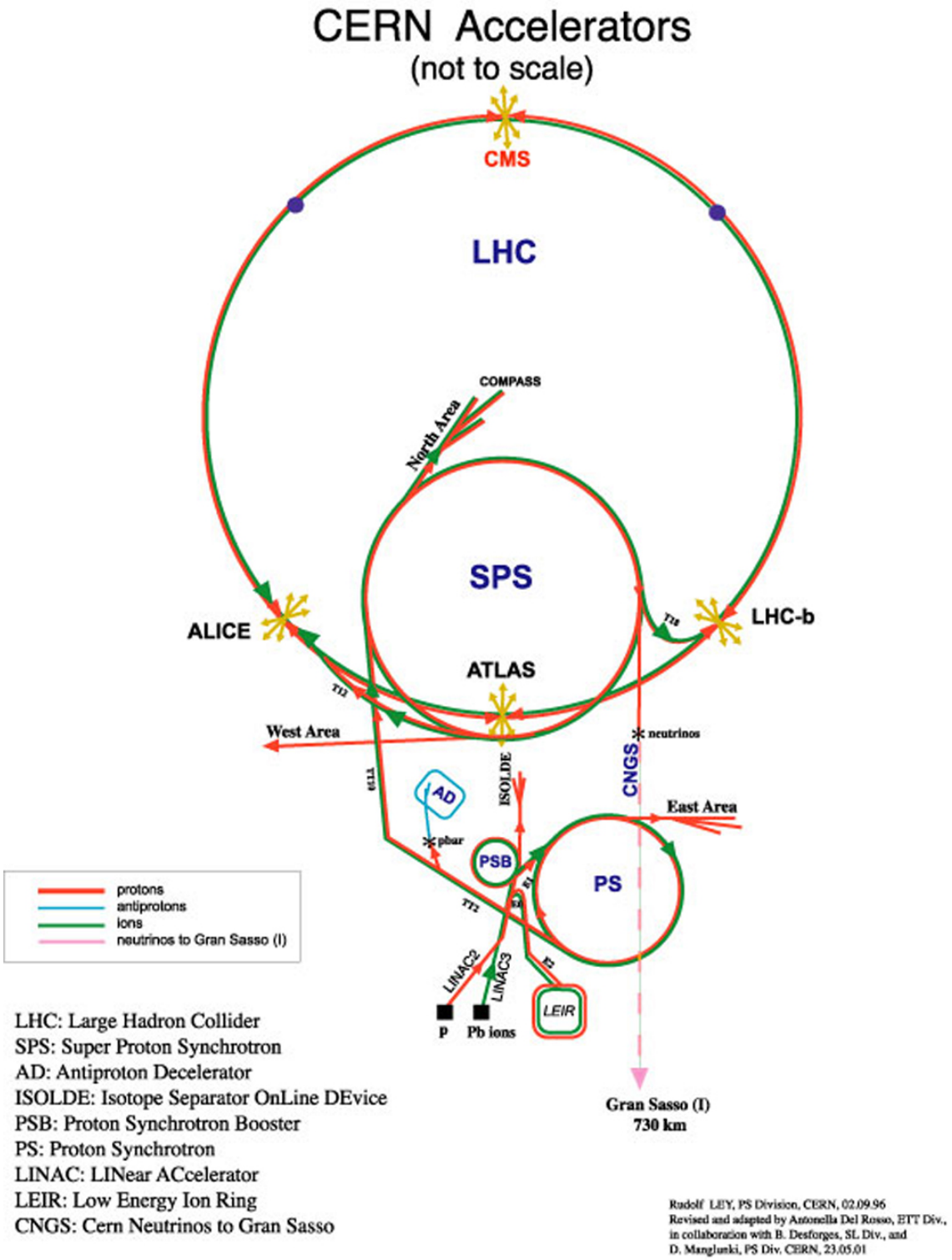

Figure 3.1: The layout of the accelerator complex at CERN (33).

3.1 The Large Hadron Collider

3.1.1 The accelerator complex at CERN - creating 7 TeV protons

The protons that are to be accelerated to 7 TeV originate from a hydrogen gas canister. By taking hydrogen atoms from this canister, creating negative hydrogen ions H^- and then accelerating these negative ions towards a high potential electrode the two attached electrons can be stripped off, so that the resultant positively charged protons can be re-accelerated (34). Several particle accelerator machines are used to raise the energy of these protons gradually up to the final 7 TeV energy. The first accelerator, Linac2 (as can be seen on figure 3.1), initially accelerates the protons to 50 MeV. After this the proton beam enters the Proton Synchrotron Booster (PSB) where the protons are accelerated to 1.4 GeV. They are then transferred to the Proton Synchrotron (PS) which is a proton pre-injector to the Large Hadron Collider (LHC). It is in the Proton Synchrotron that the protons are further accelerated to 26 GeV and the LHC bunch spacing of 25 ns is created due to the use of 40 and 80 MHz RF systems. The beam is then injected into the Super Proton Synchrotron (SPS) where the protons are accelerated to 450 GeV. The proton beams at this point are split off into the Large Hadron Collider in both clockwise and anticlockwise directions. Once the protons are in the Large Hadron Collider it should then only take 20 minutes to accelerate the protons in both rings to 7 TeV. These beams are collided at several places around the ring, one of which is at the centre of the ATLAS detector.

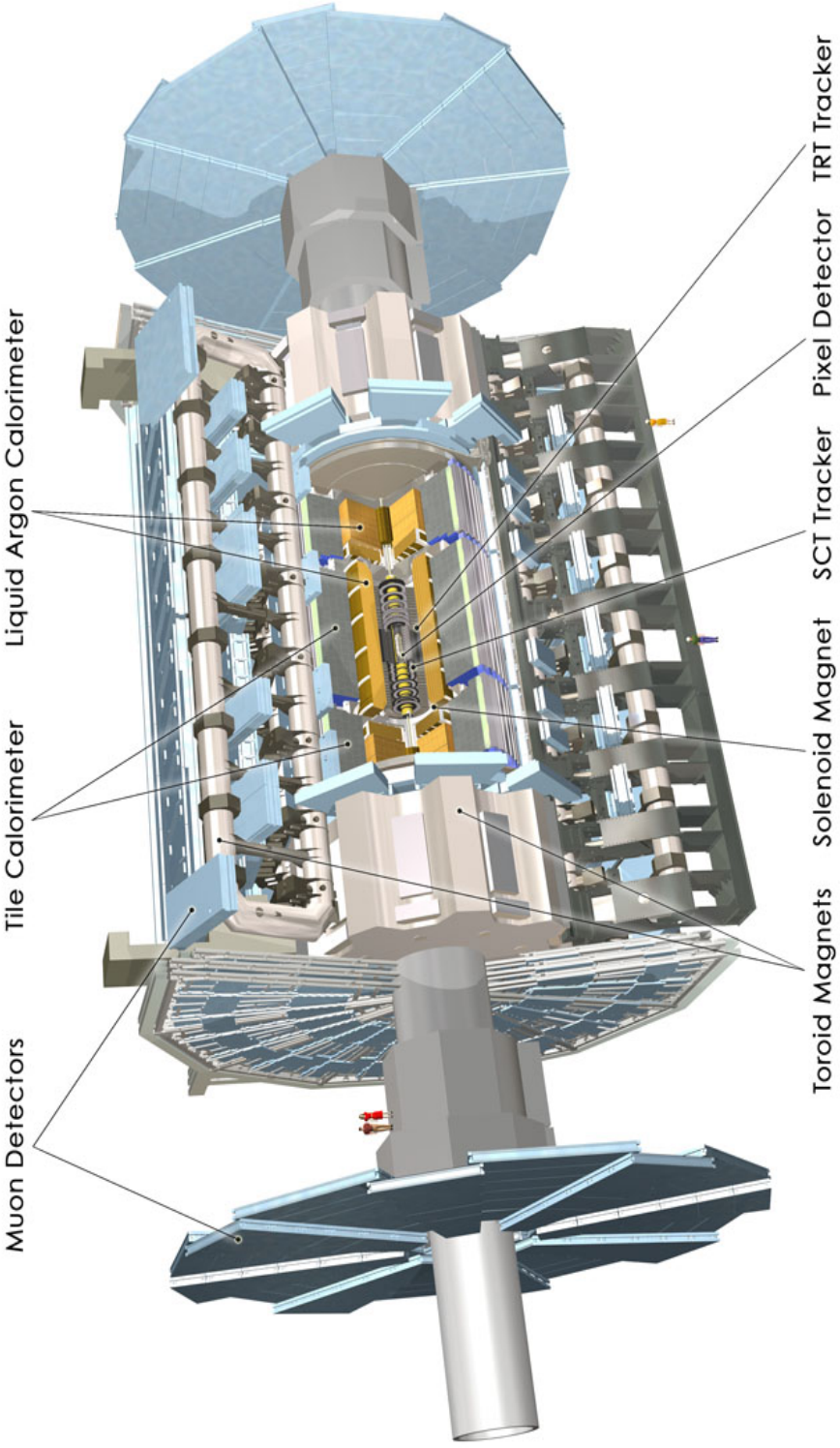

Figure 3.2: The ATLAS detector (33).

3.2 Introduction to the ATLAS detector

The ATLAS detector (figure 3.2) is over 46 m long, 25 m wide and 25 m tall. It has been designed to measure a wide variety of physics within the harsh radiation environment of the LHC. Like most particle detectors ATLAS follows the usual formula for detector design in that it is made up of several layers that are each configured to measure different properties of the particles that pass through. By using this type of design a picture of an event can be established if the information from all the individual layers is assembled. For the type of physics that the ATLAS project is interested in (35) there are high demands placed on the detector to locate vertices and track particles. In particular, the tracking detector is required to measure high transverse momentum charged leptons and heavy flavour particles. One of the other goals of ATLAS is to build a detector with a good electromagnetic calorimeter and full hadronic calorimetry coverage. The electromagnetic calorimeter will primarily be used for the identification and measurement of the energy of electrons and photons while the outer hadron calorimeter will improve measurements of isolated hadrons, jets and missing transverse energy. As final state muons will also play a crucial role in identifying new physics a good muon spectrometer will be required. This spectrometer is placed outside the calorimeter because high momentum muons will pass through to it with a minimum of interaction. Other overall objectives for ATLAS are to provide full coverage of the interaction point in the azimuthal angle and as much as possible in pseudorapidity. Each part of the detector will now be described from the interaction point outwards.

3.3 The Inner Detector

The first active part of the detector is the inner detector (figure 3.3). Its primary role is to reconstruct the tracks of charged particles over a region of $|\eta| < 2.5$

and by so doing to reconstruct interaction and decay vertices. By measuring the curvature of the tracks in the magnetic field (B-field) of the solenoid a precise transverse momentum measurement can be obtained. In addition to the momentum measurement the sign of charged particles can be deduced from the direction of the deflection in the B-field.

Due to the inner detector's proximity to the interaction point it needs to be radiation hard, have good momentum resolution and fast electronic readout. Equally importantly the detector needs to contain as little material as possible in order to reduce errors on the momentum resolution due to scattering and the absorption of particle energy due to showering. In the construction of the inner detector three different technologies are used that are capable of balancing the high radiation, interaction rate and particle density with the required performance.

3.3.1 Pixel Detector

Closest to the beam pipe and hence subject to the highest radiation is the silicon pixel detector. This is one of the newer technologies to be used in particle detectors and is capable of withstanding an absorbed radiation dose of 300 kGy (where one gray is the absorption of one joule of energy by one kilogram of matter (36)). This represents a very high amount of absorbed radiation and can be placed in context by noting that a typical medical X-ray is 1.4 mGy or perhaps more importantly the lethal limit to a human is approximately 10-20 grays delivered to the whole body at the same time (37; 38). It also has a very high granularity to meet the necessary physics requirements of measuring decay lengths. In total there are over 80 million pixels that measure 50×400 μm^2 arranged on pixel detector sensors. These pixel detector sensors are spread over three barrels (at radii of 5 cm, 9 cm and 12 cm) and three disks at either end (at radii of 9 to 15 cm). The location of these barrels and disks ensures that at least three precision measurements should be made for the full ATLAS acceptance region so that a resolution of $\sigma_{R\phi} = 12$ μm and $\sigma_z = 66$ μm

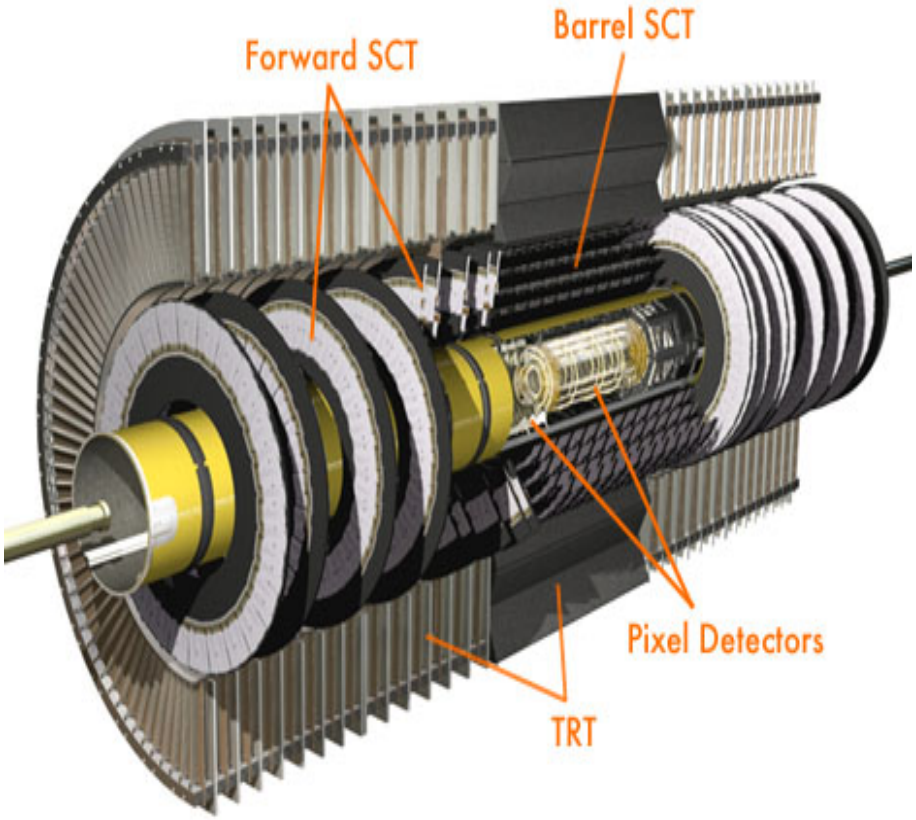

Figure 3.3: The Inner Detector (33). See the text for a further description of the labelled parts.

(on the disks $R = 77$ μm) is achieved.

3.3.2 Semiconductor Tracker (SCT)

Radially outwards from the silicon pixel detector lies the Semiconductor Tracker detector. The SCT should give 8 measurements per track over the range of $|\eta| < 2.5$. This will be most useful for the main determination of track parameters and the momentum measurement.

The detector consists of 4088 silicon detector modules, where each module has been created by wrapping around a silicon layer to create two sides on the module. Readout strips are placed every 80 μm on the silicon and in total there are approx-

imately 6 million. The layout of these two sided silicon modules is over four barrel layers (at radii of 30 cm, 37 cm, 45 cm and 52 cm) and 9 end-cap disks at each end. A space point resolution of $\sigma_{R\phi} = 16$ μm and $\sigma_z = 580$ μm can be obtained. This is a lower resolution than the pixel detector but a cost effective alternative that allows tracking to continue radially outwards towards the calorimeter.

3.3.3 Transition Radiation Tracker (TRT)

The outermost part of the inner detector is the Transition Radiation Tracker. This has been designed to allow continuing tracking of particles out to the calorimeter but with a lower cost than either of the other technologies (due to the increase in volume it covers).

The active part of this detector is a gas filled wire drift detector consisting of a 4 mm diameter straw with a 30 μm diameter gold-plated tungsten wire running down the middle of the straw. In total there will be 100,000 straws in the barrel region covering radii of 56 cm to 107 cm and 400,000 straws in the end-caps . A drift time measurement can be made that gives a spatial resolution of 170 μm. In addition to this a Xenon gas mixture is used so that transition radiation photons can be observed. This is useful in distinguishing heavy charged particles from lighter ones that have similar energies because the probability of transition radiation emission is greater for a larger relativistic γ factor. Electron identification is particularly enhanced by this feature because of the low electron rest mass.

3.4 Calorimeters

The ATLAS detector incorporates calorimeters designed to measure the energy of both hadronic and electromagnetic particles. The general layout of the calorimeters can be seen in figure 3.4. The technologies used and their position reflect the different

requirements of measuring the energy of an electromagnetic particle compared to a hadronically interacting one. However, the basic principle that both calorimeters operate upon is that an incident particle interacting with matter produces a shower of particles. As the charged particles in the shower pass through an appropriate active medium a measurable quantity such as charge or light is produced that allows the energy of the shower to be determined.

In the following subsections the details of both the electromagnetic calorimeters and hadronic calorimeters are explained. In this study the electromagnetic calorimeter is important as it has an impact on the ability to distinguish electrons/photons from jets. This is a crucial factor in observing the $W\gamma$ channel over W+jet type backgrounds.

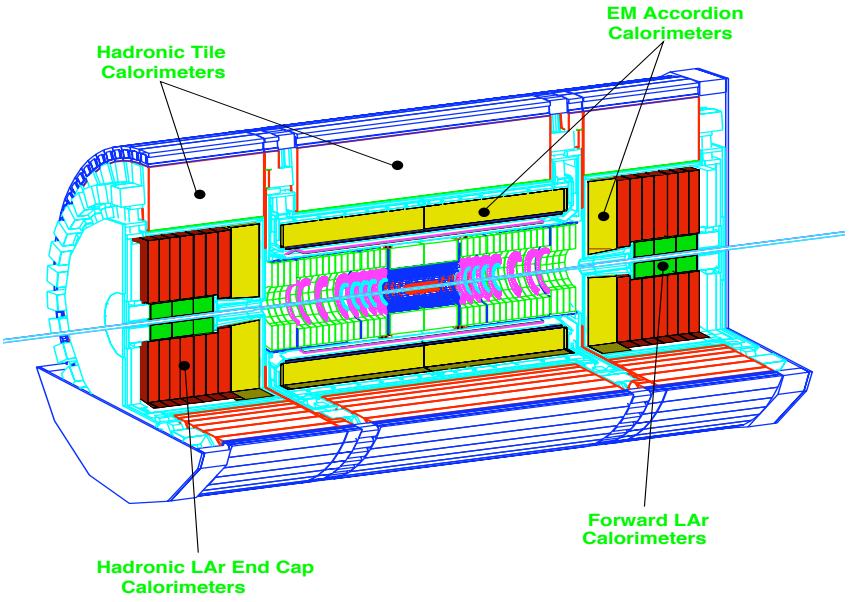

Figure 3.4: The layout of the different calorimeters in the ATLAS detector (33).

3.4.1 Electromagnetic calorimeters

The electromagnetic calorimeter's primary role is to measure the energy of electrons and photons while providing discrimination from other particle types. It is a lead liquid argon (LAr) sampling type detector with an accordion type structure as shown in figure 3.5. The lead plates have a short radiation length that causes incident electrons or photons to interact with them through the dominant processes of photon conversion and electron bremsstrahlung. These processes create other electrons or photons that can, if energetic enough, cascade to cause a shower. When this shower passes into the liquid argon the electrons in the shower lose energy by ionisation and the resulting charged particles released are recorded by electrodes. The total energy of the incident particle can then be found by examining the deposits in the relevant liquid argon sampling layers (figure 3.6). It should also be noted that by examining a shower's path the flight direction of neutral particles such as photons can be established. The shower shape and location in the calorimeter also play a role in helping to distinguish electrons and photons from hadronic particles because electromagnetic showers are pencil shaped and not as penetrating as hadronic ones.

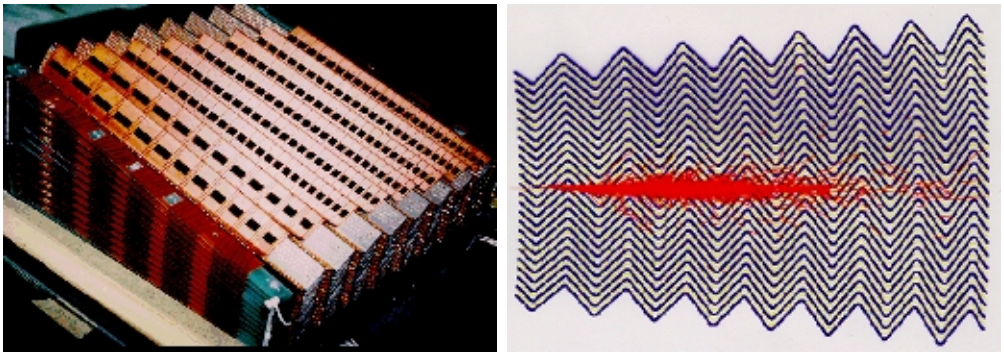

Figure 3.5: Left: Part of the electromagnetic end-cap calorimeter that has been exposed to show its accordion structure. Right: An illustrative picture showing the shower caused by a particle passing through the calorimeter (33).

The electromagnetic calorimeter is divided into a barrel and two end-cap sections that collectively give full coverage in ϕ and up to $|\eta| < 3.2$. However, where the

end-cap and barrel meet at $|\eta| \approx 1.4$ there is a small gap in the η coverage that leads to reduced performance. For making precise physics measurements such as identifying the photon or lepton in the $W\gamma$ signal the calorimeter is limited to the region of $|\eta| < 2.5$ as this is where there is an overlap with the inner detector, as illustrated in figure 3.7.

The electromagnetic calorimeter is made of several layers. The initial layer is a presampler, it has no lead in front of it and is just a layer of liquid argon. This is positioned here so that a correction for the energy lost in the inner detector, solenoid coils and cryostat wall can be made. The next layer, the first sampling layer, is designed to give good resolution in the η co-ordinate and helps with photon-π^0 separation. This is achieved by the structure of the cells being fine strip detectors as illustrated in figure 3.6. The second sampling layer is the deepest sampling. It is thus where most of the energy of an electromagnetic shower is deposited and is used to determine the position of the particle showers. The third and final sampling layer records only the tail of high energy electromagnetic showers. In the end-cap calorimeter, the presampler is not required because there is less material between it and the interaction point and therefore no need for any correction.

3.4.2 Hadronic calorimeters

In the study of the $W\gamma$ channel the hadronic calorimeter is useful as it covers a large pseudorapidity ($|\eta| < 4.9$). It is because of this that a measurement of the missing transverse energy E_T^{Miss} can be made. In the case of the $W\gamma$ channel the neutrino from the W boson will carry away a large amount of missing energy. The hadronic calorimeter will therefore help in measuring the amount of missing transverse energy in an event and thus in reconstructing the neutrino from the W.

In addition to this the calorimeter has been designed so that it can absorb the majority of the jets in order to limit the background into the muon system. However,

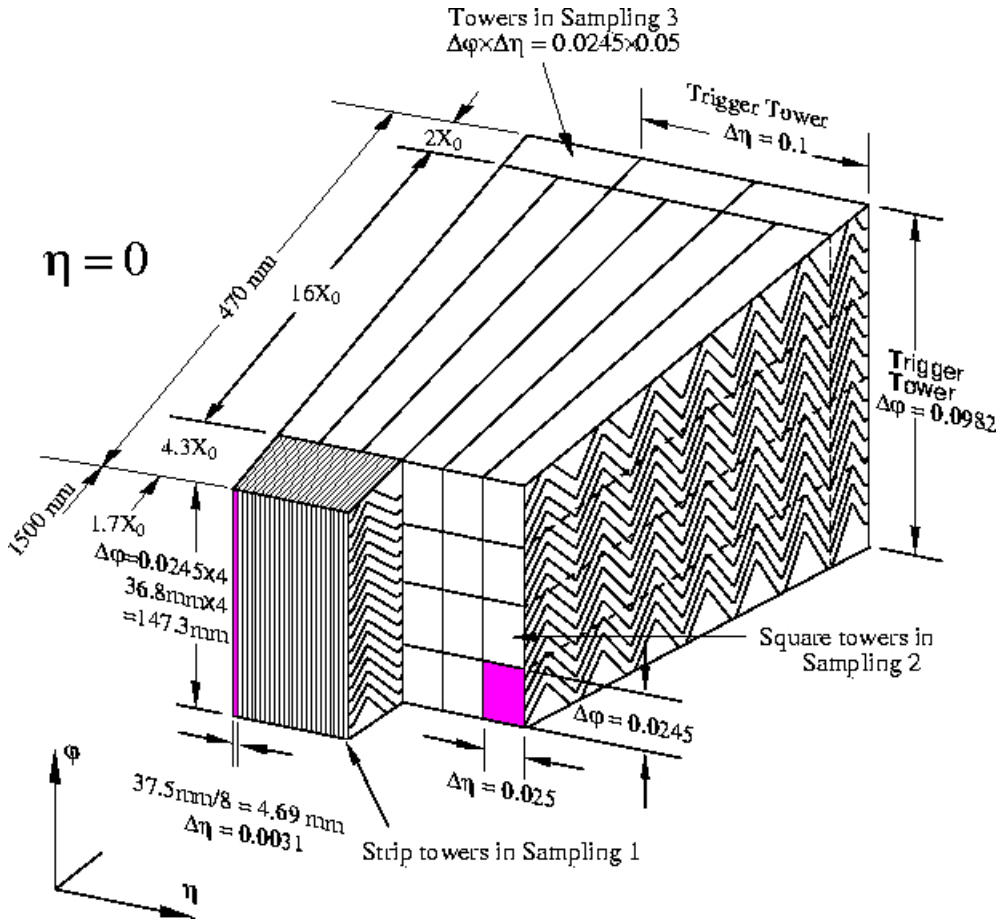

Figure 3.6: The sampling layers of the electromagnetic calorimeter with their respective cell sizes (33).

hadronic showers are caused by the strong interaction with calorimeter nuclei, and one of the implications of this is that at least 10 interaction lengths of material are required to absorb all of the shower. A typical hadronic shower is normally initiated in the electromagnetic calorimeter but with the majority of the shower absorbed in the hadronic calorimeter. Further complications in the design of the calorimeters are due to the changing radiation intensity in different parts of the detector. Therefore, in the barrel region a tile calorimeter is used, while the end-cap and forward calorimeters are of a more radiation-hard liquid argon design.

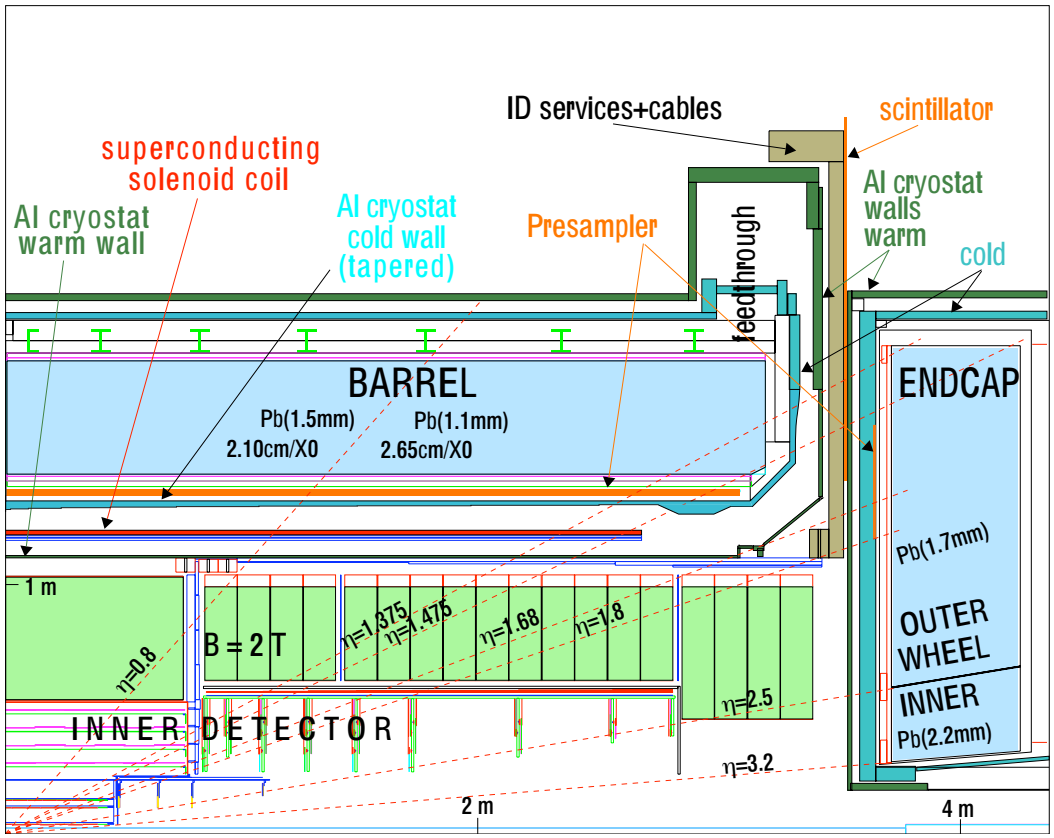

Figure 3.7: A quadrant of the inner detector with the electromagnetic calorimeter. It is in this region that all precision measurements regarding electrons and photons are made (33).

3.5 Magnets

Only tracking parts of a detector require a magnetic field to curve the tracks of the particles produced to measure their momenta. In order to do this, sufficiently large magnetic fields of a few tesla are needed. In the case of ATLAS two magnet systems are used. The first system consists of a thin solenoid magnet (figure 3.8) which is placed around the inner detector. This magnet produces a 2 T field and because of its location before the calorimeters has to be thin in order that particles passing through it interact as little as possible. The second system used is a collection of coils which together form a large 4 T air-core toroid system (figure 3.8). This magnet

is placed outside the calorimeter and is used for making a more precise measurement of muon momenta relative to the one made in the inner detector.

3.6 Muon chamber

The muon spectrometer is placed outside the calorimeter and is the outermost sub-detector (figure 3.9). This spectrometer is designed to record high momentum muons and is thus optimised for resolution, rapidity coverage and track reconstruction.

Momentum measurements within the spectrometer are made possible by using the large air-core toroid magnets to deflect the muons. This allows the muon transverse momentum, as similarly measured in the inner detector via the curvature of tracks, to be accurately established. The B-field that is produced from the magnets is designed to be orthogonal to the muon flight direction. Particular care has also been taken so that in the transition region, $1 < \eta < 1.4$, between the end of the barrel toroid and the end-caps the B-field will also be roughly orthogonal to the direction of the muons.

To aid in precisely measuring the particle tracks and hence calculating the transverse momentum the spectrometer has been constructed in the form of three barrels and four disks. These have been placed at radii of 5, 7.5 and 10 metres from the interaction point for the barrel layers and at 7, 10, 14 and 22 metres for the disks. The technology used in each of the layers varies due to the demands placed upon it by the high background and event rate. However, for most of the coverage Monitored Drift Tubes (MDT) are present on the layers and disks. It is these drift tubes, with a single wire resolution of 80 μm, that are used to make the precision measurements. In the more specialised area near the interaction point and at large pseudorapidity ($2 < \eta < 2.7$) Cathode Strip Chambers (CSCs) are utilised. These are effectively multi-wire proportional chambers that have a low sensitivity to the background and a high resolution due to the cathode being segmented. Two other technologies are

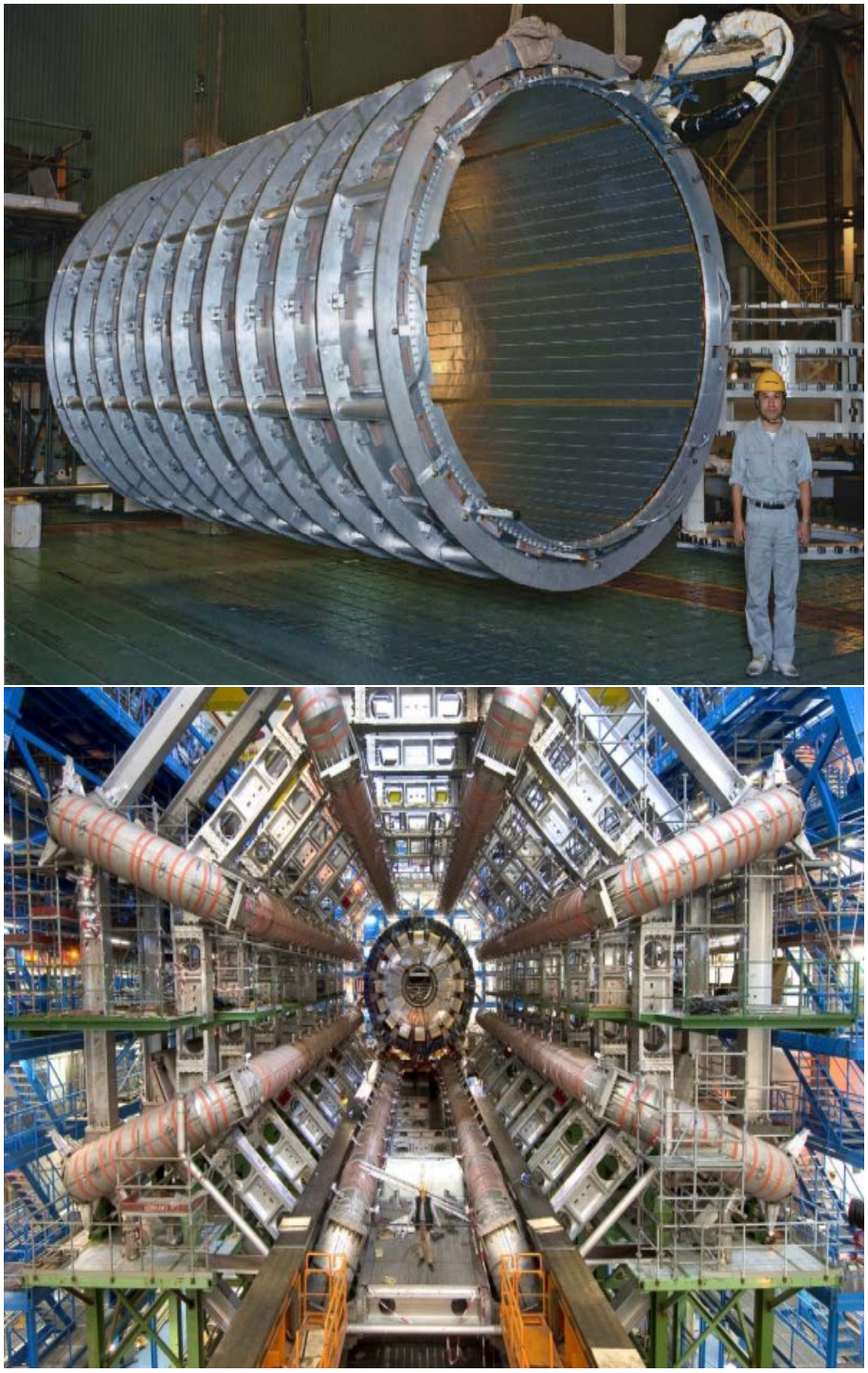

Figure 3.8: The magnets used in the ATLAS detector. Above: The solenoid magnet. Below: The 4 T toroidal magnet system (33).

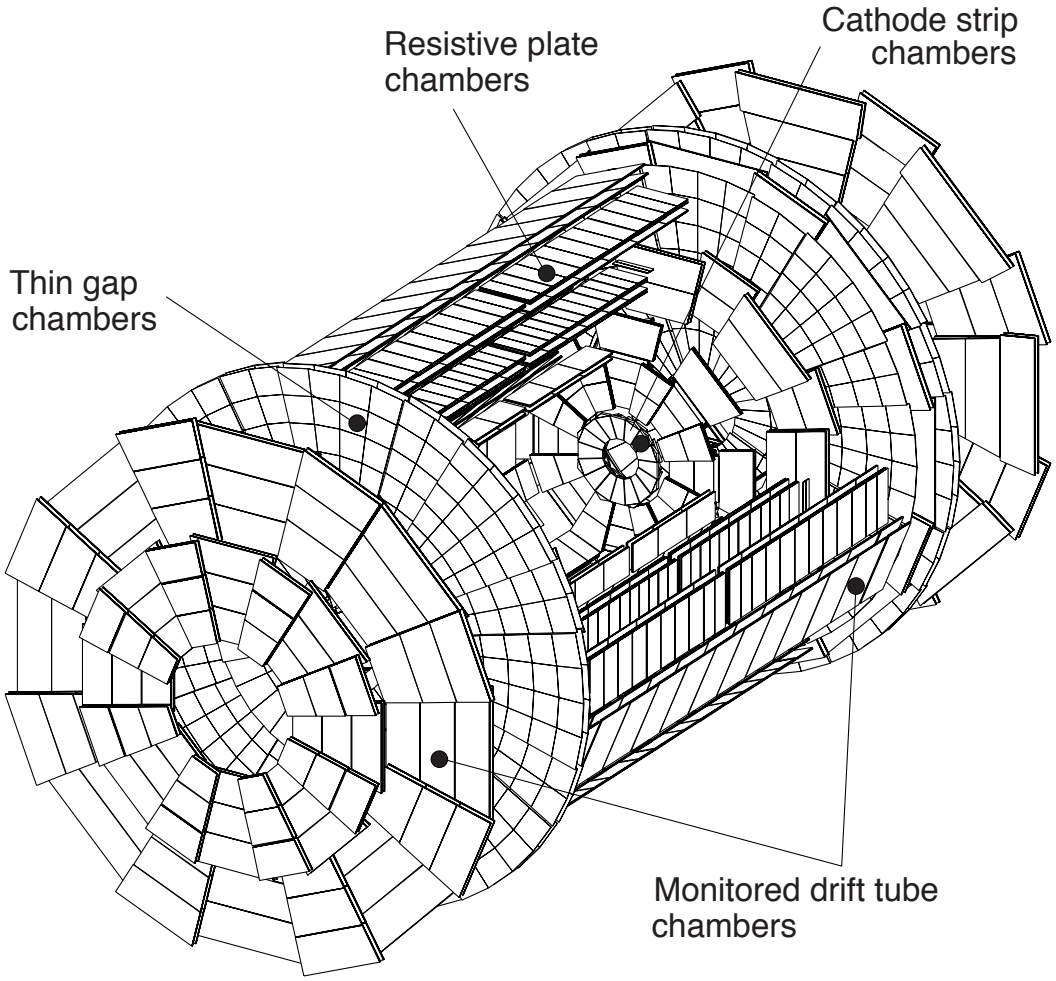

Figure 3.9: The Muon Detector (33).

also used but placed around the other types. These are Resistive Plate Chambers (RPC) found in the barrel and Thin Gap Chambers (TGC) in the disks. Their main purpose is to produce a fast trigger.

3.7 The Trigger

At design luminosity there will be 800 million collisions per second occurring at the interaction point of ATLAS. Although a colossal number, only a small fraction of these events will be from the most interesting physics channels. In order to carry out the filtering of data the ATLAS three level trigger system has been developed (39; 40).

The strategy of the trigger system can be examined by initially considering bunches of protons crossing in the detector at a rate of 40 MHz. For the purpose of data analysis in software this interaction rate is too fast and the event rate must be reduced by the level-1 trigger to a maximum rate of 100 kHz. The level-1 trigger achieves this by using reduced granularity data from the calorimeter and data from the muon chambers. The fast electronics of the level-1 trigger must then make specific cuts on the event to judge its usefulness, within a maximum latency of 2.5 μs, while the full event is temporarily stored in pipeline electronics. The results from this are then passed to the Central Trigger Processor (CTP) which can check to see whether the level-1 trigger results correspond to pre-selected menus. If a match exists between what has been sent from the level-1 trigger and these menus a level-1 Accept is broadcast to the rest of the involved hardware. This indicates that the level-2 trigger should proceed and that the event is read out and stored in Read Out Buffers (ROBs). The level-2 trigger performs a more thorough analysis on the Regions of Interest (ROI) that are sent to it from the level-1 trigger by utilising both the full granularity of the detectors and also all the subdetectors (Calorimeter, Muon and Tracking). The hardware of the level-2 trigger has 10 ms to analyse the data with the objective of reducing the rate to 1 kHz. An Accept decision at this stage means that data is passed to an Event Builder which assembles the event together. The last part of the trigger is known as the Event Filter. It has access to the full event data from the Event Builder. The Event Filter differs from the other trigger levels in that its algorithms have not been specifically designed for speed,

instead they will use algorithms as similar to the offline analysis as possible. This allows the rejection of events that would hopefully not be of use in a full physics analysis.

Chapter 4

Level-1 calorimeter trigger testing and calibration

The level-1 calorimeter trigger (41) is a vital part of the detector and must be operational for the majority of physics studies to occur. Failure of it to work will result in data being irretrievably lost. Substantial time during the PhD has been focused on the testing and implementation of two components of the level-1 calorimeter trigger. The first of these was examining how the Cluster Processor Module (42) operated at relatively extreme temperatures. However, the majority of the trigger based work was in investigating and developing a prototype mechanism that could be used for calibrating level-1 calorimeter modules. The Common Merger Module (43) which had relatively simple criteria to calibrate was chosen for this development. In the following pages the results from the above work will be documented. In addition a detailed introduction to the relevant modules will be given in the first section, to place this work in context.

4.1 An overview of the level-1 calorimeter trigger

The level-1 calorimeter trigger receives over 7200 signals from the electromagnetic and hadronic calorimeters. Each of these 7200 signals is a summed analogue trigger tower that corresponds to a 0.1 by 0.1 (in $\eta \times \phi$ where η is the pseudorapidity and ϕ the azimuthal angle around the beam pipe in units of radians) part of the calorimeters. These signals are digitised and assigned to the appropriate bunch crossing and processed to produce information that can be sent to the Central Trigger Processor for a level-1 accept decision to be made. The level-1 calorimeter trigger performs this task by using three sub-systems; the PreProcessor sub-system which digitises the analogue signals, assigns transverse energy E_T values and matches the signals with the correct bunch crossing; the Cluster Processor sub-system that receives the digitised E_T sums and identifies isolated electron/photon and tau/hadron candidates; the Jet Energy Processor sub-system which receives digitised E_T sums, identifies jets and produces global sums of E_T, jet transverse energy E_T^{jet} and missing transverse energy E_T^{Miss}.

The PreProcessor sub-system (PPr) is the first to receive the 7200 signals from the calorimeters. However, the signals are sent via Receiver stations that calibrate the linear gain of the signals on an E_T scale before they arrive at the front panels of the 124 PreProcessors (44). Upon arrival at one of the PreProcessors the analogue differential signals go via one of the four daughter modules on the PreProcessor that converts them to single ended signals. The signals are digitised using a FADC (Flash Analog to Digital Converter) with a sampling frequency of 40 MHz (the LHC clock). The PreProcessor identifies the signal with the bunch crossing and uses a Look-up table to create calibrated transverse energy values. The digitised energy from the PreProcessor modules is then passed to the Cluster Processor and Jet Energy Processor sub-systems via a 480 Mbit/s link.

For the purpose of logistics the Cluster Processor and Jet Energy Processor

sub-systems divide the calorimeters into four quadrants. This allows the Cluster Processor system to use four crates, containing 56 Cluster Processor Modules (CPM) in total, with each crate representing one quadrant in ϕ. Slightly differently the Jet Energy Processor system only needs to use two crates containing Jet Energy Modules (JEM) (45) due to the fact that the input to the algorithms has reduced granularity compared to the Cluster Processor.

4.1.1 The Cluster Processor Module

In the Cluster Processor sub-system each Cluster Processor Module (CPM) receives 80 of the fast 480 Mbit/s Low Voltage Differential Supply (LVDS) links. The CPM is used to identify possible electrons/photons or tau/hadron candidates. This is done algorithmically with a sliding window algorithm as illustrated in figure 4.1. The algorithm consists of a 4x4 window of trigger towers with a central 2x2 core. Within the central 2x2 window a potential candidate is found if a 1x2 or 2x1 combination of trigger towers in the electromagnetic layer is found to pass one of 16 preset thresholds. A special de-clustering algorithm, using the outer trigger towers, is used to ensure no double counting occurs. As shown in the bottom left of figure 4.1 the 4x4 window slides around a larger 5x7 trigger tower environment moving one trigger tower away in ϕ or/and η. In order to process all these 4x4 windows, 8 Cluster Processor (CP) chips per CPM are used (bottom right of figure 4.1). On each CPM it has been designed that these 8 CP chips process 8 overlapping 4x4 windows so that they cover the entire width of the CPM in η. After the algorithm has worked, the overall result is that each CP chip produces two 16 bit cluster candidates. Each of the cluster candidate bits represents the pass or fail status of one of the 16 preset thresholds. The results from all of the CP chips are then collected together and merged to give the number of hits. The result of the merging is stored in a 3 bit multiplicity counter. This means that no more than 7 hit counts may be recorded for any threshold before saturation occurs. The 3 bit multiplicity counter

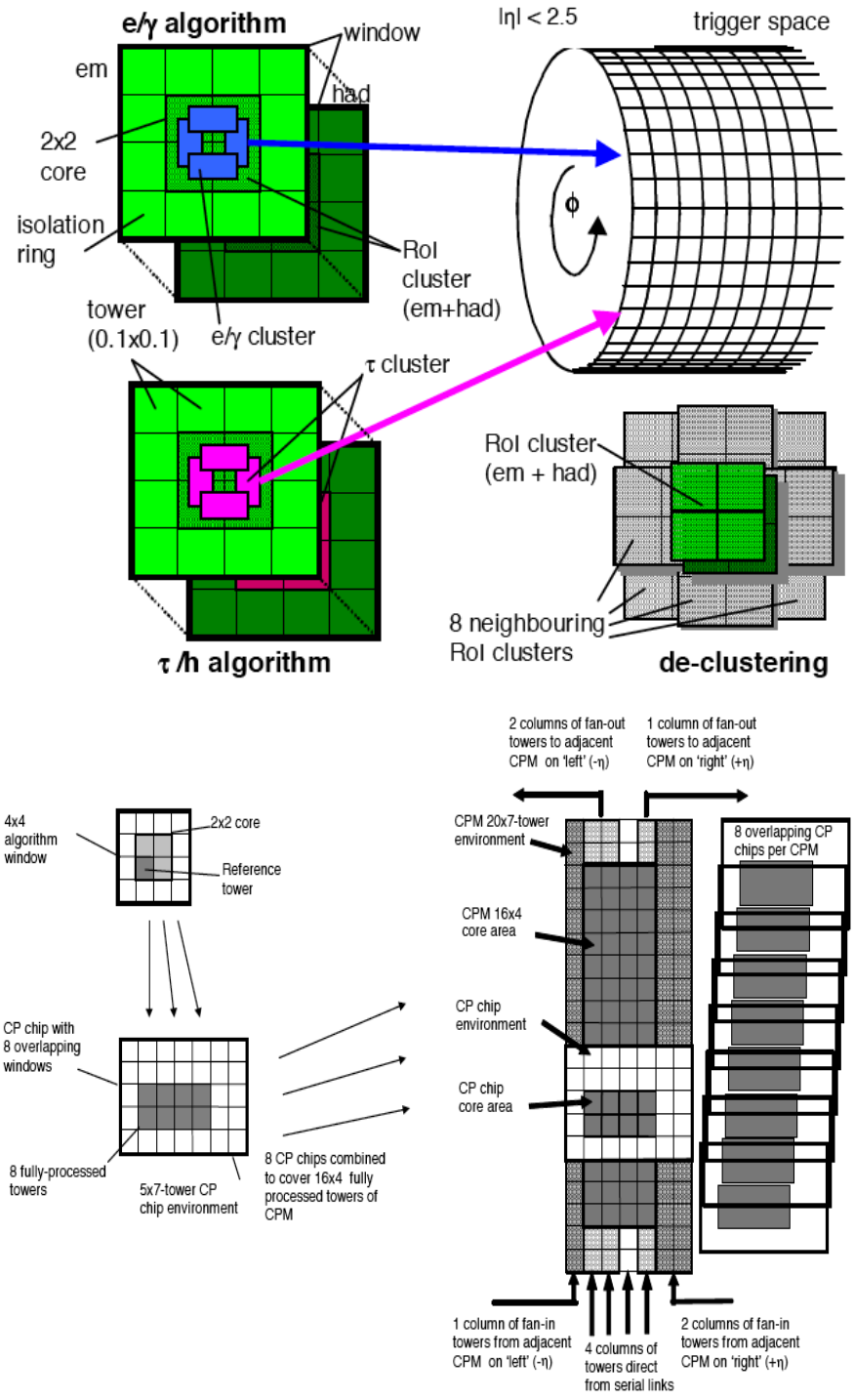

Figure 4.1: Illustration of the sliding window algorithm used in the CPM(42). A full description can be found in the text.

is then concatenated with a parity error bit and sent to the Common Merger Module (CMM). The addition of this parity error bit is vital for checking the integrity of the signal when it arrives at the CMM.

The above process can be examined in a little more detail by considering the real time data flow on the CPM as shown in figure 4.2. The additional information shown here is that the data received, from the PreProcessor Modules, must pass through serialiser chips that take the LVDS signals that are serialised at 40 MHz and then re-times them to 160 MHz. The data then proceed as described above to the CP chips or adjacent CPM modules. On each 40 MHz clock tick each CPM sends the results to the merging logic. Finally, the merging logic on each CPM transmits the results over the backplane at 40 MHz to the Common Merger Modules.

For all of these processes the clock signal is obtained from the Timing, Trigger and Control system and decoded locally on the CPM using a daughter board (the TTCdecoder card) containing the TTCrx ASIC chip (46; 47). The TTCrx chip decodes the timing signals from the Timing, Trigger and Control system so they can be used by the trigger processing modules such as the CPM. One of the most important signals that the TTCrx chip decodes from the TTC is the LHC clock signal. In addition to the process of decoding the LHC clock signal the TTCrx passes it via two independent high resolution phase shifters. The outputs from these two phase shifters result in two clock signals that can be shifted in steps of 104 ps. A 104 ps step is called a TTC tick in the jargon. By having the ability to make small shifts on the clock signals, corrections can be made for the different timing of electronics and track lengths. The two clocks produced from the TTCrx chip are called Clock40Des1 and Clock40Des2. It is important for both Clock40Des1 and Clock40Des2 to be stable as some trigger modules have a domain of validity for their data as narrow as 2.5 ns. Any misbehaviour on either of these clocks over several hundred picoseconds would strongly affect the performance of the system. The stability of the clock from the TTCdecoder card is studied and reported later

in this chapter.

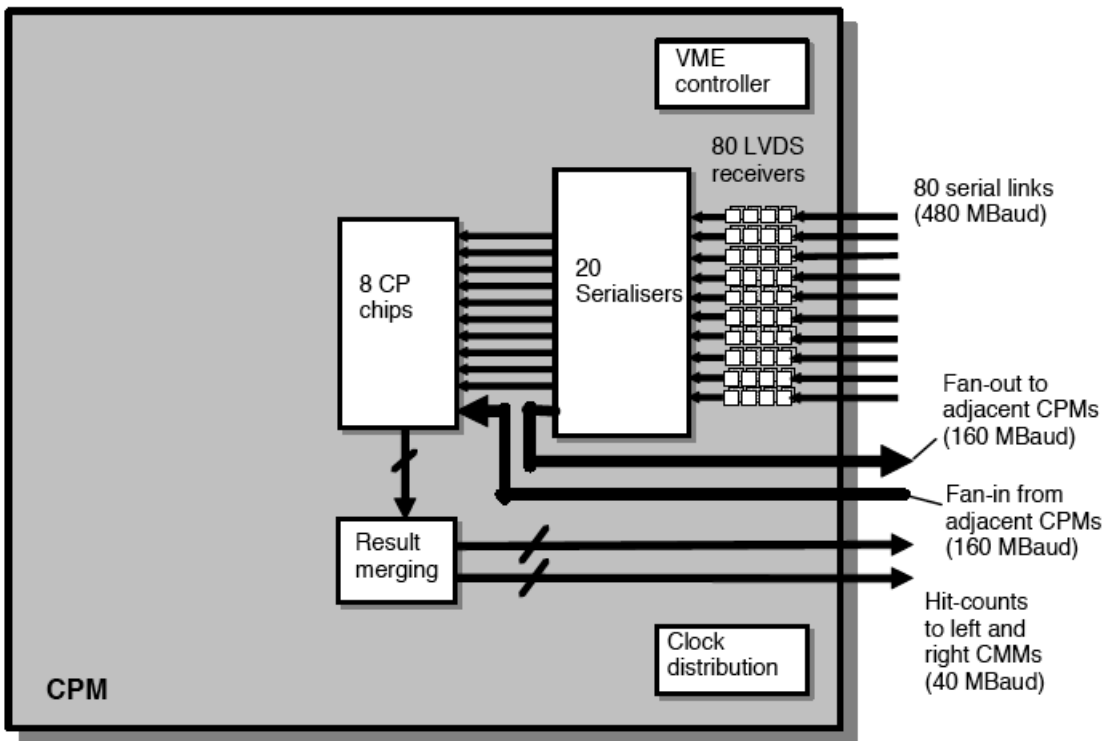

Figure 4.2: The real time data path in the CPM(42). On the right hand side the data arrives from the PPM on 80 serial links at 480 Mbit/s. The fan in and out from adjacent CPMs is also shown as well as the output to the CMM.

4.1.2 The Common Merger Module

Located in every crate in the Cluster Processor and Jet Energy Processor systems is another type of module called the common merger module (CMM). The CMM's purpose is to collect the 3 bit multiplicity count results for each threshold from the CPMs or JEMs that are sent to it over the crate backplane, add them together and then forward the results (with a parity error bit) via a cable to another CMM. This CMM sends the data, that represents the final results of the level-1 calorimeter trigger, to the Central Trigger Processor to make the first level trigger decision.

As described above a CMM can act in two ways. The first type of CMM is known

as a Crate CMM as it collates the results from the CPMs or JEMs in a crate. The second type of CMM is know as a System CMM as it collects the results from all the Crate CMMs. The hardware of both the Crate and System CMMs is identical and they are interchangeable. The flow of logic is different depending on its function as illustrated in figures 4.3 and 4.4. What is important to note in figures 4.3 and 4.4 is that each of the backplane inputs from each CPM/JEM or CMM has the signal parity checked. The results of all the parity checks are recorded as an error count and also as a map that shows from which input(s) the error originated. The relevant registers on the CMM where these details are stored are the Backplane Parity Error and Cable Link Parity Error registers (43). When describing the calibration of the CMM in section 4.2 the full use of the parity error counter and map will be explained.

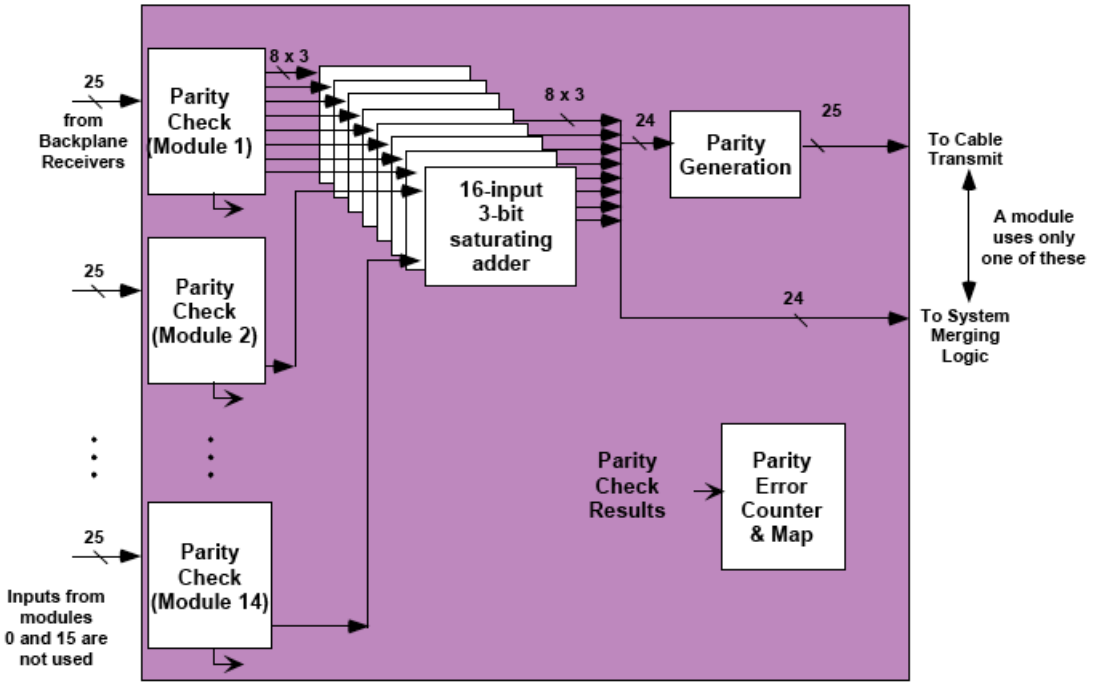

Figure 4.3: The flow of logical operation in a Cluster Processor Crate CMM(43).

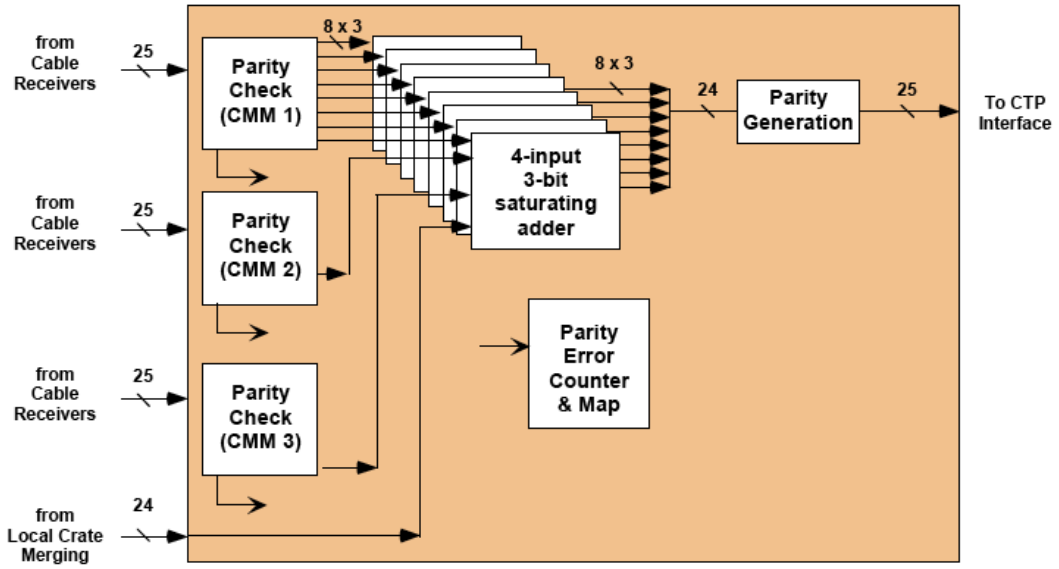

Figure 4.4: The flow of logical operation in a System CMM(43).

4.2 The CMM Timing Calibration

As part of the effort to ensure that the trigger will be set up correctly, work has been done to ensure the timing calibration of the data signals sent over the backplane to the CMM. These signals are important as they contain data sent from JEM/CPM modules and must be timed correctly for the processor to work. The CMM calibration procedure has therefore been built to ensure this. Before considering the CMM calibration in detail it is best to examine the general procedure for calibration runs. This serves as an introduction to the various steps needed in a calibration run.

4.2.1 A general calibration run

A calibration run involves several stages such as running modules with known settings, analysing the results to produce calibrated settings and finally storing the calibrated settings so that they can potentially be used in the future. The analysis stage is specific to the module undergoing calibration but the mechanisms for stor-

ing the results in a database and retrieving them are universal. A special form of database known as a conditions database[1] is being used to store the data from a calibration run. For ATLAS and the other experiments the structure of the conditions database being used is defined by the COOL software (48). The COOL software allows users to read and write data into a chosen database, in a consistent manner, so that the data interval of validity, insertion time and version are recorded. This allows a record of the history to be kept and a clear indication of which settings are to be currently used as is required in a conditions database.

4.2.2 Why and how the timing of the backplane signals must be calibrated on the CMM

For every signal that the CMM receives over the backplane from a CPM/JEM the data must be read at the correct time to ensure no errors. It is the timing of these signals that has to be calibrated to ensure this always happens otherwise data will be corrupted and lost. The calibration is done using the parity error bit that was sent with the 3 bit multiplicity count. An example of the signal that is transmitted over the backplane between a CPM and CMM is shown in figure 4.5 (a). When a module such as the CMM receives the signal it must first interpret the high and low voltages, that represent binary bits, back into a binary register format so that it can be stored and saved for later processing. It is at this point that corruption of the data could happen.

Normally the rising edge of a clock signal is used to mark when the transmitted data signal should be read. At the LHC the most convenient clock to use would be the LHC clock that is distributed via the TTC system to the rest of the experiment (figure 4.5(b)). As it is not only the receiving CMM that uses this clock to receive

[1] A definition of a conditions database is one which stores "non-event detector data that vary with time". The timing data so far described is exactly this kind of data and as such a conditions database is required.

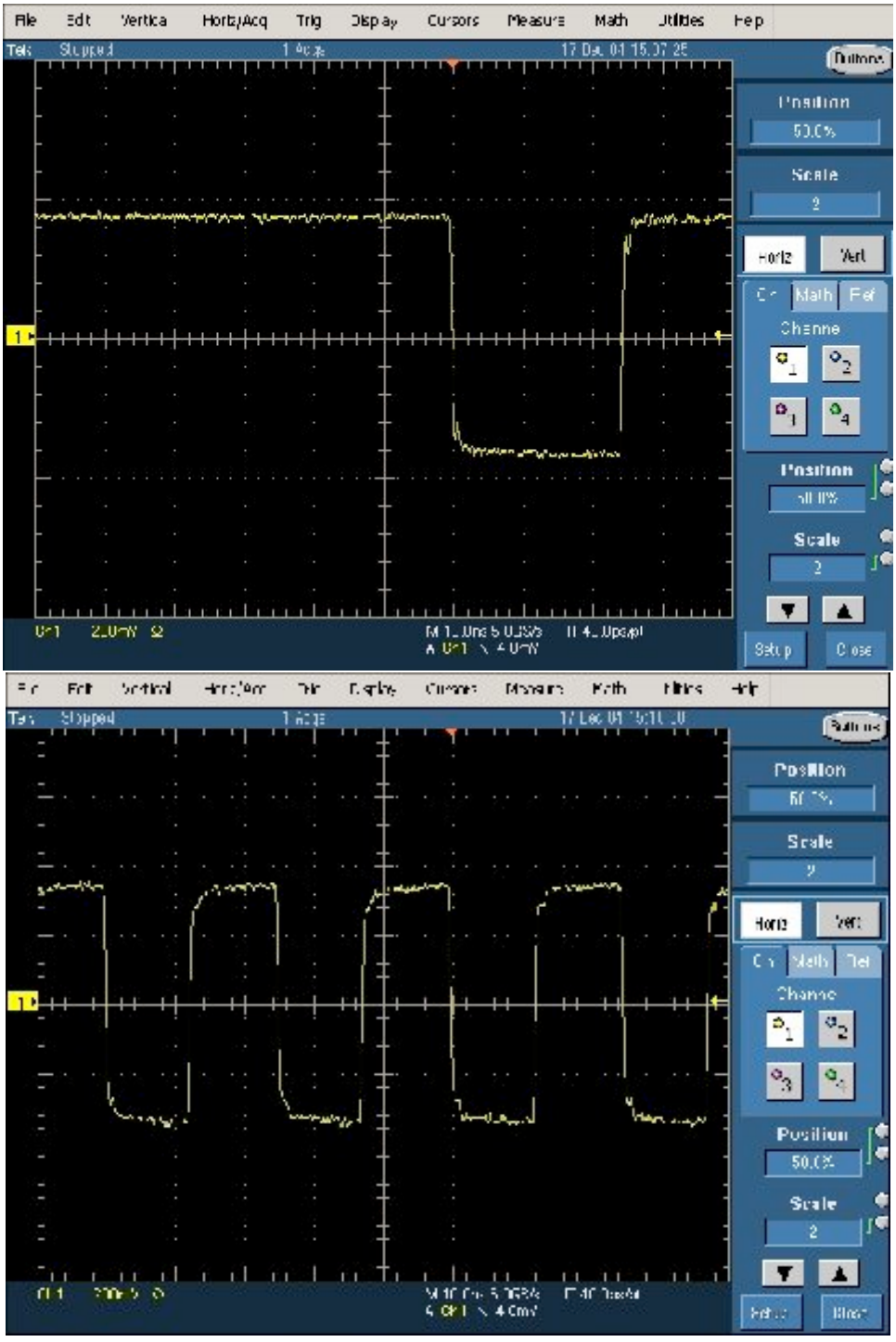

Figure 4.5: (a) This is part of a signal transmission to the CMM. The binary aspect of the signal can be seen as either being high or low. (b) The LHC clock signal. (Picture from N.Gee)

the data signal but also the transmitting module, this ensures that there is a degree of synchronisation between the two modules. There is however one problem with this approach that occurs if the rising clock edge should fall into the transition region which is neither up nor down in the data signal. This could indeed happen as it is possible for the data signal or clock to drift relative to each other or different path lengths may result in offset signals. This situation is avoidable though as it is possible to move the clock signal in integer steps of 104 ps and also change, for each of the CPM/JEM input signals, the overall phase of the clock in quarter phase steps. It would therefore be feasible to choose a non-transition location to perform the translation. It can perhaps now be clearly seen that what is meant by calibrating the CMM is simply to ensure that the signals received are strobed in a good region by selecting the optimum position for the clock (see figure 4.5 where the rising clock edge in the bottom plot is ideally located to read the data signal above). The rest of this section therefore devotes itself to explaining how the error free timing window in the data signal is found and how having found it, the best clock timing is selected.

4.2.3 Mapping the timing of the backplane signals with a multistep run

In order to perform a calibration run on a CMM it is desirable to use simulated data for reasons of control, simplicity and independence from the rest of ATLAS. The level-1 calorimeter collaboration have therefore written code that allows all the modules to be simulated as though they were running with data. An interface to all these programs then allows the user to select which modules in the system to make active and the type of data that they should use. For instance one relevant case is the population of CPMs with data and then allowing the processed results to be sent to a CMM module. Settings such as whether the clock phase is to be incremented and the number of steps to do this for is also set here. It is this feature that allows the data signals to be mapped because the CMM clock is incremented

over a number of steps corresponding to a complete clock cycle. This is known as a multistep run.

The precise nature of how, for each step, the data signal is analysed can be described as follows. The parity error counter, for each step, is read out from the Backplane Timing register (43) to see if any errors are present. If an error should be found it signifies that the signal is being read from a region with errors. The error and error-free regions in the signal can then be obtained by analysing the results from each step.

The method of using just the parity error counter as stored in the Backplane Timing register is only efficient if one CPM/JEM is sending data over the backplane to the CMM. When the crate is full there will be 14 or 16 CPMs or JEMs respectively sending signals to the CMM at the same time. If the data from more than one CPM gives an error this counter would simply give the sum of those errors and there would be no way to differentiate between modules by looking at the counter. This would mean that for every CPM in the crate a multistep run would have to be done. One of the aims of a calibration run is to calibrate quickly and time would be lost by doing a multistep run for each CPM/JEM in a crate. However, the map register on the CMM records from which slot in the crate (i.e. which CPM/JEM module) any parity errors come and thus it is the better tool. The overall picture can be found from just one multistep run. There is a drawback with this solution in that no details of the transition (between error-free and having an error) is obtained for the respective modules. For the case of debugging and observing changes with time it may be of interest to plot the onset of errors and any anomalies. However, for the purposes of the calibration this is not important as the overall aim is to place the strobe timing as far away as possible from the transition points so the boundaries of the error-free windows are all that is required.

Both the map and parity error register on the CMM are cleared every time the timing is changed so it is important to record this information for each step of

the multistep run. A special "crate readout" program is used to place previously specified register settings into a monitoring stream[2] at the end of each step. An analysis program listening to the crate readout program picks up the relevant parts of the monitoring stream, for example the map register, until a signal indicates that the multistep run has ended. Upon the end of the multistep run the collected data is analysed to determine where the error-free windows are for each of the signals sent to the CMM and the calibrated settings are generated.

4.2.4 Analysing a timing window: Reconstruction, Calibration Settings and Verification

As soon as the multistep run has been completed the data should have been obtained to construct the timing windows for all the CPM/JEMs in the crate. For each CPM/JEM input signal the windows are then analysed. The analysis of each window begins with a simple algorithm to locate the opening(s) and closing(s) of the error-free part of the window. Once these have been established checks are performed to establish what kind of timing window has been obtained. This has to be done because it is possible to have different configurations of timing window depending upon where the window's opening(s) and closing(s) are. As shown in figure 4.6 six types of window are generally possible. What is also indicated in this diagram is where the window opening is defined for the different window types. In general this opening is defined as where the error-free part of the window commences. However, particular care should be reserved for the case when the window wraps round as in figure 4.6(b) because here the window opening is to the right of the window closing. This occurs due to the signal not being synchronous with the 25ns clock. Two of the possible types of windows would signify that an error has occurred. The

[2]The monitoring stream is a specially structured stream of data. It has headers and footers so you know which module you are dealing with and the words corresponding to each module appear in a previously designated order.

window in figure 4.6(e) would indicate that the CPM/JEM signal was not reaching the CMM while the other kind of window in figure 4.6(f) with more than two error free windows would indicate that something was wrong in the hardware or from the multistep run. In both cases the program would flag the data as bad. However, regardless of the type of window, all data is output into a histogram at this early stage of the analysis so that it is made persistent. If the window is found to be one of the other types in figure 4.6 (a,b,c or d) then the analysis would continue by producing the calibrated settings to be used by the CMM. These calibrated settings consist of the "best" position for each CPM/JEM input signal and also if any overall phase shift in the Clock40Des1 clock is required. The "best" position is defined in a twofold action. Firstly, any timing pointer position that is in the error free part of the timing window is considered as a candidate. A second check then determines which of these is furthest from the transition edges and this is chosen as the "best" position.

The collection of best timing position settings for the signals from all the CPM or JEM modules in a crate form a set of non-verified calibrated settings for the CMM. Before using for real data taking, the calibrated settings should be verified. Decisions must be made to see whether or not the calibrated settings appear reasonable and if they are better than previously used ones. This safeguard of checking the reliability of the calibrated settings is a necessity because an error could have occurred during the calibration run leading to abnormal data or some factor could have caused the timing window size to move or shrink considerably. In both cases it would be highly undesirable to load the newly found calibrated settings back into the module and further investigation would be required to ascertain the cause of the problem. Verification procedures, that compare some of the features of the current timing window to those obtained in previous calibration runs, are used to do this. The precise algorithm of any verification procedure will require extensive experience with the final setup of the hardware and this was not feasible when working on this prototype. However, this final stage of calibration is important as it determines

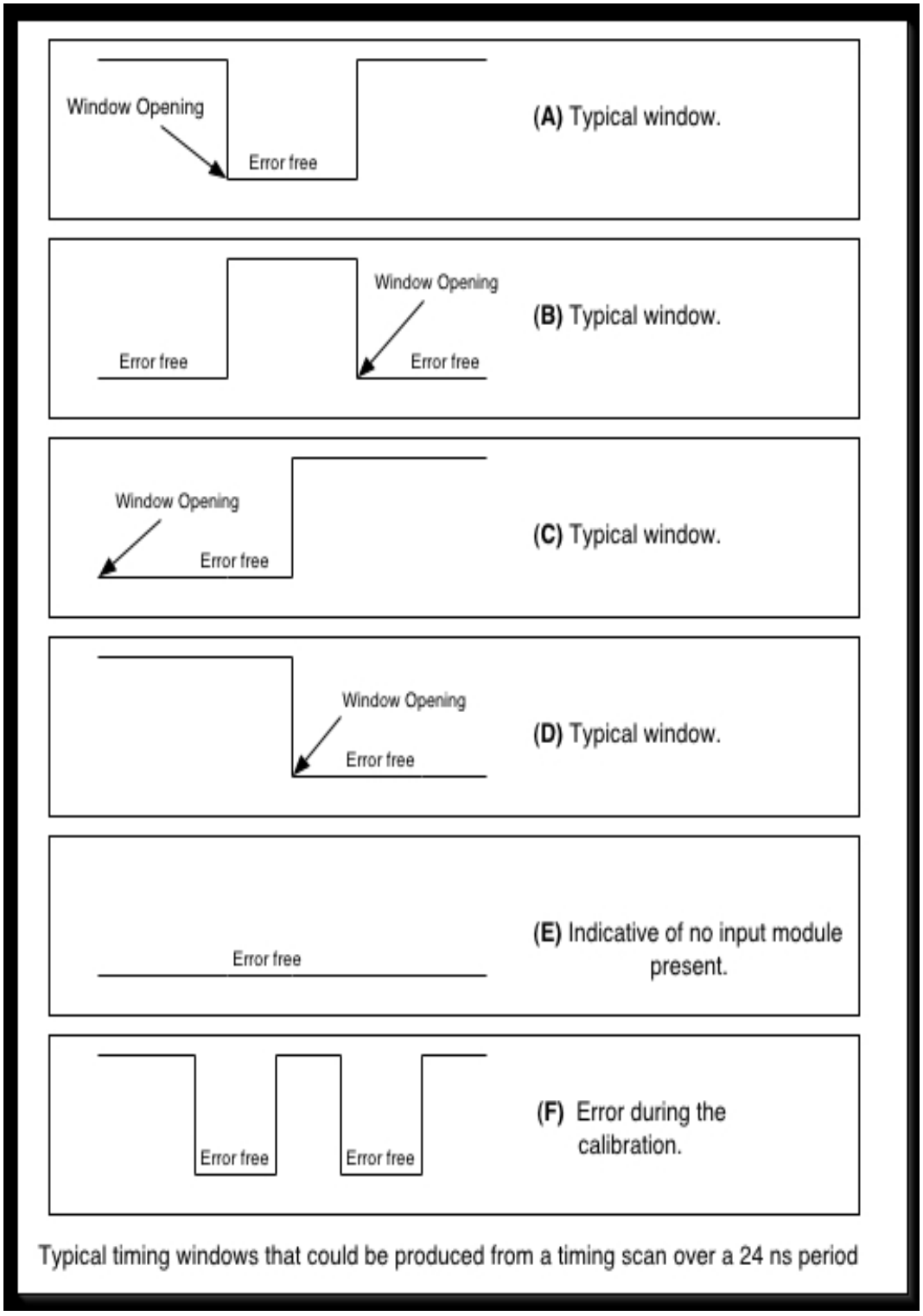

Figure 4.6: The different types of timing window produced from a multistep run.

whether the settings represent a good set of data and so should be used.

4.3 The stability of the CPM at various temperatures

The CPM module has undergone rigorous design and testing. However, in addition to these tests it was important to check that the module as a whole would be unaffected by temperature variations. Such temperature variations are a possibility due to the heat output of all the neighbouring electronics or fluctuating crate cooling causing the temperature of a CPM to vary from normal conditions. This section therefore reports on the steps taken to check that the CPM works reliably over an ambient temperature range from 5^0C to 50^0C. In particular the data transmission to and from the CPM and the clock jitter[3] were studied.

4.3.1 Method of measuring CPM temperature stability on the CPM

As described previously the CPM receives preprocessed data from the calorimeter, analyses that data with algorithms programmed into its Field-Programmable Gate Array (FPGA) chips, and then transmits its findings down the chain. Test systems have been established in order to simulate the data that is transmitted to the CPM and to verify that the algorithms do indeed process the data as required at ATLAS. Of particular interest in this process is the 'scanpath' debugging tool which tests whether initially known data sent through the CPM, to the point just before it is processed by the CP chips, is corrupted. This was known as a 'data test'. The

[3]The jitter in a clock is a measure of how the leading or trailing edge varies from the nominal timing on a cycle-to-cycle basis.

functioning of the algorithms and further parts of the CPM board were also tested by running the data through the CP chip and looking for parity errors. The output of both of these tests was an error count (represented by a number greater than zero) or no error (a zero result). In a similar way as described for the CMM calibration multistep run the output of both tests was examined at several points over the 25ns clock period. From this it was possible to produce the error-free windows which indicated where the signal could be strobed. However, unlike in the case of the CMM calibration, the issue was not where to set the strobe, but to check that the size and position of the error-free window was relatively stable and constant with varying temperature. It should also be remembered that the data sent through the CPM, in the 'scanpath' test, is at 160 MHz. This is four times the normal 40 MHz LHC clock rate and will thus give four error-free windows over the 25 ns period examined. These error-free windows are thus narrow and it is important to ensure that the widths of the windows are not shrinking or moving with different temperatures. In addition to checking the size and position of the error-free window these tests enabled checks to be performed on the clock stability. If the clock used to strobe the signal has a jitter that is comparable to the size of the error free window then the data would not always be read out correctly. Therefore, since these tests can check the correct functioning of the CPM, it is natural that the temperature testing of the CPM was based on them.

Under normal operation the CPM is linked to the test system via the crate backplane, this could not be done as the ambient CPM temperature was regulated precisely in an environmental chamber. Therefore, a special connection consisting of two Printed Circuit Board's (PCB) joined by a ribbon cable was designed to bridge the gap (see figures 4.7 and 4.8). The environmental chamber proved ideal for heating and cooling the CPM to a specific temperature. To confirm this temperature was as set on the oven an independent temperature probe was placed above the CPM.

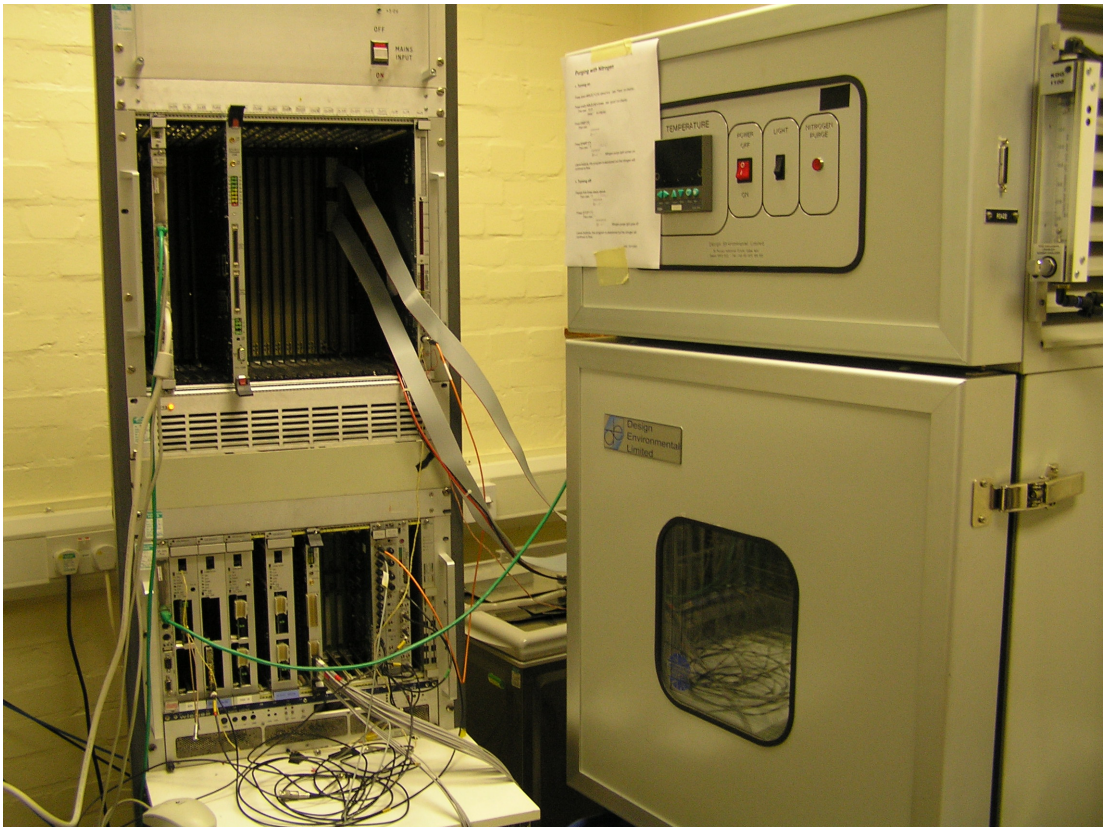

Figure 4.7: The crate and environmental chamber which housed the CPM.

Initially, although this configuration allowed the transmission of data, when the error-free windows were examined multiple error spikes appeared. However, this problem was drastically reduced by attaching a grounding cable from the crate via the oven to the CPM. This gave enough functionality to run the tests. The problem was not completely eliminated and a few randomly changing spikes remained. This was believed to be due to the special out-of-crate configuration as under normal operation the error-free window was error-free.

4.3.2 Results of the CPM temperature test

The designed system allowed the data and parity tests to be performed. In addition to this the TTC clock signal was recorded from the front-end clock output of the

Figure 4.8: Above: the VME cable connected to the back plane. Bottom: the CPM in the environmental chamber.

CPM in order to measure its jitter. The clock jitter, although showing an increase with temperature, was never greater than 10 ps and had a negligible effect on the 25 ns period clock.

One of the effects of increasing the temperature was that the positions of the error free windows from the scanpath test were shifted. This effect is shown in figure 4.9 which illustrates the extremes of the shift at 5 ^{0}C and 50 ^{0}C. This shift had been expected due to the performance of the electronics on the board changing with temperature. By studying the average shift of each of the four error regions[4], in the range of 5 ^{0}C and 50 ^{0}C, a global drift value of approximately 500 ps was found.

The results of the previous data tests were checked by examining the parity test. The parity 'error free' window was shifted by a change in temperature but as before the width remains reasonably constant.

4.3.3 Conclusions of the CPM test

Both tests, with data and parity error, have revealed that there are changes with temperature occurring in the CPM. However, the main conclusion from the CPM test is that although the CPM is affected by temperature it will operate reliably over the 45 ^{0}C range tested. These tests suggested the hypothesis that the shifts may be mainly due to the Timing Trigger and Control TTCrx ASIC chip on the CPM. This is the component on the CPM from which all components get their timing signals. As the TTCrx chip is used on many modules in the L1 calorimeter trigger it is important to understand this effect further in case other modules are also affected. An investigation into the temperature dependence of the TTCrx ASIC is described in the following section in order to test the hypothesis that the timing

[4]To define the average shift the central point, between the lower and upper boundary with the error-free window, in each of the four error regions was used.

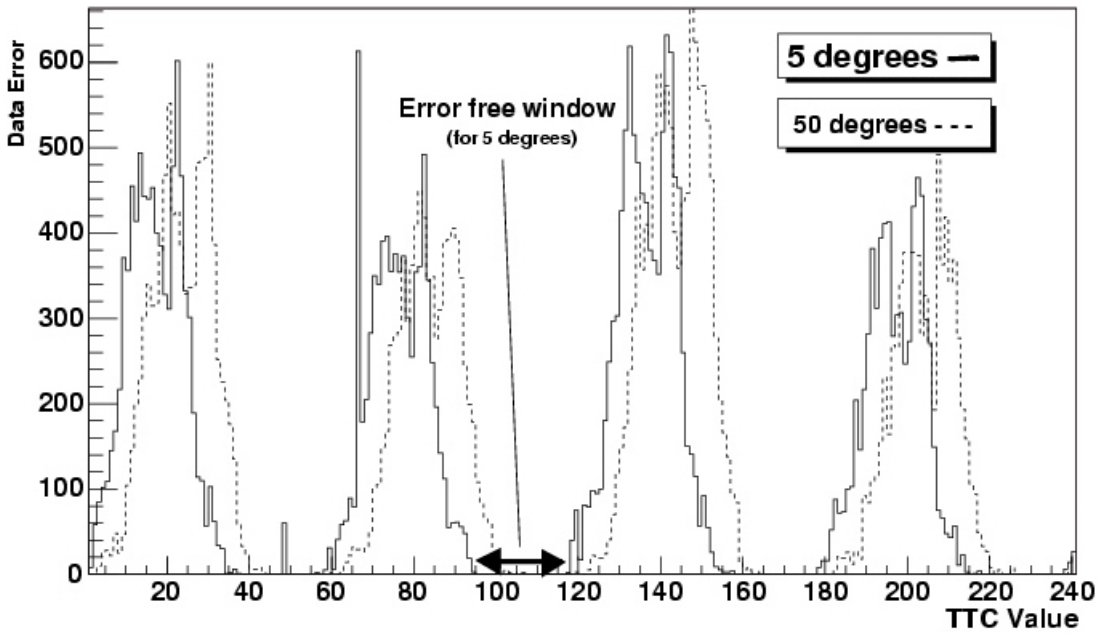

Figure 4.9: The errors from data passed through the CPM when operated at 5 ^{0}C and 50 ^{0}C. The four peak pattern observed in this figure is due to the scan being over a period of 25 ns with the data received having a period of 6.25 ns.

shifts originate from the TTCrx ASIC.

4.4 Temperature effects on the TTCdecoder card

In previous work (49; 50) it was suggested that the TTCrx ASIC is affected by temperature variations. The two clocks, Clock40Des1 and Clock40Des2, that are output from the TTCrx chip are examined here to ascertain their stability. Primarily the phase of Clock40Des1 was studied in order to observe how it shifted with temperature over a temperature range of 40 ^{0}C. In addition to this, the relative shift in phase between Clock40Des1 and Clock40Des2 was examined over the same 40 ^{0}C range. For the purpose of simplicity in the testing it should be noted that it was the TTCdecoder card, which contains the TTCrx ASIC, that was tested. Since each individual module of the level-1 trigger carries its own TTCdecoder card,

8 TTCdecoder cards have been tested in order to examine the spread due to the variability between different TTCrx chips.

4.4.1 Method to check for temperature variation of the TTCdecoder card

The environmental test chamber was used, as described for the temperature testing of the CPM. An independent temperature probe was also used to measure the local temperature in the environmental chamber.

Under normal operation the TTCrx chip is mounted on a board called the TTCdecoder card that is in turn plugged into the trigger modules as a daughter board. For this test the TTCdecoder card was instead placed on a TTCfanout module, which may serve as a TTCdecoder card testing platform (51). The differential TTC signal that the TTCdecoder card used as an input was obtained from a mock TTC system used for testing called the TTCvi. This was input to the TTCrx chip via a buffer on the TTCdecoder card. The reference clock was also retrieved from the TTCvi system but sent directly to an oscilloscope without going through the oven (see figure 4.10). In addition to this setup two oscilloscope probes were attached to the Clock40Des1 and Clock40Des2 outputs on the TTCdecoder card.

4.4.2 Results from the TTCdecoder temperature test

The variation of Clock40Des1 as a function of temperature is shown in figure 4.11 and table 4.1. No non-linearity was observed and the average linear coefficient was 55 ps / ^{0}C with a spread on all 8 cards of less than 10 percent. This result differed from that measured previously (49) of 34 ps/ ^{0}C but it should be noted that in the current test the latest radiation-hard version of the TTCrx ASIC was being used unlike in the previous measurement.

TTCdecoder card	Coefficient
1	0.056±0.002
2	0.055±0.002
3	0.060±0.002
4	0.052±0.002
5	0.056±0.002
6	0.054±0.002
7	0.053±0.002
8	0.052±0.002

Table 4.1: The temperature coefficient for each TTCdecoder card (ns/^{0}C).

The relative phase of Clock40Des2 compared to Clock40Des1 was also measured when set to be offset by 0, 1/4, 1/2 and 3/4 of the period and found to be constant for each measurement over the 40 ^{0}C range tested (figure 4.12). This confirms that the temperature affects both clocks equally as would be expected. What can also be seen from figure 4.12 is that for each phase measurement made the timing differs from one TTCdecoder card to another by approximately ±1 ns.

4.4.3 Conclusions on the TTCdecoder temperature test

The temperature testing of the TTCdecoder card has revealed that there are changes with temperature occurring in Clock40Des1 and Clock40Des2. It has been shown that Clock40Des1 drifts with temperature at a rate of 55±2 ps per ^{0}C. It has also been shown that the relative phase of Clock40Des2 is stable against Clock40Des1. This lack of drift between the two clocks shows that Clock40Des2 changes at the same linear rate as Clock40Des1 with temperature. This is important for trigger modules as the timing of input data requires that the relative phase of the clocks should be as stable as possible.

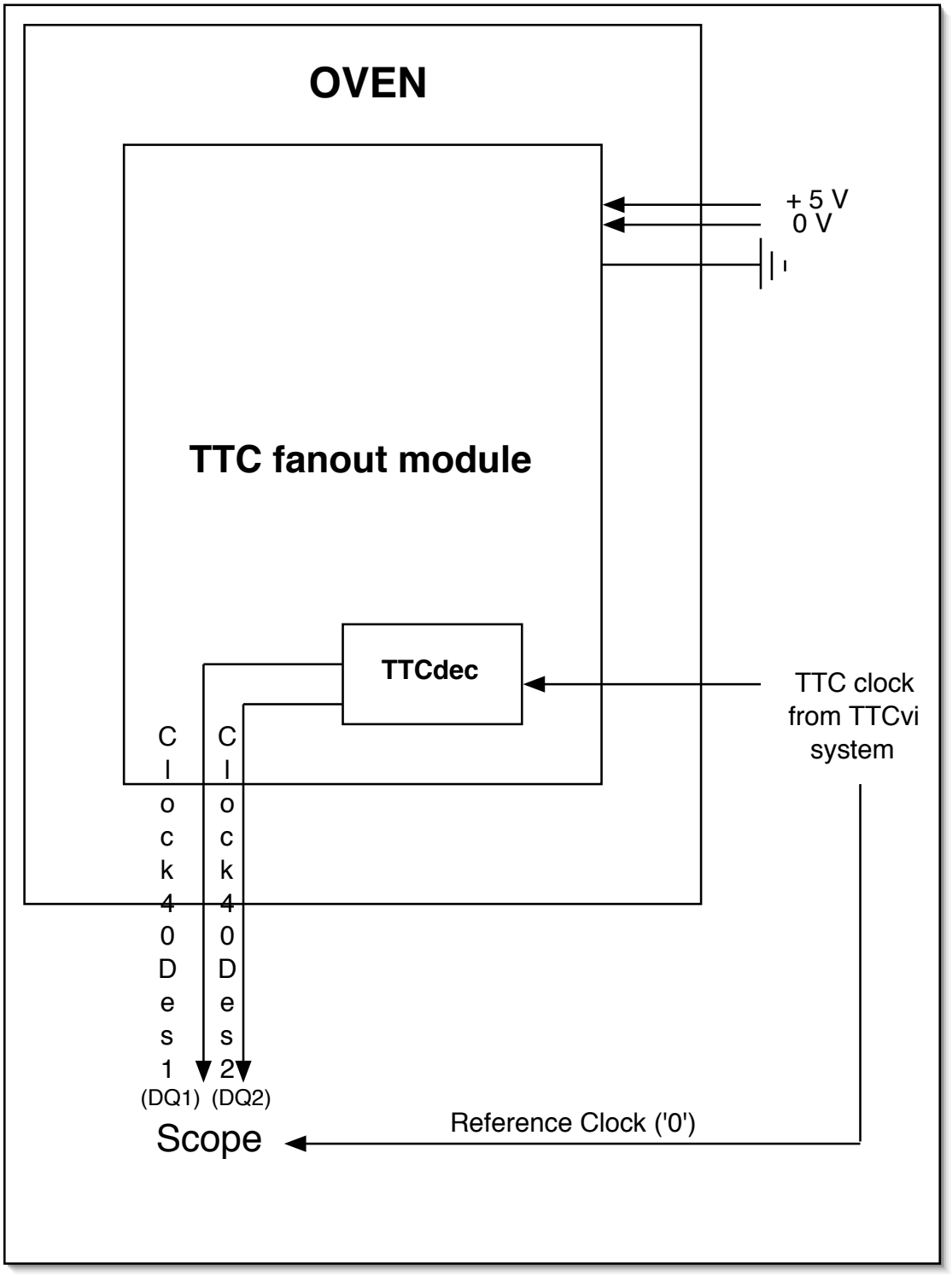

Figure 4.10: The experimental set up of the TTCdecoder card that contained the TTCrx ASIC chip.

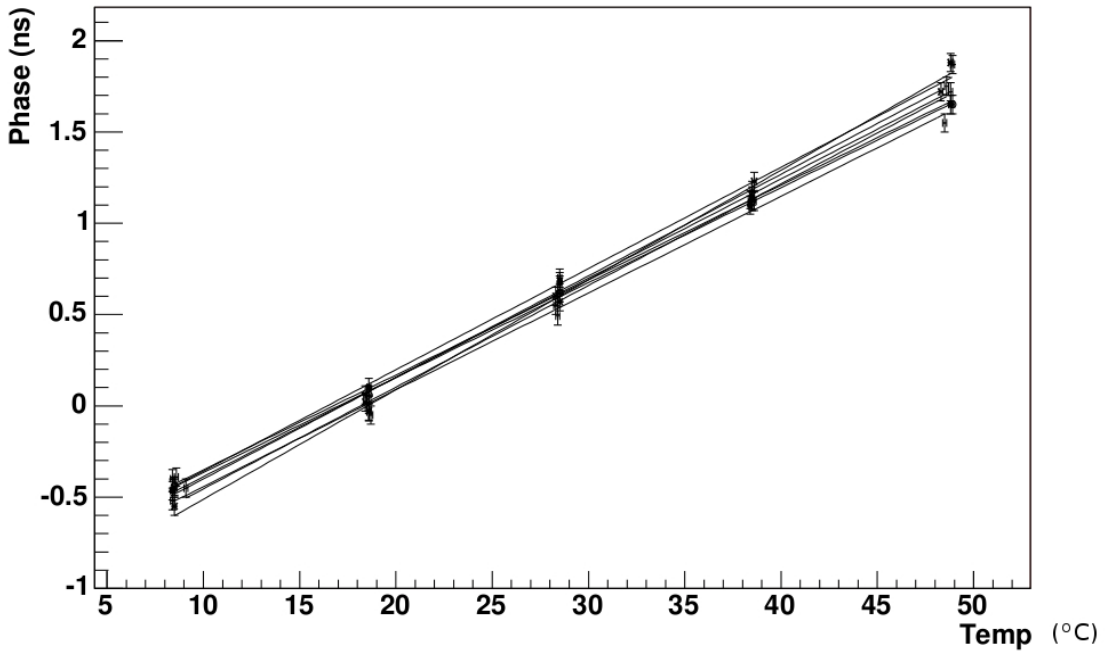

Figure 4.11: Drift of Clock40Des1 with ambient temperature, relative to the stable reference clock, for the 8 TTCdecoder cards studied.

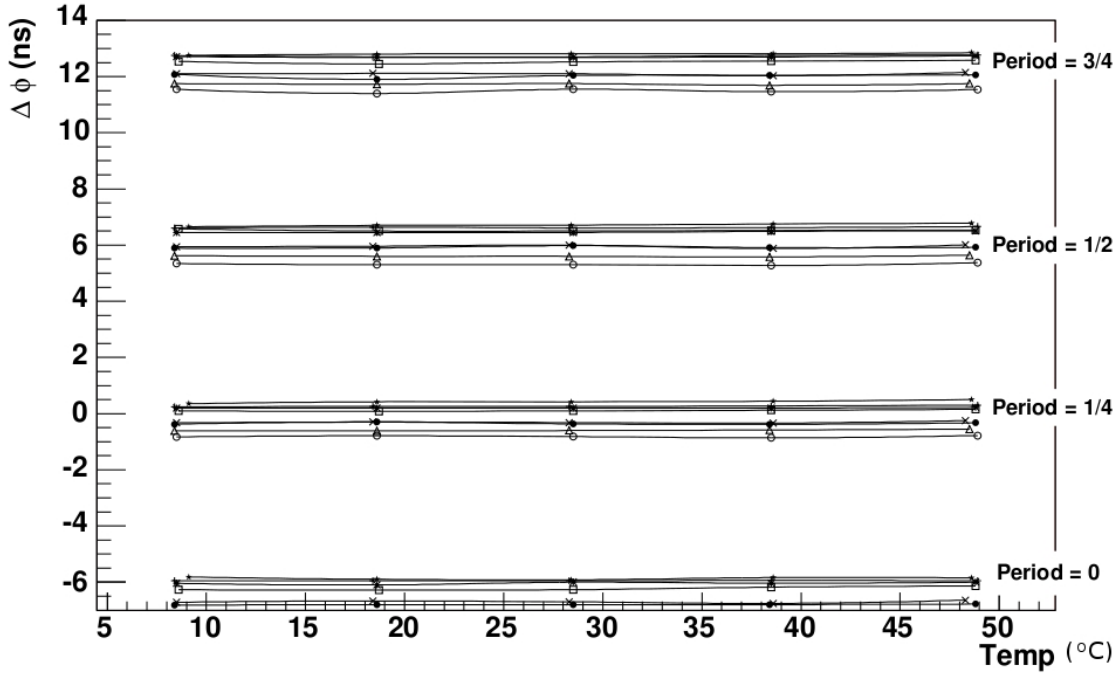

Figure 4.12: The difference in phase $\Delta\phi$ of Clock40Des1 relative to Clock40Des2 for the eight TTCdecoder cards studied.

Chapter 5

Simulating the signal and background

The purpose of this chapter is to describe the general methodology that was used to generate and simulate the $W\gamma$ signal and background datasets. More detailed information is also included on how the signal datasets were generated. This was included because a relatively new Monte Carlo generator with a customised anomalous triple gauge coupling model had to be used to represent accurately the physics of producing a $W\gamma$ event with next-to-leading log (NLL) accuracy. A NLL prediction differs from a full NLO prediction in that although the event shapes are comparable the normalisation is not (52; 53). The implication of this for the user is that a separate calculation is required to get the prediction for the event rate.

5.1 Producing the signal and background

Since there have been no collision events observed yet by ATLAS all the data within this thesis was simulated. This task was made easier by the fact that the ATLAS collaboration centrally simulates a substantial number of potential signals and back-

grounds (see table 5.1). However, no suitable datasets were available that described the signal so the $W\gamma$ events used in this thesis were produced outside the main production system. As several signal samples, with varying anomalous couplings active, were required it was necessary to harness the distributed computing power of The Grid (54). It should also be noted that although the signal samples were independently produced the same tools and software packages were used as for the centrally produced background datasets.

Process	ATLAS Dataset Number	Cross Section (pb)	Number Of Events
$t\bar{t}$	5200 (semi-leptonic)	461	593600
W+jet	5270 (elec), 5271 (mu) and 5272 (tau)	5.38	198492
Z+jet	5185 (elec), 5186 (mu) and 5187 (tau)	44.6	175000
Zγ	5900	3.77	10000

Table 5.1: Table of cross sections for the background processes. The number of generated events is also given.

In general the simulation of the data is a lengthy procedure that is composed of several stages: generation, simulation, digitisation and reconstruction. As each dataset used in this study has undergone this procedure of being simulated it is important to understand, in principle at least, what occurs at each stage.

5.1.1 Event generation

The collision of two protons and the resulting physics is modelled at the event generation stage using a Monte Carlo generator (55). However, the collision of two relativistic protons is a complex process and the physics is not fully understood. Event generators overcome this problem by splitting the collision into several manageable parts such as:

1. Describing the hard process (e.g. $q\bar{q}\rightarrow W\gamma$) with matrix elements.

2. Dealing with particles decaying e.g. $W \rightarrow l\nu$.

3. Initial and final state parton showers.

4. Multiple interactions and beam remnants (to model the underlying event).

5. Hadronisation of partons.

Each step is still difficult to perform and different Monte Carlo techniques have been devised to get around the various difficulties. The PYTHIA (56) Monte Carlo program contains a treatment for merging the matrix elements and parton shower models together. However, this approach has been shown to be much more complex to implement as the number of final state particles is increased (57). For the purpose of this study PYTHIA-produced datasets were used for all the backgrounds except for $t\bar{t}$. For the $t\bar{t}$ sample a more sophisticated generator called MC@NLO (58) was available that could match the parton shower to the NLO matrix elements. In the case of the signal a specialised generator was required that could incorporate anomalous couplings and give at least a NLL description. A discussion on the various possibilities for generating the signal and the choice made is included in section 5.3.

Features within all of the Monte Carlo generators used also allow a number of criteria to be placed upon the events being generated. These range from the obvious requirements such as what are the final state particles to whether kinematic or spatial restrictions are to be applied. Ideally no kinematic or spatial requirements would be required but it should be noted that to pass 50 generated events through the chain of generation, simulation, digitisation and reconstruction takes of the order of 1 CPU day. If the area of physics that is to be studied is in a region which is sparsely populated then it is preferable to bias event generation towards a desired region to save time. In the case of this study the area of interest is in the tail of the photon transverse momentum distribution and therefore a minimum $P_T^{\gamma} > 80$ GeV cut was always applied. Regrettably some of the generation cuts applied to the background datasets resulted in producing jets (that have the potential to fake

a photon) with a $P_T > 100$ GeV. In the study of triple gauge couplings, especially at low luminosity, this is slightly high. In general this issue could not be overcome as these datasets had not been produced by the author and it was impractical to produce more in sufficient quantities.

5.1.2 Detector simulation and Reconstruction

The generation stage constructs the four-vectors of the emerging particles from the collision. However, it is also necessary to model the interaction of these particles with the detector and how the detector will identify them in order to reconstruct them. For this purpose the GEANT4 (59) detector simulation software is used to simulate how every particle interacts in the detector. This includes simulating the scattering, the particle production and the response of the active parts of the detector for each particle. As the GEANT4 simulation is continually being improved the description of the detector model used in this study was ATLAS-DC3-05 (60). The results from the simulation stage are then digitised so that they appear identical in form to the real data that will be produced by ATLAS. By taking the data in this digitised form it is possible to apply the same reconstruction algorithms as will be applied to real data. These reconstruction packages are designed with specific purposes such as identifying and recreating the track of a charged particle passing through the inner detector or finding clusters of energy in the calorimeter. Finally, after this stage has been completed the data is recorded in Analysis Object Data (AOD) format. The AOD contains both detector information and a record of the physical objects in the event such as the number of electrons. A specially designed analysis framework allows the user to run over the AOD and perform a physics analysis.

5.2 An introduction to the backgrounds and how they were generated

The main aim of this section is to introduce the backgrounds and to state how they were generated.

5.2.1 $t\bar{t}$ background

The $t\bar{t}$ background was generated with MC@NLO. The top quarks were allowed to decay semi-leptonically through the electron, muon and tau flavours. With over half a million events corresponding to approximately $1 fb^{-1}$ there are enough events that contain a photon-like object. The presence of the W decaying leptonically is also a common event characteristic shared with the $W\gamma$ signal.

5.2.2 W+jets

The generation and simulation of the W+jet background was performed as part of the standard ATLAS production and modelled using the PYTHIA subprocess $f_i\bar{f}_j \rightarrow gW^{\pm}$ and $f_i g \rightarrow f_i W^{\pm}$. A kinematic cut of 100 GeV on the hard $2 \rightarrow 2$ process was also in place to simulate the required area of phase space. Although it would have been ideal to obtain a dataset with a lower hard $2 \rightarrow 2$ process cut and thus cover all regions of phase space it was not possible with the computing facilities available due to the increased number of events that would have to be simulated. However, as the jet is the main source of the fake photon then this kinematic cut is reasonable when looking only at photons with $P_T > 100$ GeV.

This background has the potential to mimic the signal when a jet is misidentified as the photon. Ensuring good jet rejection through photon identification cuts is essential. It is also important that the lepton (in particular the electron) does not

fake or radiate a photon but this is generally suppressed by the requirement of one cleanly identified lepton in the preselection cuts found in section 7.1. This is the main background.

5.2.3 Z+jets

This background was generated as part of the standard ATLAS production using PYTHIA with subprocess $f_i\bar{f}_j \rightarrow gZ^0$ and $f_ig \rightarrow f_iZ^0$. A 100 GeV kinematic cut on the hard $2 \rightarrow 2$ process ensured that the correct region of phase space was generated for the same reasons as specified in the case of W+jets.

This background can fake the signal in two ways. Predominantly the jet can fake the photon while an electron or muon may not be detected, thus faking the neutrino. Alternatively an electron or muon can be misidentified as a photon. For this to occur and the event to pass the missing transverse momentum (P_T^{miss}) preselection cuts means that the jet must be lost. However, the requirement of only one electron/muon and also $P_T^{miss} > 15$ GeV means a large percentage of these events are vetoed in the preselection cuts (see section 7.1).

5.2.4 $Z\gamma$

The process was generated as part of the standard ATLAS production using PYTHIA with the Z forced to decay leptonically. This background has similar characteristics to the signal if a lepton is either not found or is misidentified as a photon. As the cross section for this channel is similar to the $W\gamma$ cross section, this background has been examined and found to be only a small contribution as the P_T^{miss} cuts in the preselection remove it (see section 7.1).

5.2.5 Other negligible backgrounds

In addition to the backgrounds mentioned there are also γ+jet, and $b\bar{b}$ backgrounds. The γ+jet fakes the signal when the jet is misidentified as an electron while the $b\bar{b}$ background can fake the signal due to its high cross section increasing the chance of a jet faking the photon. Previous studies (2) have shown that these backgrounds are negligible. These were therefore not included in this study.

The contribution of $W\gamma$ with $W \rightarrow \tau\nu$ was also considered here to be part of the background. Ideally this should be part of the signal process but it was not possible due to time constraints to generate and simulate $W(\rightarrow \tau\nu)\gamma$ datasets with the anomalous triple gauge couplings active as was required in order to make a prediction on the anomalous sensitivity. Therefore, it must be considered a background as it cannot be used in any prediction and must be vetoed. However, using a fully simulated SHERPA (19) dataset in the standard model limit, it was found to be negligible. This was due to the cross section being a factor of two smaller than the signal and the leptonic branching ratio of the τ suppressing it even further.

5.3 How to model $W\gamma$ at NLO

Several programs exist that can model the $W\gamma$ channel at NLO. However, only two programs, BHO (17) and AYLEN (3), include anomalous triple gauge couplings. Of these programs BHO has already been used at the Tevatron and in previous ATLAS studies, while AYLEN was written specifically with ATLAS in mind and includes decay angle correlations. Only minor differences could be observed between AYLEN and BHO, however, without actual data in the proton-proton regime of $\sqrt{s} = 14$ TeV it is impossible to tell which will fit the data best. Regrettably neither of these programs is interfaced to the parton shower generation and to create this interface was beyond the scope of this thesis. It was decided to investigate the relatively new

SHERPA (19) generator that is capable of a NLL prediction. This NLL prediction was found to provide a similar description when compared to the NLO AYLEN and BHO descriptions as is indicated in figure 5.1. Due to this and because SHERPA has the anomalous triple gauge model incorporated, is fully interfaced to the parton shower generation and is an official ATLAS generator, it was decided to use it for generating the signal. A total of 59350 events were generated in the SM limit, 31400 events for $\lambda_\gamma = -1$, 24250 events for $\lambda_\gamma = 1$, 11950 events for $\Delta\kappa_\gamma = 0.5$, 13550 events for $\Delta\kappa_\gamma = 1$, and 31350 events for $\lambda_\gamma = 1$ and $\Delta\kappa_\gamma = 1$.

5.3.1 SHERPA Monte Carlo

The approach taken by the SHERPA Monte Carlo to model physics lies at an intermediate stage between the PYTHIA and MC@NLO methods. While not wanting to take on the complexity of matching parton showers to full NLO theory but still requiring a better QCD radiation model than a simple merging, SHERPA compromises and matches the parton shower to leading order matrix elements. SHERPA can therefore describe X, X+jet, ... , X+n-jet processes and should give the same shape as the full NLO description. However, as leading order matrix elements were used, that by definition do not have virtual loop corrections, the cross section is only known to leading order. The normalisation thus requires a separate analytical calculation that can be obtained from either the BHO or AYLEN NLO generators. The precise implementation of the leading order matrix element matching to the parton shower in SHERPA is defined by the CKKW mechanism (52). This approach works by combining the various leading order matrix elements with the number of jets corresponding to the power of α_s of the matrix element. The jets are added in by re-weighting them and then applying a jet clustering algorithm.

Generating SHERPA events through the chain

Generating SHERPA events and placing them into the ATLAS framework differs from a typical ATLAS Monte Carlo, such as PYTHIA. In SHERPA the events have to be generated outside the ATLAS framework before being converted into the HEPMC format by an ATLAS conversion package (61). This implies that the Monte Carlo tuning is left to the user. In order to try to obtain consistency and the same optimised tuning as other ATLAS users, the options as suggested by ATLAS were used (62).

Details of the anomalous Triple Gauge Coupling model that has been incorporated.

The anomalous triple gauge coupling model that has been implemented by the SHERPA authors describes the general WWV vertex where V represents either a Z or γ boson. The precise implementation of this vertex which contains the off-shell contributions is documented in (16) and (63).

Accuracy of triple gauge coupling model: comparing photon P_T spectra and cross-section parabolae

In order to verify that the anomalous model in SHERPA was working several checks were performed to ensure its validity. The first test was to observe that the cross section prediction when either $\Delta\kappa_\gamma$ or λ_γ was varied changed parabolically. This is due to the cross section being proportional to the matrix element squared and the matrix element depending linearly on the anomalous coupling value, as discussed in chapter 2. With similar input conditions the leading order cross sections for SHERPA, BHO and AYLEN were compared and found to be in agreement. The event shape for the photon P_T distribution was compared to both the BHO and

AYLEN NLO generators (figure 5.1).

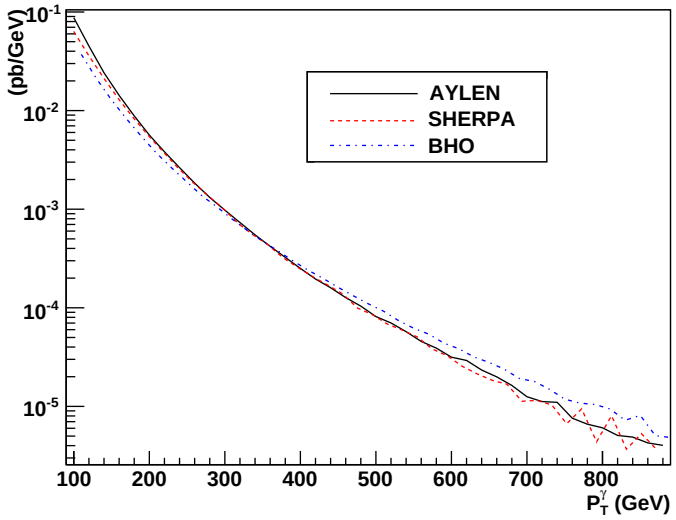

Figure 5.1: Photon transverse momentum produced by the AYLEN, SHERPA and BHO Monte Carlo generators. The SHERPA distribution, that predicts the NLO shape but only the LO cross section, has been scaled up to the AYLEN distribution with a constant scaling factor.

Chapter 6

Particle ID, Signal and Background characteristics

This chapter will introduce the key methods for the identification of particles produced in the signal process $pp \rightarrow W\gamma + X$ with $W \rightarrow l\nu$, namely the photon, electron/muon, neutrino (via missing energy) and jets.

6.1 Electron and Photon ID

The initial identification of electrons and photons in ATLAS is based on information from the calorimeter and inner detector. The various techniques for both are now outlined with particular emphasis on the photon. The principal reason for focusing on the photon identification is because the main backgrounds fake the signal when a jet is misidentified as a photon (64). As will be shown in chapter 7 the photon P_T distribution is one of the most sensitive to anomalous triple gauge couplings and hence a further reason why measurements of photons are important.

Potential electrons can be identified in the detector using two reconstruction

algorithms depending upon whether they have high or low P_T (65). As this analysis is only interested in electrons with a minimum $P_T > 20$ GeV the high P_T approach is the only way electrons are identified. However, particles identified through the high P_T reconstruction algorithm are not necessarily electrons. The candidate particles are selected using the following procedure:

1. The electromagnetic calorimeter energy deposits are mapped onto an η by ϕ grid with cells of size $\Delta\eta \times \Delta\phi = 0.025 \times 0.025$.

2. A sliding window algorithm of 5x5 cell size moves over the grid and identifies energy clusters.

3. Each cluster is then matched with all track candidates with $P_T > 5$ GeV. The η and ϕ of the cluster must match the η and ϕ of the track to within 0.05×0.1. Should there be a match, the ratio of the energy in the cluster to the track momentum ($E_{cluster}/P_{track}$) has to be less than 4 (ideally this should be 1 for isolated charged particles such as electrons).

4. To minimise the number of jets passing this procedure $E_{cluster}/P_{track} > 0.7$ is also required.

5. Finally the track is extrapolated through each compartment of the calorimeter to ensure the respective cluster η and ϕ position, defined as the centroid of the energy deposit, agrees within 0.025×0.025 to the extrapolated track's η and ϕ.

The identification of photons is almost identical to that of electrons with the exception that photon candidates do not have a track matching the cluster. There is some complexity in identifying a photon because it is observed through its conversion to an electron-positron pair and subsequent showering. If the photon should convert early in the detector then it has to be identified through the signature of an electron and positron originating from a common vertex. This specifically means that the

reconstructed electron and positron trajectories have to be successfully reconstructed back to the photon conversion point using the track information. For the case of the $W\gamma$ signal it is predicted[1] that 37 percent of primary photons will convert before leaving the inner detector ($R < 1150$ mm). A further breakdown of the number of conversions in the subdivisions of the inner detector, as a percentage of the total number of conversions within the inner detector, is given in table 6.1 (figure 6.1 also illustrates this). These will have to be found by the relevant converted photon reconstruction algorithms. The remaining 63 percent of primary photons produced in the $W\gamma$ channel will appear as unconverted photons in the calorimeter.

Sub-detector	Percentage converted
PIXEL	23
SCT	25
TRT	37
SERVICE	15
TOTAL	100

Table 6.1: The percentage of photons converting in the inner detector. The PIXEL, SCT and TRT refer to the various parts of the inner detector as described in chapter 3. The SERVICE label refers to the outer part of the inner detector where the electronics for the inner detector are situated.

Due to the likelihood of other particles, such as those in jets, also passing the reconstruction procedures it has been customary for electron and photon identification algorithms to apply a set of selection criteria based on shower shape, tracking (if an electron) and isolation. Both shower shape and tracking conditions have been combined into a standard technique in ATLAS called "isEM". This isEM condition examines variables from the calorimeters such as hadronic leakage, energy deposits

[1]Using a fully simulated PYTHIA dataset that contains both the actual photons produced by Monte Carlo generation, called the "truth infromation", and a record of the reconstructed photons as predicted by the ATLAS reconstruction algorithms.

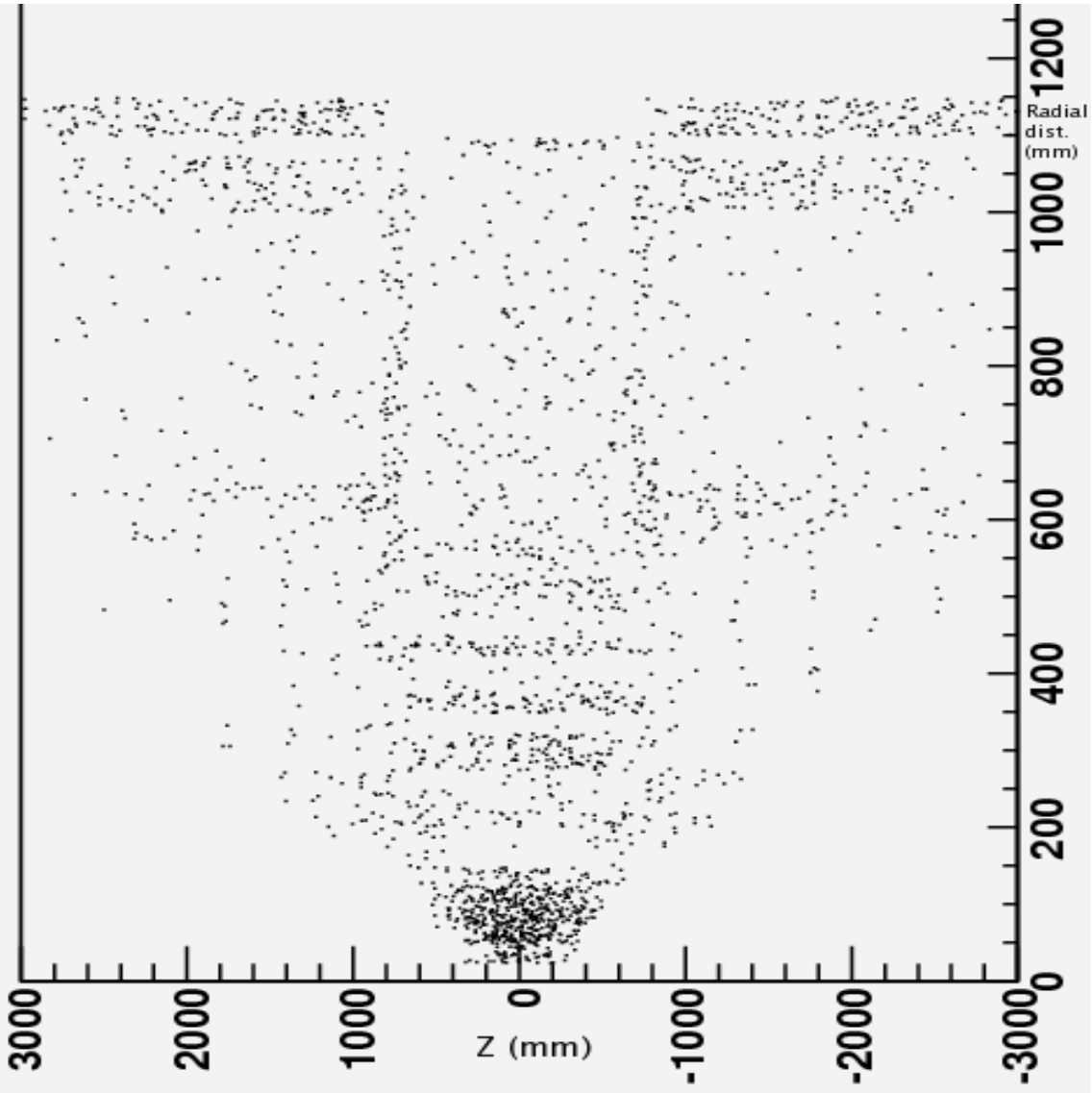

Figure 6.1: Each dot represents the vertex where a photon converts in the inner detector. The beam pipe is on the horizontal axis with 0 representing the interaction point at the centre of ATLAS. The radial distance is on the vertical axis.

in the first and second ECAL compartments and also, for electrons, information from the inner detector such as track quality, spatial matching and TRT information. The various quantities used in the isEM cuts are explained in the following sections, as it is these cuts that remove a large number of the fake photons. As part of the study of triple gauge couplings is very sensitive to the photon distributions,

such as P_T, it is important to model these well. Therefore, for the main variables used in the isEM selection the corresponding contributions representing true and fake photons from the signal and main backgrounds are displayed. This was done to check that the position of the standard isEM cuts, as specified in table 6.2, are sensibly located for identifying true primary photons in the signal. For all cases, any photons considered had to have $P_T > 100$ GeV, as this is the region of interest for this study. A summary of the overall results of applying the isEM cuts is given after their description.

isEM variable	$\|\eta\| \leq 0.8$	$0.8 < \|\eta\| \leq 1.5$	$1.5 < \|\eta\| \leq 1.8$	$1.8 < \|\eta\| \leq 2.0$	$2.0 < \|\eta\| \leq 2.5$
Had. Leakage <	0.03	0.008	0.03	0.02	0.015
$E_{37}/E_{77} >$	0.915	0.91	0.89	0.92	0.91
$\omega_{\eta 2} <$	0.012	0.012	0.012	0.0115	0.0125
$\Delta E(MeV) <$	150	150	350	200	150
$\omega_{tot1} <$	2.7	3.5	3.5	2.0	1.4
$F_{side} <$	0.35	0.6	0.68	0.3	0.2
$\omega_{3strips} <$	0.75	0.75	0.8	0.7	0.6

Table 6.2: Table of isEM conditions for photon identification. The isEM cuts are optimised over a series of η ranges to correspond to the differing performance of the detector.

6.1.1 Using calorimeter information to identify electrons or photons

Hadronic Leakage

A basic requirement for the isEM cuts is that both photons and electrons should deposit little or no energy in the hadronic calorimeter because most of it will have been absorbed in the electromagnetic calorimeter and cryostat wall. Furthermore a study (66) has shown that an electromagnetic shower, originating from electrons,

generally deposits less than 2 percent of its energy in the hadronic calorimeters. A jet however will penetrate into the hadronic calorimeter and deposit a substantial amount of energy there. Therefore by measuring the energy leakage into the hadronic calorimeter from a candidate electron or photon some distinction against jets can be made. The definition of the hadronic leakage is the ratio of the $E_T^{Hadronic}$ (in the first compartment of the hadron calorimeter) to the $E_T^{Electromagnetic}$.

The hadronic leakage is shown in figure 6.2 and further explanation of what is displayed follows. In this figure, and the subsequent isEM related ones, several distributions are plotted. To understand what has been plotted it is important to make a distinction between reconstructed photons (i.e. the particles that have passed the ATLAS photon reconstruction algorithms) and the Monte Carlo truth photons (i.e. the photons that were produced by the Monte Carlo generator at the event generation and detector simulation stage.). For each of the distributions labelled "Matched" a primary photon from the Monte Carlo truth has been found to be within a distance $\Delta R = \sqrt{\Delta\eta^2 + \Delta\phi^2} < 0.4$ of the reconstructed photon candidate. The reconstructed photons in these cases are therefore most likely to be correctly reconstructed high energy photons. The "Background Not Matched" and "Signal Not Matched" cases correspond to reconstructed candidate photons that do not have a true photon within $\Delta R < 0.4$. These are very likely to be fake photons and originate from jets or even misidentified electrons/muons. Any photons that are not matched are not useful when trying to identify primary photons. By using these distributions and examining where the isEM cut is (the vertical solid line on the plot) it can be determined whether the cut is in the right place. Ideally a correctly set isEM cut would remove the "not matched" photon candidates (i.e. jets faking photons) and leave the matched photons (i.e. real primary photons). The overall effectiveness and comments on the suitability of this and the following isEM cuts are given in section 6.1.3.

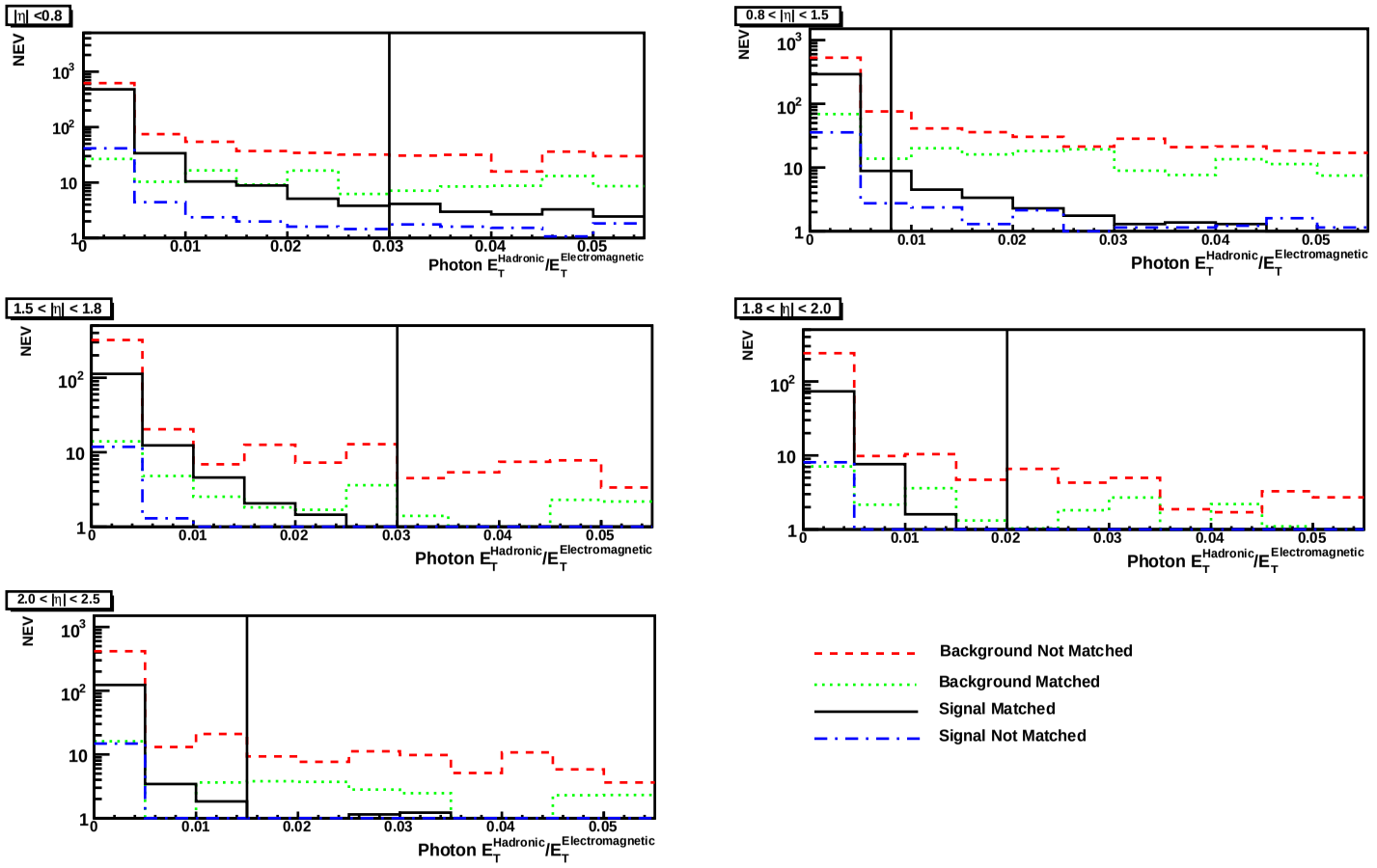

Figure 6.2: The hadronic leakage. In all plots the signal and backgrounds are normalised to a luminosity of 0.5 fb^{-1}. See text for details. On the y-axis is the Number of Events (NEV).

Measuring the transverse shower profile using energy deposits in the second compartment of the ECAL

The second compartment of the electromagnetic calorimeter is the largest one and hence the majority of the energy from electromagnetic showers is deposited in this layer. Particles such as photons or electrons will give a narrow shower profile compared to jets that are typically composed of many particles. In addition to this jets deposit only a small percentage of their energy in the electromagnetic calorimeter. Therefore, by examining the lateral shower shape and the lateral width of particles in this sampling layer a further distinction between electromagnetic electrons/photons and hadronic jets can be made.

It has been shown (64) that electrons and photons deposit most of their energy in a $\Delta\eta \times \Delta\phi$ = 3x7 window of calorimeter cells (each calorimeter cell dimension is 0.025×0.025 in $\Delta\eta \times \Delta\phi$). By comparing the ratio of energy in a 3x7 to a 7x7 window a value for the transverse energy leakage can be obtained. This energy leakage is an indirect measurement of the lateral shower shape. For the case of electrons and photons the leakage should be small and the ratio is expected to peak towards 1 whereas jets will typically have a large tail to lower values (figure 6.3).

The lateral shower width can also be calculated by examining the energy weighted sum in a 3×5 window of calorimeter cells:

$$\omega_{\eta 2} = \sqrt{\frac{\Sigma E_c \times \eta^2}{\Sigma E_c} - \left(\frac{\Sigma E_c \times \eta}{\Sigma E_c}\right)^2}. \tag{6.1}$$

To summarise equation 6.1, it allows discrimination between particles whose deposited transverse energy in a 3×5 window of calorimeter cells (E_c) is far away from the shower core to those that are central, by weighting those that are further away in η as shown in figure 6.4.

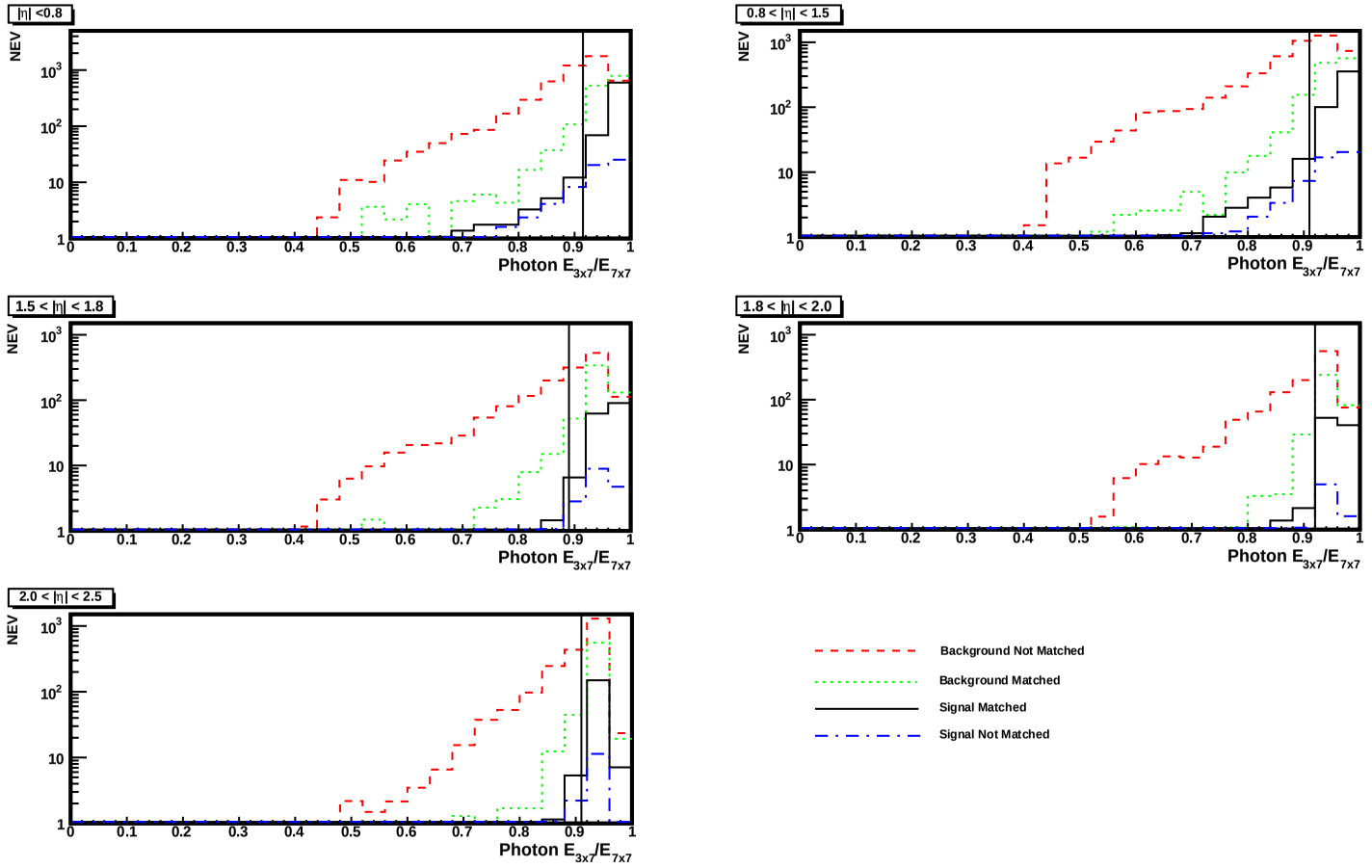

Figure 6.3: Ratio of energy in 3x7 over 7x7 calorimeter cell for photons. In all plots the signal and backgrounds are normalised to a luminosity of 0.5 fb^{-1}.

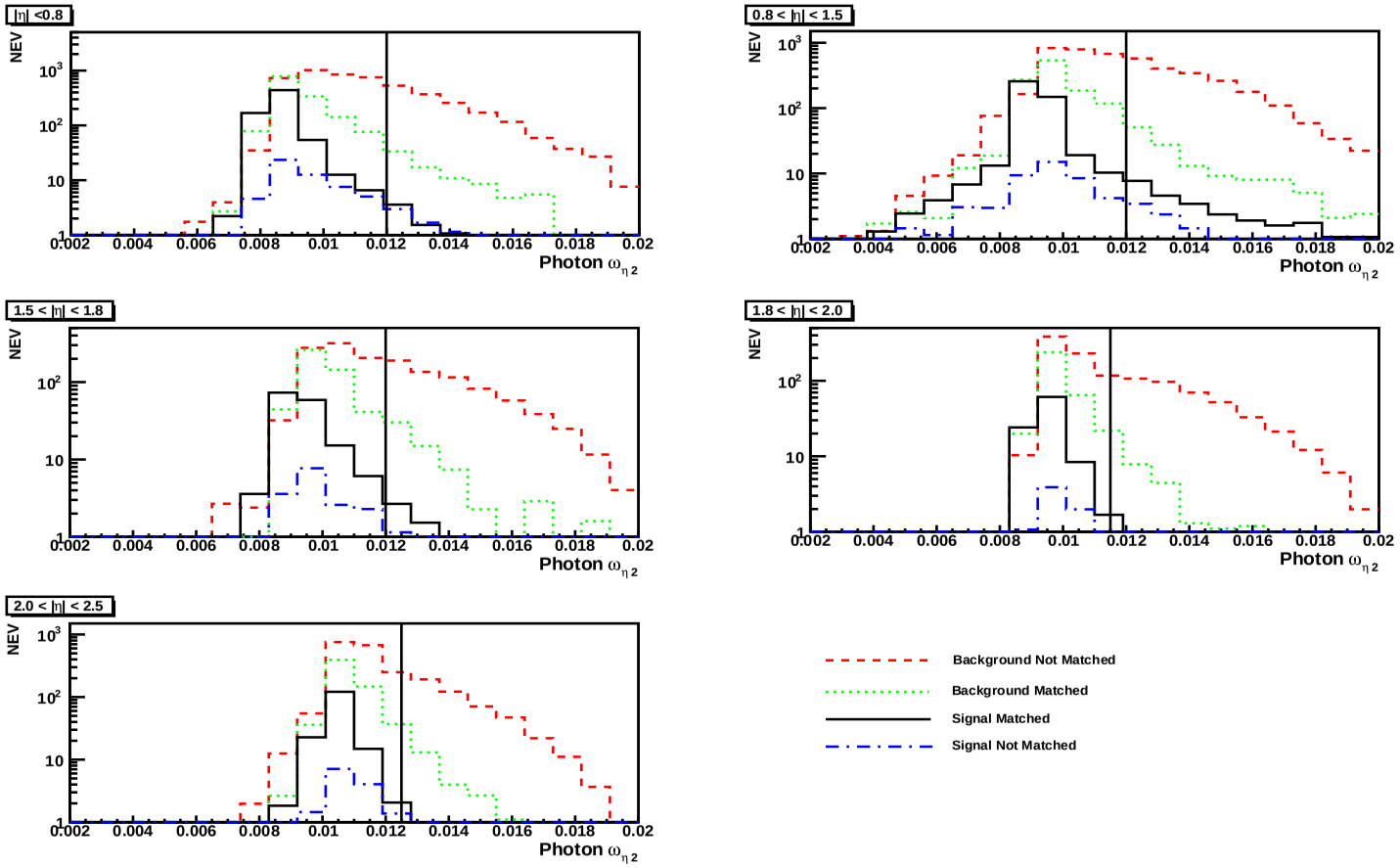

Figure 6.4: Lateral shower width for photons. In all plots the signal and backgrounds are normalised to a luminosity of 0.5 fb^{-1}.

Use of the first compartment of the ECAL

The transverse shape cuts on the cluster in the second compartment of the ECAL are used to veto jets that have wide showers. The types of jets that can pass the second electromagnetic compartment cuts are typically composed of single η and π^0 particles (64; 67). The first compartment of the electromagnetic calorimeter is of use in removing these narrow jets because it has a high granularity that allows substructures in the shower to be observed. Different substructures for the π^0 and γ are to be expected because the photon converts to an e^+e^- pair while the π^0 decays to two photons. For a high E_T π^0 the two photons will be close together in the calorimeter. A further statistical observation (64), via the energy deposition in the first sampling layer, indicates that the probability of two photons from a π^0 decay interacting early in the first sampling layer is greater than that of a single primary photon. One of the isEM conditions for this part of the detector is that particles with less than 0.5% of their transverse energy deposited in the first sampling layer are assumed to be photons and hence no further cuts based on this compartment are applied. If the transverse energy in this compartment is larger than 0.5% then further cuts are made only if the particle is found within $|\eta| < 2.35$, as this is where the strip granularity is fine enough to observe the substructure.

If a candidate passes the previous cuts, as defined above, then several more cuts are applied that exploit the substructure of the shower. The first of these cuts examines a window of size $\Delta\eta \times \Delta\phi$ =0.125 $\times$ 0.2 to see whether more than one energy maximum exists. The purpose of this is that the π^0 will have decayed to two photons that should give two energy maxima if both photons have converted. By searching in the 0.125×0.2 window, centred around the hottest cell, a second energy maximum E_{max2} could be found. By combining this with the minimum energy E_{min} between the first and second energy maxima the difference $\Delta E = E_{max2} - E_{min}$ can be defined. ΔE can then be used because single photons should have only one well resolved maximum and hence an undefined or small ΔE, whereas a π^0 with two

energy peaks from two photons should have a large ΔE as shown in figure 6.5.

As in the case of the second electromagnetic compartment, the shower width and shape can also be used. In particular, the isEM cut makes use of the total shower width to try to remove any wide showers that remain with one maximum (figure 6.6). The total shower width ω_{tot1} is calculated using the energy in i^{th} strip E_i in a window of $\Delta\eta \times \Delta\phi$ =0.0625 $\times$ 0.2. This window usually contains 40 strips and in the following equation for the total shower width the 'i' represents the strip number and i_{max} the strip number with the first local maximum:

$$\omega_{tot1} = \sqrt{\Sigma[E_i \times (i - i_{max})^2]/\Sigma E_i}. \tag{6.2}$$

Two more variables that study the fine structure of the remaining narrow showers are used. The shower shape in the core can be examined by the use of the F_{side} variable:

$$F_{side} = \frac{E(\pm 7) - E(\pm 3)}{E(\pm 3)}. \tag{6.3}$$

In equation 6.3 the $E(\pm n)$ represents the energy in the $\pm n^{th}$ strip centred on the highest energy strip. F_{side} thus gives an indication of how centralised the core is (figure 6.7).

The last variable used is another definition of the shower width that just uses three strips centred on the strip with the highest energy deposit (figure 6.8). The variable $\omega_{3strips}$ is defined as in equation 6.2 except that 'i' runs over just three strips.

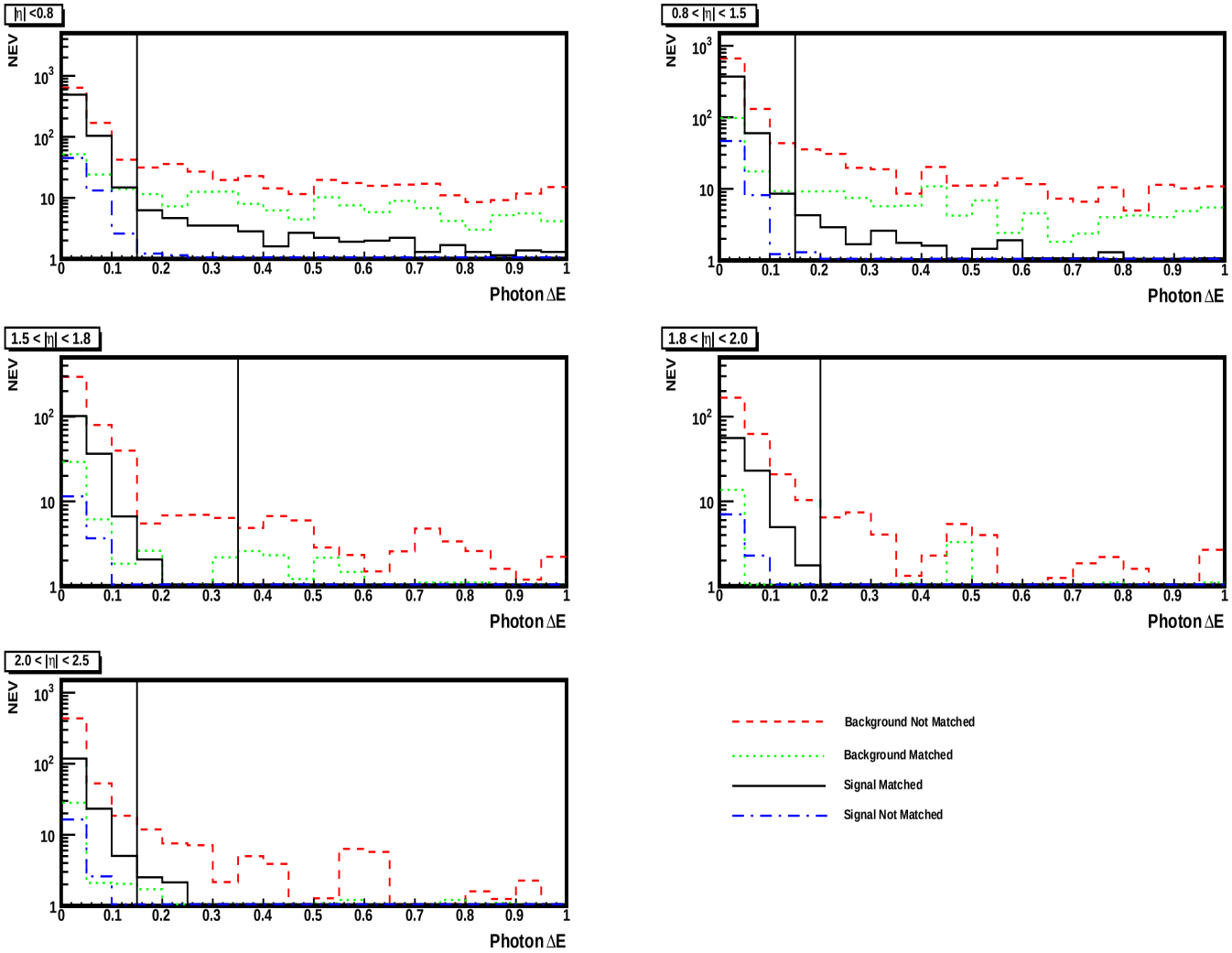

Figure 6.5: The ΔE for photons. In all plots the signal and backgrounds are normalised to a luminosity of 0.5 fb^{-1}.

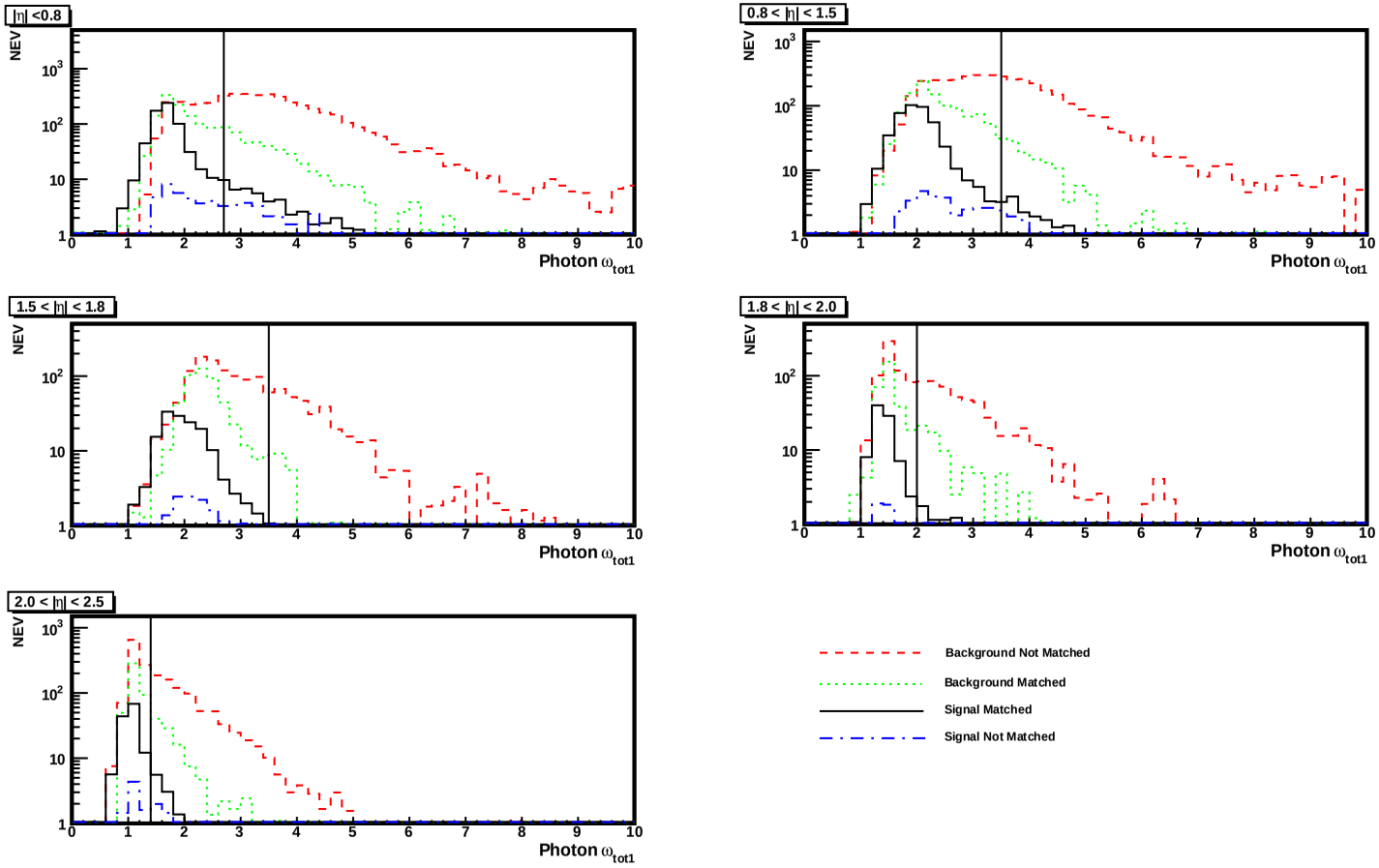

Figure 6.6: Total shower width for photons. In all plots the signal and backgrounds are normalised to a luminosity of 0.5 fb^{-1}.

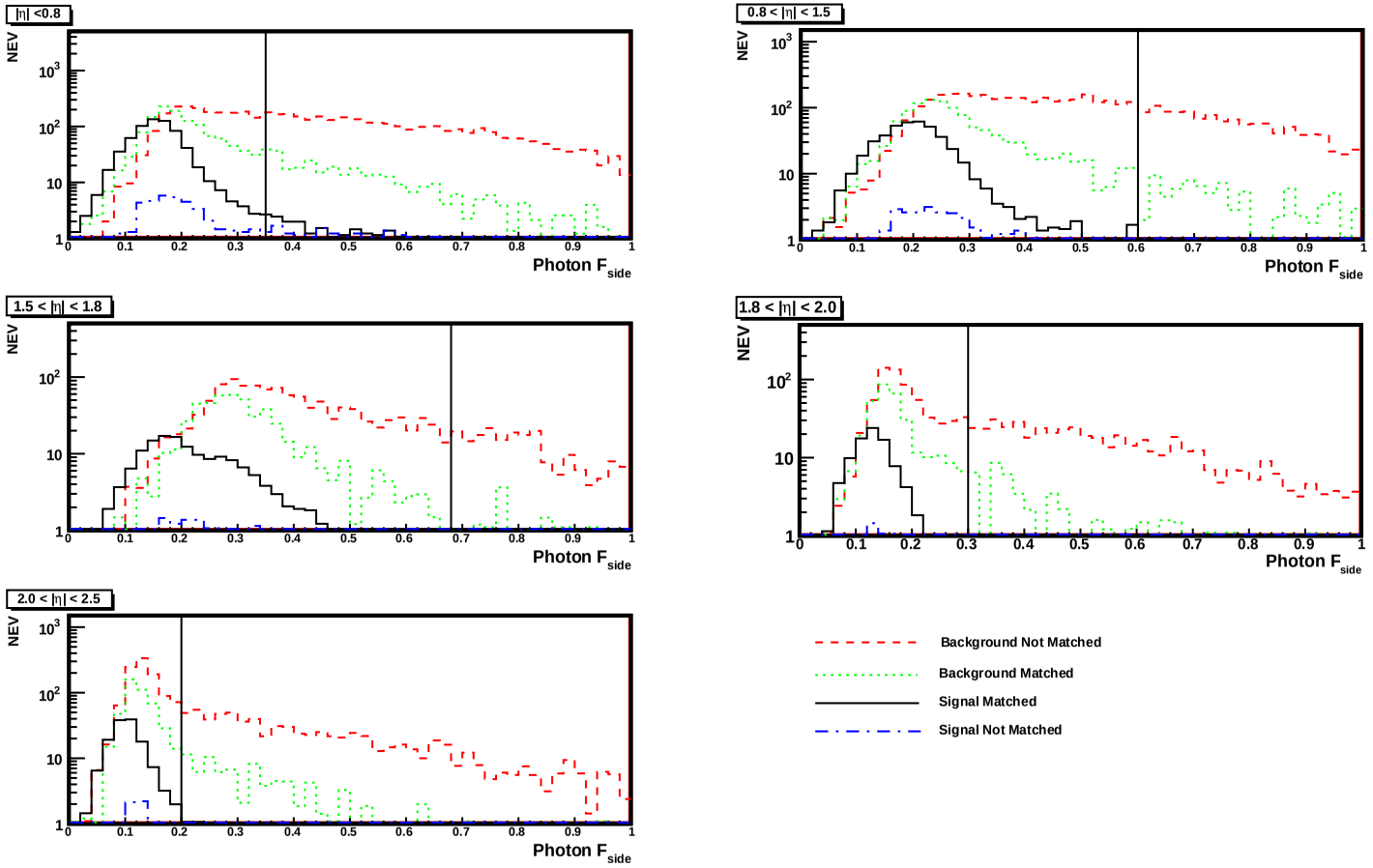

Figure 6.7: Shower shape in the core for photons. In all plots the signal and backgrounds are normalised to a luminosity of 0.5 fb^{-1}.

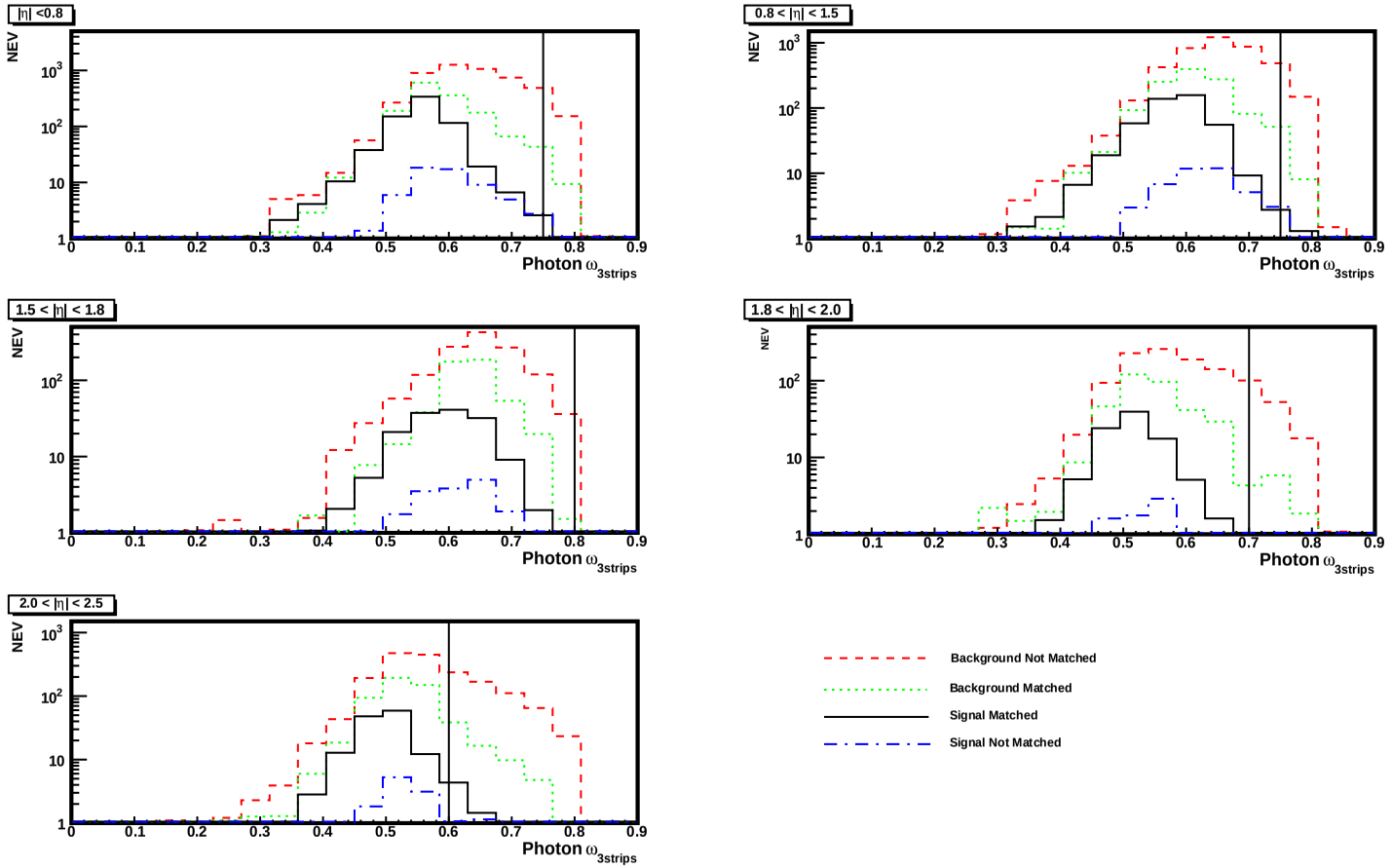

Figure 6.8: Shower width in three strips for photons. In all plots the signal and backgrounds are normalised to a luminosity of 0.5 fb^{-1}.

6.1.2 Using tracking information to identify electrons

The inner detector can be used to further improve the identification of electrons by applying track quality cuts, spatial matching and information from the TRT. When these cuts are applied after the calorimeter based cuts they are useful for removing the remaining photon conversions and high P_T π^0 mesons in low multiplicity jets.

The first tracking requirement is that the track must have at least nine hits in the pixel and SCT layers. Two of these hits must be in the pixel layer with one of those in the first pixel layer. Further jet rejection can then be obtained by comparing the information from the tracker and calorimeter. This can be done by requiring a good pseudorapidity match between the track position in the first compartment of the calorimeter ($\eta_{strips\ cluster}$), where the granularity is best, to the pseudorapidity of the track extrapolated from the inner detector (η_{ID}):

$$|\Delta\eta| = |\eta_{strips\ cluster} - \eta_{ID}|. \tag{6.4}$$

The azimuthal angle is checked using the second compartment of the ECAL and the track is extrapolated to that position from the inner detector:

$$|\Delta\phi| = |\phi_{Second\ ECAL} - \phi_{ID}|. \tag{6.5}$$

The TRT information can also be used by examining the ratio of high threshold TRT hits[2] N_{TR} to the total number of TRT hits N_{straw} (69). This removes charged hadrons that only have a low percentage of tracks with high threshold hits.

By using the information from the calorimeter and inner detector the electron identification reconstruction efficiency was studied. By matching the number of true

[2]A high threshold hit is one where the TRT straw (see section 3.3.3) has a hit occupancy of 5 keV relative to a low threshold hit occupancy of 200 eV (68).

electrons to reconstructed electrons on an event-by-event basis the reconstruction efficiency was found (table 6.3). This gives a jet rejection of approximately 5×10^5.

	Wγ signal sample
Number of Events	38350
Number of True Electrons	19074
Number of Reco Electrons	15069
Efficiency	0.79
Efficiency with all isEM cuts applied together	0.61

Table 6.3: The reconstruction efficiency for electron identification on signal events. See table 6.2 for the values of the isEM cuts used. No single isEM cut dominated the overall isEM reconstruction efficiency. The true electrons were defined to be in the acceptance of the detector ($|\eta| < 2.5$) and with a transverse momentum $P_T > 20$ GeV. The reconstructed electrons also had to be in acceptance with a transverse momentum $P_T > 20$ GeV.

6.1.3 Summary of the effectiveness of photon identification using isEM

The cut values used for the isEM condition are displayed in table 6.2. By matching the number of true photons to reconstructed photons on an event-by-event basis the reconstruction efficiency can be studied for the signal process (table 6.4). When only events with a photon with $P_T^\gamma > 100$ GeV are considered these cuts remove approximately 36 percent of the matched signal photons (i.e. the photons that are most likely to be true primary photons). However, the number of fake photons originating from the background is reduced by 93 percent. The relatively small number of fake photons in the signal is reduced by 96 percent. The selection is therefore a balance between efficiency and purity. The various isEM distributions suggest that these cuts could be further optimised for this specific study. For consistency

with other work, the standard ATLAS isEM cuts were used as the performance was sufficient.

	Wγ signal sample
Number of Events	38350
Number of True Photons	28847
Number of Reco Photons	23334
Efficiency	0.81
Efficiency with all isEM cuts applied together	0.64

Table 6.4: The reconstruction efficiency for photon identification on signal events. See table 6.2 for the values of the isEM cuts used. No single isEM cut dominated the overall isEM reconstruction efficiency. The true photons were defined to be in the acceptance of the detector ($|\eta| < 2.5$) and with a transverse momentum $P_T > 100$ GeV. The reconstructed photons also had to be in acceptance with a transverse momentum $P_T > 100$ GeV.

6.2 Muon ID

Muons are easier to identify than electrons in ATLAS and give a much cleaner signal due to the electromagnetic and hadronic calorimeter removing most of the problematic hadronic background. Several different packages have been developed to try to reconstruct muons efficiently. In the case of the $W\gamma$ channel where the W decays to a muon it is important to see how well each of these reconstruction packages performs. Two of the relevant muon reconstruction packages are now briefly reviewed in order to make such a comparison on muon performance.

6.2.1 Muonboy and STACO reconstruction package

The Muonboy package (70) performs a detailed reconstruction of tracks in the muon spectrometer and takes into account multiple scattering, dead material and energy loss from the calorimeters. The tracks from the inner detector and those found in Muonboy can be merged using the Statistical Combination (STACO) package (70; 71) to obtain a global track and improved momentum resolution at low to moderate P_T.

6.2.2 Moore and MuID reconstruction package

The Moore reconstruction package (72; 73; 74) is capable of fitting tracks by recognising patterns in the MDT and CSC components of the muon spectrometer. In a similar fashion to Muonboy, the Moore package can be combined with the MuID package (75) to obtain a global track. The MuID package is also capable of taking into account multiple scattering and energy loss from the calorimeters.

6.2.3 Comparing STACO and MuID

In order to determine which algorithm is better for identifying muons in this study a comparison of Muonboy plus STACO combined against Moore plus MuID combined was made for the $W\gamma$ channel. This was done using the MuPerf analysis package (76) that matches the true and reconstructed muons on an event-by-event basis. MuPerf allows the different algorithms to be compared by examining the reconstruction efficiency as a function of muon P_T, η and ϕ. These were then examined using the $W\gamma$ channel in the fully simulated SHERPA sample. For the case of the efficiency as a function of P_T, the combined STACO package is slightly better at the low to moderate $P_T < 200$ GeV range. In the P_T range above this, low statistics make it hard to draw conclusions from any differences. The muon η and ϕ efficiency

distributions were found to contain only negligible differences. A summary of the results are presented in table 6.5 which gives the efficiency and the number of fake muons per event. Due to the slightly better performance of the STACO package at low P_T, this is the reconstruction package that is used in this study to identify muons.

	Staco combined	Muid combined
Number of Events	38350	38350
Number of True Muons	19786	19786
Number of Reco Muons	18480	18104
Efficiency	0.934	0.915
Efficiency with muon $P_T > 20$ GeV	0.830	0.813

Table 6.5: Comparison of the STACO and MuID combined packages. A fully simulated dataset of $W\gamma$ events was used with the W allowed to decay to $e^{\pm}$ or $\mu^{\pm}$. MuPerf compares true muons (defined as being any muon within the acceptance with $P_T > 2$ GeV) to reconstructed muons. The efficiency for the matching of these true and reconstructed muons is labelled "Efficiency" in the table. A further efficiency is also reported for muons with $P_T > 20$ GeV.

6.3 Missing E_T

Measuring the missing energy is important for the signal as the presence of the neutrino from the W boson decay can be inferred from this. For this study the reconstructed missing energy, $E_T^{MISS}(reco)$, was calculated from the energy deposited in the calorimeter (with a correction applied for energy lost in the cryostat) and from the momentum measurements of muons. For the purposes of this study this was already implemented via the centrally produced ATLAS software as described by MET_Final (77; 78).

6.4 Jet reconstruction

ATLAS is an environment in which jets are in abundance due to the hadronic proton proton collisions. As the $W\gamma$ signal may be produced in association with jets it is important to ensure that the best reconstruction is used, in particular so that any high jet multiplicity backgrounds (especially $t\bar{t}$) can effectively be vetoed. The rest of this section details the various methods of reconstructing jets and the motivation for the choice of method.

The aim of a jet reconstruction algorithm is to match the jet with the original parton from the hard scattering. However, jets are complicated to reconstruct because they are caused by the hadronisation and showering of quarks and gluons. This is further complicated by detector effects such as dead material, the magnetic field and electronic noise. When measuring a jet the reconstruction can be split into two sections. The first is the reconstruction of the jet using a clustering algorithm on the energy deposits in the calorimeter. The second is the energy calibration of the jet to take into account detector effects. In this study the second step is processed automatically by the ATLAS software. As it is not possible to repeat the jet finding on the AOD data file, in this analysis there were only two predetermined types of clustering algorithm that could be used. These were the cone algorithm and the Kt algorithm (77). The cone algorithm operates by taking an initial energy deposit in the calorimeter and then clusters it with other nearby energy deposits in increasing angle, up to a fixed cone size ΔR. The cone algorithm keeps iterating over the cone until it obtains a stable E_T weighted cone. The Kt algorithm is different from the cone algorithm in that it merges pairs of energy deposits in increasing transverse momentum until a specified cut off. The implementation of both algorithms have advantages and disadvantages and a description of both, with particular emphasis on hadron colliders, can be found in reference (79). For this analysis no distinguishing feature between the jet algorithms could be found that identified either as being the better reconstruction technique to use. The ATLAS-specified cone algorithm

with size 0.4 radius was therefore used.

6.4.1 Reconstructed jets - The removal of non-jet particles from the jet container

One feature of how the ATLAS reconstruction stage works is that particles of certain types are grouped into containers. For instance there exists a photon container that stores for each event the number of photons that have passed the basic photon reconstruction. The particles that are placed into their respective containers are only loosely identified though, hence the need for additional photon identification cuts on photon candidates in the photon container. In the jet container, the jets are very loosely defined (the majority of particles that leave a shower in the calorimeter will be entered into this container). This means that photons, electrons or muons for the case of the $W\gamma$ signal can also end up in the jet container. If these particles are not removed the events will be mis-reconstructed. The procedure for removing them in this analysis is first to identify cleanly the e, μ and γ particles that could enter the jet container. Specifically this means finding a photon or electron that passes the isEM style calorimeter cuts or a clean muon. Once these particles have been identified they are matched in ΔR space to any jet. The separation of the lepton or photon from the jet ($\Delta R_{l,jet}$ and $\Delta R_{\gamma,jet}$) were observed to be correlated for distances $\Delta R_{l,jet} < 0.1$ and $\Delta R_{\gamma,jet} < 0.1$. This indicated that the jet was travelling in a direction collinear to the respective particle and was thus highly likely to be a replica. The distance $\Delta R < 0.1$ is therefore chosen as the cut off point below which any matched jet is removed and not used.

Chapter 7

Sensitivity to anomalous couplings with 0.5 fb^{-1}

This chapter derives the sensitivity to triple gauge couplings at low luminosity in ATLAS. After examining the appropriate preselection cuts the method for estimating the sensitivity is detailed, followed by the differing ways that the predictions can be made. Finally a study of the systematics is incorporated.

7.1 Preselection Cuts based on Event Generation, Particle ID and Signal Description

The main motivation for applying preselection cuts is to ensure that any unmodelled backgrounds are removed from consideration and that the signal region of interest is selected. Later in this chapter other selection cuts will be investigated that optimise the sensitivity to triple gauge couplings, hence these cuts are called preselection cuts. As the signal and background samples have been generated with different generator-level cuts it is also a necessity that cuts are applied to ensure the fully populated

regions are examined. Other preselection cuts are determined by the distinguishing features of the signal and the aim of sensitivity to anomalous couplings. A summary of all the preselection cuts applied is given here with the relevant explanations following.

1. Exactly one good photon with $P_T > 100$ GeV is found.
2. No other loose photon with $P_T > 100$ GeV is found.
3. Exactly one muon or good electron with $P_T > 20$ GeV is found.
4. The above lepton must give a real solution for the neutrino longitudinal momentum (using the E_T^{miss} in the event). See section 7.3 for details of the calculation.
5. No other muon or loose electron with $P_T > 20$ GeV is found.
6. $\Delta R_{l,\gamma} > 0.4$.
7. $E_T^{miss} > 15$ GeV.
8. $|\Sigma \overrightarrow{P_T^{Jet}}| < 200$ GeV.

A good photon or electron corresponds to one that has passed the isEM conditions in section 6.1, whereas a loose photon or electron does not pass the isEM conditions. In this study the identification of any photons or electrons is performed within the pseudorapidity range of $|\eta| < 2.5$. For muons the corresponding value is $|\eta| < 2.7$.

To explain the choice of the preselection cuts requires examining the basic experimental signatures of the $W\gamma$ signal. The $W\gamma$ signal was generated using SHERPA in such a way that it is characterised by a high-P_T photon and a W decaying leptonically into either electron or muon flavours. The photon and electron/muon were also generated in the range $|\eta| < 2.7$. The processes that SHERPA generated at

matrix element level were up to the first order in α_S and second order in α_{EM}. These signal generation criteria indicate that the number of high-P_T photons in the event should be restricted to one and the number of high-P_T $e^{\pm}$ or $\mu^{\pm}$ in the event to one. The restriction of just one electron or muon is a good veto against events containing Z bosons. In both cases the correct primary photon or lepton should be identified accurately as this is what any measurement will be based on. However, when searching for the presence of other photons or leptons, in order to veto the event, it is far more stringent to relax the identification criteria on secondary particles so as not to include the isEM conditions (i.e. a loose photon/electron). This ensures a greater purity in the event selection and increases the probability of the correct photon or lepton being selected. This can be particularly useful in events such as $Z \rightarrow ee$ decays or $t\bar{t}$ where the chance of having two leptons that are not both cleanly identified is reasonable. The relaxation on the identification of secondary particles, after the other preselection cuts have been applied, reduces the signal efficiency by a further 3 percent compared to a further 19 percent reduction in the background.

Another preselection cut applied is to ensure that any electron or muon identified can be reconstructed to give a real solution for the neutrino longitudinal momentum. This is done in order to reconstruct the $M_{W\gamma}$ system and a full explanation of how this is performed is given in section 7.3. However, a real solution does not always exist due to detector effects or misidentification so in these cases the events were not selected.

It is also important to try to identify any photons that have been produced due to final state radiation (FSR) off a lepton. These photons contain no information on the triple gauge coupling so should be suppressed where possible. In addition FSR can cause confusion in selecting a photon because it was observed in the $W\gamma$ data sample used in this study to be a leading cause of events[1] containing two

[1]Three percent of the total number of events produced.

photons that pass the particle identification criteria. By using the fact that photons produced via FSR are preferentially emitted along the direction of the radiating particle it is possible to place a cut on the separation between the photon and lepton $\Delta R_{l,\gamma} = \sqrt{(\eta_l - \eta_\gamma)^2 + (\phi_l - \phi_\gamma)^2}$ distribution, where l represents an electron or muon and γ the photon. This cut was placed at $\Delta R_{l,\gamma} > 0.4$. When $\Delta R_{l,\gamma}$ is required to be > 0.4 the sensitivity to triple gauge couplings is not diminished. Any photon that is found to lie within this cut is removed from consideration as a potential candidate, should no photons be left then the event is vetoed. Should two photons, with minimum $P_T > 100$ GeV, still be found in the event after this cut then one photon is either a hard photon from the lepton or a fake photon. As it is impossible to tell which photon is of interest, for simplicity, the event is vetoed.

Further selection to require events to look like the signal can also be made by placing a cut on E_T^{miss}. This is designed to account for the neutrino and thus is a veto against backgrounds that should have little or no E_T^{miss} such as $Z\gamma$. It is set relatively low at 15 GeV so that it can be increased later if necessary.

In addition to the above cuts a jet veto was also investigated because it can be effective in removing the NLO contribution to the $W\gamma$ channel that has no sensitivity to the anomalous couplings. However, it should also be remembered that some of the NLO contribution to the $W\gamma$ channel does contain a triple gauge coupling. The application and usability of a jet veto might, therefore, be considered when discussing the analysis of triple gauge couplings. However, for the reasons to be outlined it is discussed here. A jet veto is also important for removing backgrounds that can contain high momentum jets, for example $t\bar{t}$. In this study as the backgrounds had lower statistics, in the region of interest, than the signal it was found to be advantageous to reduce their contribution significantly through this cut. In addition, for the case of the $W\gamma$ event generation, it had been observed that a small percentage of events had been produced where a photon radiated off a lepton and a jet was also present. This could be viewed as W+jets production and meant a small fraction of

events were being double counted with the W+jets sample. Although the majority of these events were removed by the previous $\Delta R_{l,\gamma} > 0.4$ cut it was found, by examining the Monte Carlo truth information, that this contribution could be made negligible by the stringent jet veto that was chosen. The vector sum of jet P_T ($|\Sigma\overrightarrow{P_T^{Jet}}|$) was used as a veto. As a mixture of LO and NLO generators are used this is a more appropriate cut than acting on just one jet in an event. The best signal to background ratio was observed to require a $|\Sigma\overrightarrow{P_T^{Jet}}| < 100$ GeV. However, using the log-likelihood fitting method as described in section 7.2, the best sensitivity to anomalous couplings was found to be at $|\Sigma\overrightarrow{P_T^{Jet}}| < 200$ GeV.

A summary of the above cuts with the number of events found in the signal and background at an integrated luminosity of 0.5 fb^{-1} is displayed in table 7.1. The signal efficiency after the last of the preselection cuts is 13 percent while the background efficiency is 1 percent.

Preselection Cut	$W\gamma$	$t\bar{t}$	W+Jet	Z+Jet	$Z\gamma$	S/B
Photon ID+Lepton ID	385	24	73	33	10	2.8
$\Delta R_{l,\gamma} > 0.4$	310	22	59	33	10	2.5
$E_T^{miss} > 15$ GeV	290	21	51	22	5	2.9
$\lvert\Sigma\overrightarrow{P_T^{Jet}}\rvert < 200$ GeV	229	17	38	16	5	3.0

Table 7.1: Preselection cuts for the signal and backgrounds for a luminosity of 0.5 fb^{-1}. The numbers shown for each process are the number of events that pass the given preselection cuts. When moving down the table the previous preselection cuts are included. The photon ID corresponds to all the photon related cuts in the preselection list given earlier (numbers 1-2). The lepton ID corresponds to all the lepton related cuts (numbers 3-5).

7.2 Measuring the sensitivity to anomalous TGC via a binned log-likelihood fit

In order to find the sensitivity to anomalous couplings for a given set of data a binned log-likelihood fit (80) was used. The log-likelihood fitting procedure works by using a set of predictions so that an unknown parameter can be determined. In this case it is possible to construct several reference or template histograms, for instance the photon P_T, with a known value of an anomalous coupling. The histograms used in the fit contain both the signal and background contributions that remain after the cuts (see the black solid line of figure 7.10). These histograms are the predictions that are then used to determine the unknown anomalous coupling parameters from a data sample. More rigorously, the likelihood function can be described as the product of probability density functions $P(x_n;\theta)$ where x_i is the observable for event i and θ is the parameter to be estimated. For the case of the photon transverse momentum (P_T^γ) the likelihood would be:

$$L(\Delta\kappa_\gamma,\lambda_\gamma) = \Pi_{i=1}^{n} P(P_{T,i}^\gamma;\Delta\kappa_\gamma,\lambda_\gamma) \tag{7.1}$$

where the product is taken over all selected events n.

The maximum of this likelihood function is the best estimate of an anomalous coupling for the specific dataset. The maximum is found by taking the first derivative of the likelihood with respect to the coupling and equating it to zero. For computational reasons the log of the likelihood is taken first. For the general case the best estimate, providing it exists, would satisfy:

$$\frac{\partial lnL}{\partial\Delta\kappa_\gamma\partial\lambda_\gamma} = 0. \tag{7.2}$$

As the fit was binned the form of the likelihood function used was altered to take into account the number of bins (N_{Bins}) and the number of data events in the j^{th} bin (NEV_j):

$$L = \Pi_{j=1}^{N_{Bins}} [P(P_{T,j}^\gamma;\Delta\kappa_\gamma,\lambda_\gamma)]^{NEV_j}. \tag{7.3}$$

The above procedure for calculating the log-likelihood function and finding the best fit value was performed using the MINUIT package (81). MINUIT also extracted the corresponding confidence limits at the 68.27 % (corresponding to one standard deviation) and 95 % level by finding where the contour, defined by a distance of 0.5 or 1.92 up from the best fit value, intersected the log-likelihood function.

In this study the method of constructing the probability density function $P(x_n;\theta)$ for the likelihood function is based on the parabolic dependence of the cross section on the anomalous couplings (see section 2.4.1). The various steps showing how it is used are outlined below:

1. Create binned and normalised (to the cross section) template histograms in the SM limit and with anomalous couplings active. Fully simulated datasets in the SM limit and with $\Delta\kappa_\gamma = 0.5$, $\Delta\kappa_\gamma = 1$, $\lambda_\gamma = 1$, $\lambda_\gamma = -1$ and $\lambda_\gamma = 1$ plus $\Delta\kappa_\gamma = 1$ are used for this. Both signal and background contributions combined are used for this.

2. For each reference histogram find the cross sections in each bin for each value of the anomalous coupling. The cross section for datasets with differing anomalous coupling should vary parabolically with the coupling.

3. Construct the parabola defined by the points above for each bin (if both $\Delta\kappa_\gamma$ and λ_γ are varying it is a paraboloid). When normalised (using all the parabolas) this represents the probability density function. For the case of either $\Delta\kappa_\gamma$ or λ_γ varying this requires just three points to define the parabola (e.g. if measuring the likelihood for just $\Delta\kappa_\gamma$ use the cross section values in each bin from the SM limit, $\Delta\kappa_\gamma = 0.5$ and $\Delta\kappa_\gamma = 1$ template samples to get three points). When allowing both $\Delta\kappa_\gamma$ and λ_γ to vary together six points are required.

In this study both $\Delta\kappa_\gamma$ and λ_γ anomalous couplings were allowed to vary. However, for the purposes of studying the sensitivity to them, $\Delta\kappa_\gamma$ was first examined

with λ_γ fixed to its SM value and vice versa. Finally the sensitivity with both $\Delta\kappa_\gamma$ and λ_γ varying together was studied. Normally, when making this measurement, data from the experiment would be used in the log-likelihood fit. However, as this could not be done 'data-like' samples, with the numbers of events corresponding to a luminosity of 0.5 fb^{-1}, were used. These 'data-like' samples used different events from the template samples.

In order to verify that the likelihood fit was indeed working, 'data-like' samples with anomalous couplings active were passed into the fitting algorithm. This was done in order to show that the fit was unbiased and that it would reproduce the associated dataset's coupling. In all cases tested the prediction reproduced the anomalous coupling's value at the 95% confidence level (see figure 7.1).

The statistical reliability of the fitting procedure was investigated by producing 'pull tests' using 50 SM 'data-like' samples. When each 'data-like' SM sample is fitted the most likely value is returned, that in the ideal case would be the SM value. It is important to check the statistical reliability of the fit by examining the 'pull' away from the SM value that each 'data-like' sample gives:

$$pull = \frac{\Delta S}{\sigma} \tag{7.4}$$

where ΔS is the most likely value returned by the fit minus the true SM value (i.e. the shift), and σ is the 1 standard deviation statistical error given by the fit (see figure 7.2). As the 1 standard deviation statistical error can sometimes be slightly asymmetrical, the average of the positive and negative value was used to represent σ in each fit. For the case of $\Delta\kappa_\gamma$ the pull distribution was found to have an RMS of 0.81±0.08 with a mean of 0.08±0.11 and for λ_γ an RMS of 0.51±0.05 with a mean of 0.04±0.07 (see figure 7.3). Ideally the standard deviation would be expected to be around 1, as the shift away from the true SM value for each dataset should lie within 1σ 68% of the time. The results obtained here, for the $\Delta\kappa_\gamma$ and λ_γ anomalous couplings, indicate that for 68% of the 'data-like' samples the shift from the SM value lies within the 1σ statistical error. The errors produced by the fit are

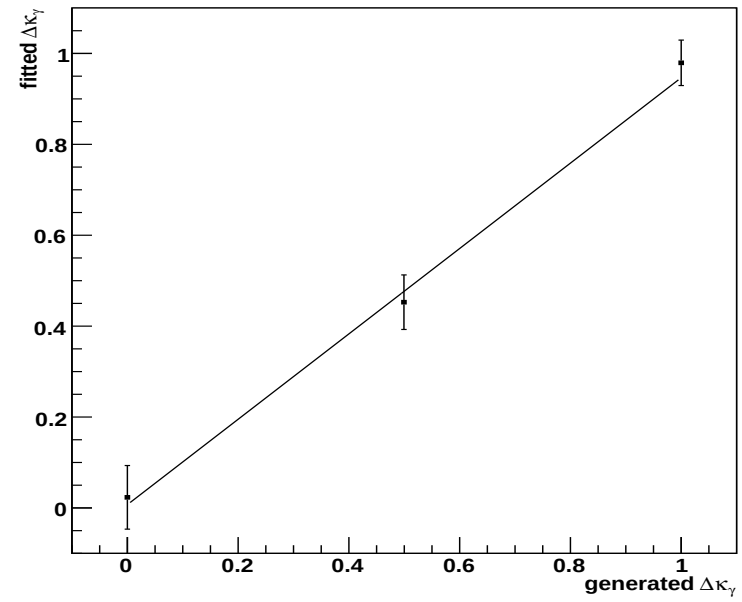

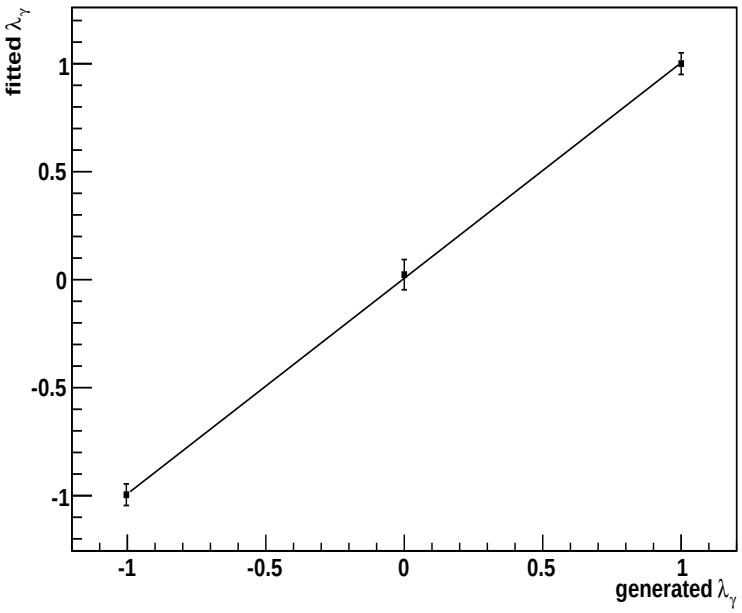

Figure 7.1: In both plots the anomalous coupling returned from the log-likelihood fit is plotted vs. the value of the anomalous coupling used to generate the 'data-like' sample that was used in the fit. The line shows the best fit through these points.

therefore a conservative reflection of the true 68% and 95% confidence limits.

7.2.1 Choosing the bin width

When performing the log-likelihood fit it is important to ensure that the most appropriate binning is used. In the ideal case each bin would be narrow thus giving a large number of bins over which the fit could take place. However, if the bin width is too small then large statistical fluctuations will exist between neighbouring bins in the reference samples. This problem is particularly noticeable in the tails of the reference samples where statistics are naturally low. Empty bins cause several problems as the probability density function in the fit is difficult to define if there are no bin entries. One solution for this problem was to change the bin size for the final bin so that it spanned a well described region and also as far out into the tail at high-P_T or mass as had been selected in the Monte Carlo samples. This not only solved the low statistics problem but also ensured that the sensitive information that is contained in the high-P_T/mass tails is kept.

In this study the P_T^γ, P_T^l and $M_{W\gamma}$ distributions were initially used to measure the sensitivity to anomalous couplings (figures 7.4, 7.5 and 7.6). The most appropriate binning for the P_T^γ, P_T^l and $M_{W\gamma}$ distributions is now discussed. It was found that in all cases increasing the upper edge of the fit range was the most important factor in improving the sensitivity. The distributions were binned up to a range of 3 TeV as this is where the unitarity cutoff was placed (see section 2.5). For each distribution the lower edge of the first bin was placed at the appropriate selection cut (P_T^γ at 100 GeV, P_T^l at 20 GeV, $M_{W\gamma}$ at 0 GeV). The lower edge of the large final bin was determined by the need for it to span a well described region in the reference histograms. Such a region could be characterised by the requirement that each bin should contain approximately 50 events (as a minimum). The SM template is the sample that has the least statistics in the region of interest for a given luminosity and therefore suitable positions for the lower edge of the last bin were derived from

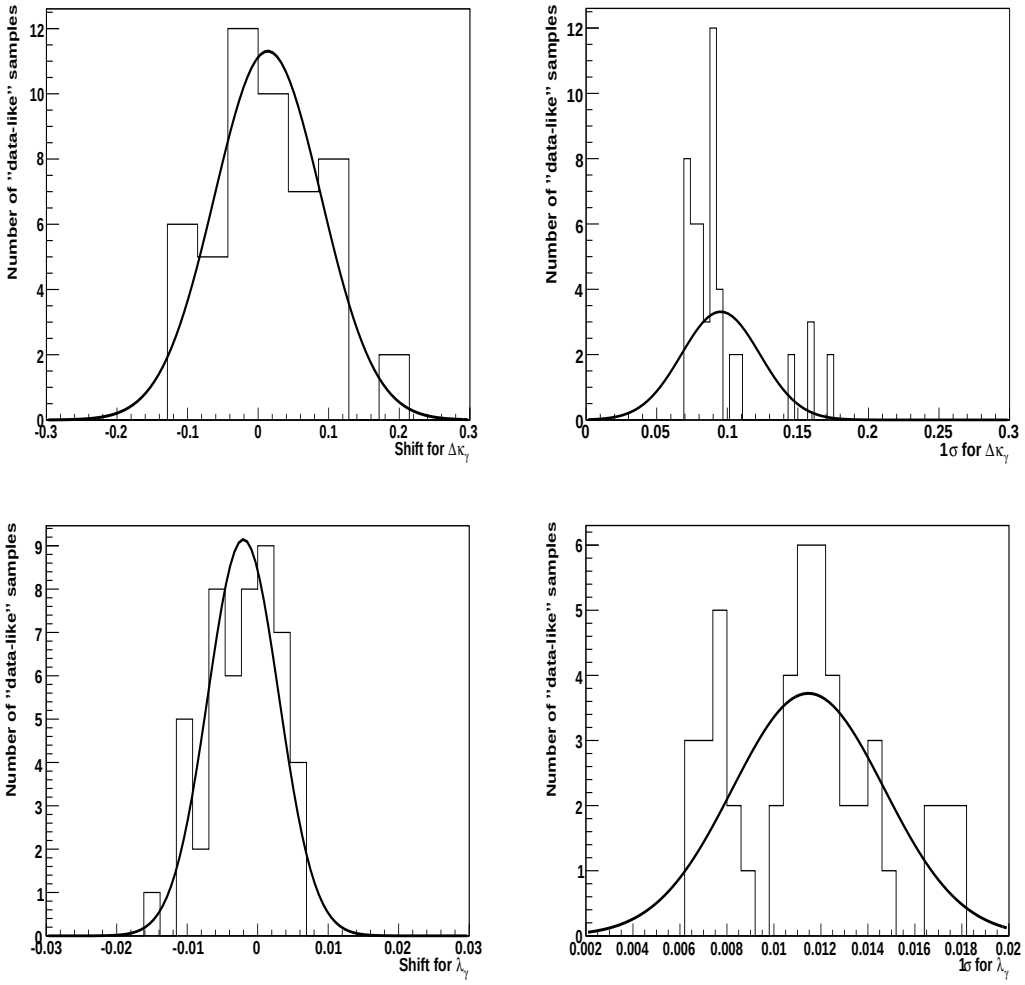

Figure 7.2: Top: The shift and 1 σ standard deviation statistical error given by the fit from 50 "data-like" samples when fitting for $\Delta\kappa_\gamma$. The shift has a mean of 0.015±0.010 and an RMS of 0.072±0.008. The 1 σ standard deviation has a mean of 0.095±0.004 and an RMS of 0.028±0.003. Bottom: The shift and 1 standard deviation statistical error given by the fit from 50 "data-like" samples when fitting for λ_γ. The shift has a mean of -0.002±0.001 and an RMS of 0.0050±0.0005. The 1 σ standard deviation has a mean of 0.0115±0.0004 and an RMS of 0.0032±0.0003. In all plots a Gaussian (solid line) has been fitted using a binned log-likelihood fit. The binning was chosen so that an acceptable goodness-of-fit, as reported by MINUIT (81), was found (see reference (80) for more details about goodness-of-fit).

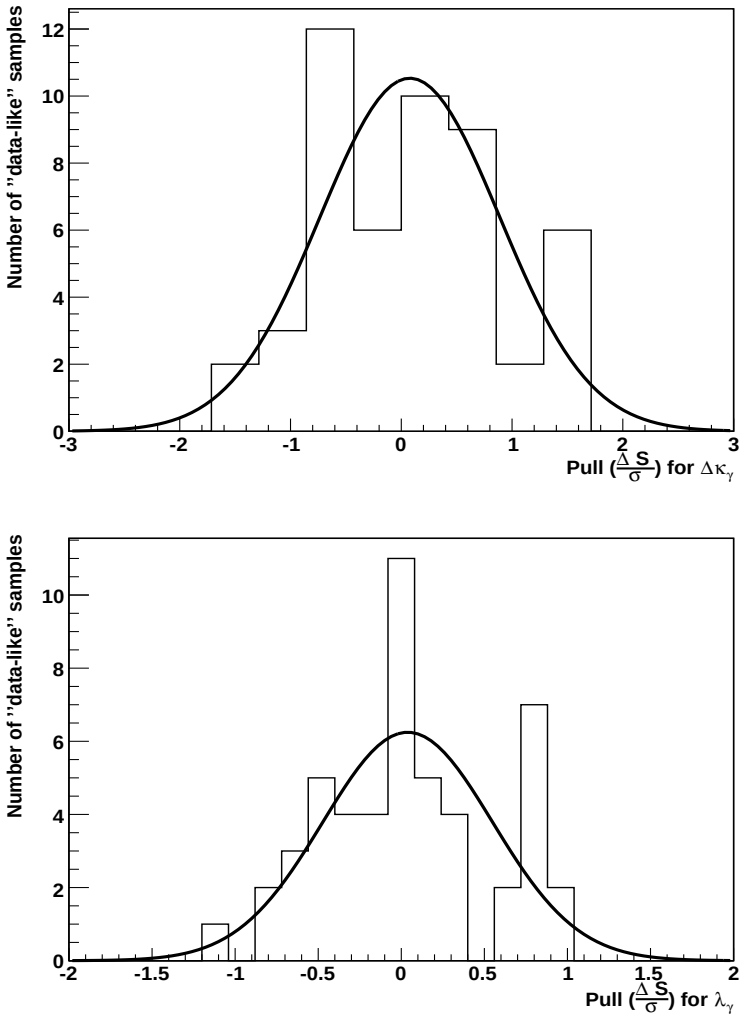

Figure 7.3: In both plots the pull distribution is plotted for 50 "data-like" samples. A Gaussian (solid line) has been fitted using a binned log-likelihood fit.

it. They were 600 GeV for the $M_{W\gamma}$ distribution, 300 GeV for the P_T^γ distribution and 170 GeV for the P_T^l distribution. The width of the bins was set to approximately 50 GeV for the P_T^γ and the P_T^l distributions and 75 GeV for the $M_{W\gamma}$ distributions. Further optimisation of these bin widths could improve the sensitivity. However, these bins (e.g. in the P_T^γ distribution) are in the part of the distribution which is less sensitive to anomalous couplings and little extra information is gained by making them narrower.

The $\eta_\gamma - \eta_l$ distribution was also considered for its sensitivity to the anomalous couplings (figure 7.7). The main sensitivity to the anomalous couplings was found to be in the central region and by binning over a range of $|\eta_\gamma - \eta_l| < 1.5$ with 10 equal sized bins this area was covered.

7.3 Reconstruction of the $M_{W\gamma}$ system

The $M_{W\gamma}$ system has to be reconstructed in several stages. To reconstruct the invariant mass of the $W\gamma$ system the four vectors of the W and γ need to be known. The four vector of the photon is directly measurable experimentally. However, when the W decays leptonically by $W \rightarrow l\nu$ the neutrino cannot be measured. The presence of the neutrino can be inferred from the momentum balance in the detector by equating the missing transverse momentum P_T^{miss} with the neutrino transverse momentum. This is insufficient for the reconstruction of $M_{W\gamma}$ as the neutrino longitudinal momentum P_z^ν is also required. However, by making the assumption that the W is on mass shell,

$$M_W^2 \equiv (P^\nu + P^l)^2 \tag{7.5}$$

the neutrino longitudinal momentum can be determined at the cost of a two-fold ambiguity in the solution.

By solving this equation the neutrino longitudinal momentum (2) is found to be:

$$P_z^\nu = \frac{1}{2{P_T^l}^2}[P_z^l(M_W^2 + 2P_T^l \cdot P_T^\nu) \pm |P^l|\sqrt{(M_W^2 + 2P_T^l \cdot P_T^\nu)^2 - 4{P_T^l}^2 {P_T^{miss}}^2}]. \tag{7.6}$$

The $M_{W\gamma}$ system can therefore be fully reconstructed with a two-fold ambiguity arising due to the neutrino longitudinal momentum. Experimentally it is impossible to know which is the correct solution. However, it has been observed (2) that the minimum of the two $M_{W\gamma}$ solutions is more likely to be correct because the $M_{W\gamma}$ distribution falls off rapidly at high $M_{W\gamma}$. The minimum $M_{W\gamma}$ solution was therefore always used here.

7.4 Event Selection optimisation and statistical limits on the anomalous couplings

The $\Delta\kappa_\gamma$ anomalous coupling is predicted to be less well constrained than λ_γ, which can be understood in terms of the different factors that enter into the matrix elements (eqn 2.5 and 2.6). These factors cause the effect of $\Delta\kappa_\gamma$ to be enhanced by $\frac{\sqrt{\hat{s}}}{M_W}$ whereas λ_γ is enhanced by $\frac{\hat{s}}{M_W^2}$. The $\Delta\kappa_\gamma$ coupling also has a lack of projection into the central observable region of the detector due to a factor proportional to $(1 \mp \cos\theta_\gamma^\star)$ compared to λ_γ being dependent on $\sin\theta_\gamma^\star$. From a theoretical position the main advantage that the $\Delta\kappa_\gamma$ coupling has over the λ_γ coupling is that it is enhanced only in the matrix element corresponding to the longitudinally polarized W boson state[2] and is thus sensitive to the W boson helicity.

The log-likelihood fitting method was used to determine the sensitivity to the anomalous couplings. This method can be used on any distribution that displays sensitivity to the anomalous couplings and it is therefore necessary to determine which distribution has better sensitivity. Between different distributions various sensitivities could occur. This is due to the different way information on the anomalous triple gauge couplings is reflected by the various distributions (section 2.4):

- The photon P_T^γ distribution contains a mixture of energy and angular information on the anomalous couplings.
- The $M_{W\gamma}$ distribution contains energy information on the anomalous couplings.
- The P_T^l distribution contains helicity and energy information on the anomalous couplings.

[2]The helicity of the longitudinally polarized W boson is $H_W = 0$ as the helicity operator is $\vec{\sigma}\cdot\hat{p}$ and the spin $\vec{\sigma}$ is perpendicular to the momentum $\hat{p}$ of the W boson.

- The $\eta_\gamma - \eta_l$ distribution contains angular information on the anomalous couplings.

In this study the anomalous couplings were investigated through the one-dimensional P_T^γ, P_T^l, $M_{W\gamma}$ and $\eta_\gamma - \eta_l$ distributions (figures 7.4, 7.5, 7.6 and 7.7). However, as the one-dimensional distributions contain different information on the anomalous couplings it would suggest that by combining them to create a multi-dimensional histogram a greater sensitivity could be achieved. This was attempted using the photon and lepton P_T distributions to create a two-dimensional histogram. However, the binning had to be made significantly coarser and this resulted in no gain in information on the triple gauge couplings with the statistics of 0.5 fb^{-1}. Therefore only one-dimensional distributions were used in this study.

The rest of this section describes the choice of distribution which was found to give the best sensitivity to the anomalous couplings and the statistical confidence limits it provides. However, in order to investigate this it is first necessary to optimise each distribution under study by applying selection cuts. This is therefore commented on below, before the most sensitive distribution to anomalous couplings is determined.

7.4.1 Event Selection Optimisation

Earlier in this chapter the various elements for distinguishing the $W\gamma$ signal from the background at ATLAS have been discussed and simple preselection cuts were applied. As this study is to determine the sensitivity to anomalous triple gauge couplings, any further cuts made should aim to maximise this sensitivity. The best placement of the photon, lepton and missing P_T cuts were considered using log-likelihood fits to evaluate the expected error. Primarily a photon P_T^γ distribution was used in the likelihood fit to measure this but to ensure that this did not favour any particular distribution the results were checked with both P_T^l and $M_{W\gamma}$ distributions.

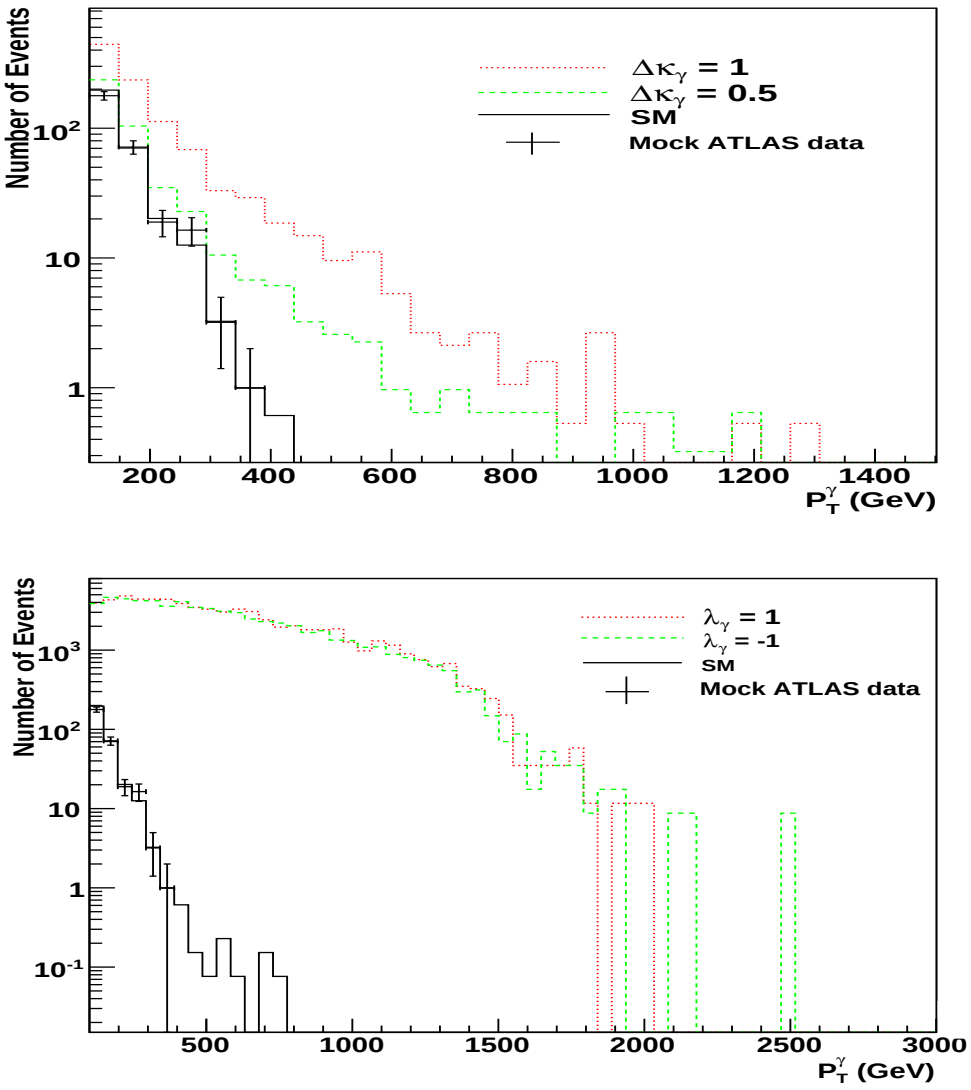

Figure 7.4: The top plot shows the photon P_T^γ distribution for the SM and $\Delta\kappa_\gamma$ reference samples. The bottom plot shows the photon P_T^γ distribution for the SM and λ_γ reference samples. Mock data corresponding to one ATLAS experiment (i.e. a 'data-like sample' corresponding to a luminosity of 0.5 fb^{-1}) and used in the fit in figure 7.9 are also included in both plots. The reference samples and ATLAS dataset include the background contribution. The reference samples are normalised to a luminosity of 0.5 fb^{-1}. (It should be noted that the log-likelihood fit is sensitive to the shape of the distribution only and not to the normalisation.)

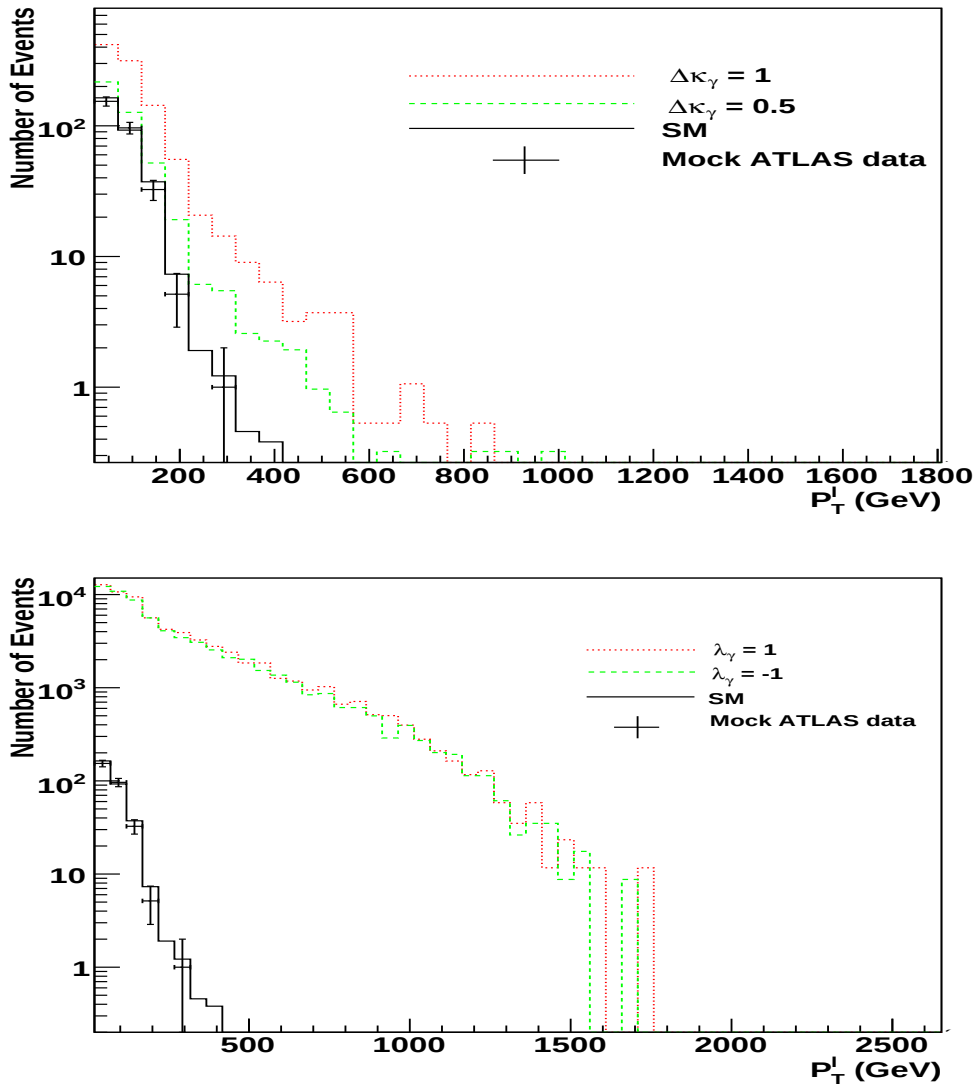

Figure 7.5: The top plot shows the lepton P_T^l distribution for the SM and $\Delta\kappa_\gamma$ reference samples. The bottom plot shows the lepton P_T^l distribution for the SM and λ_γ reference samples. Mock data corresponding to one ATLAS experiment (i.e. a 'data-like sample' corresponding to a luminosity of 0.5 fb^{-1}) and used in the fit in figure 7.9 are also included in both plots. The reference samples and ATLAS dataset include the background contribution. The reference samples are normalised to a luminosity of 0.5 fb^{-1}. (It should be noted that the log-likelihood fit is sensitive to the shape of the distribution only and not to the normalisation.)

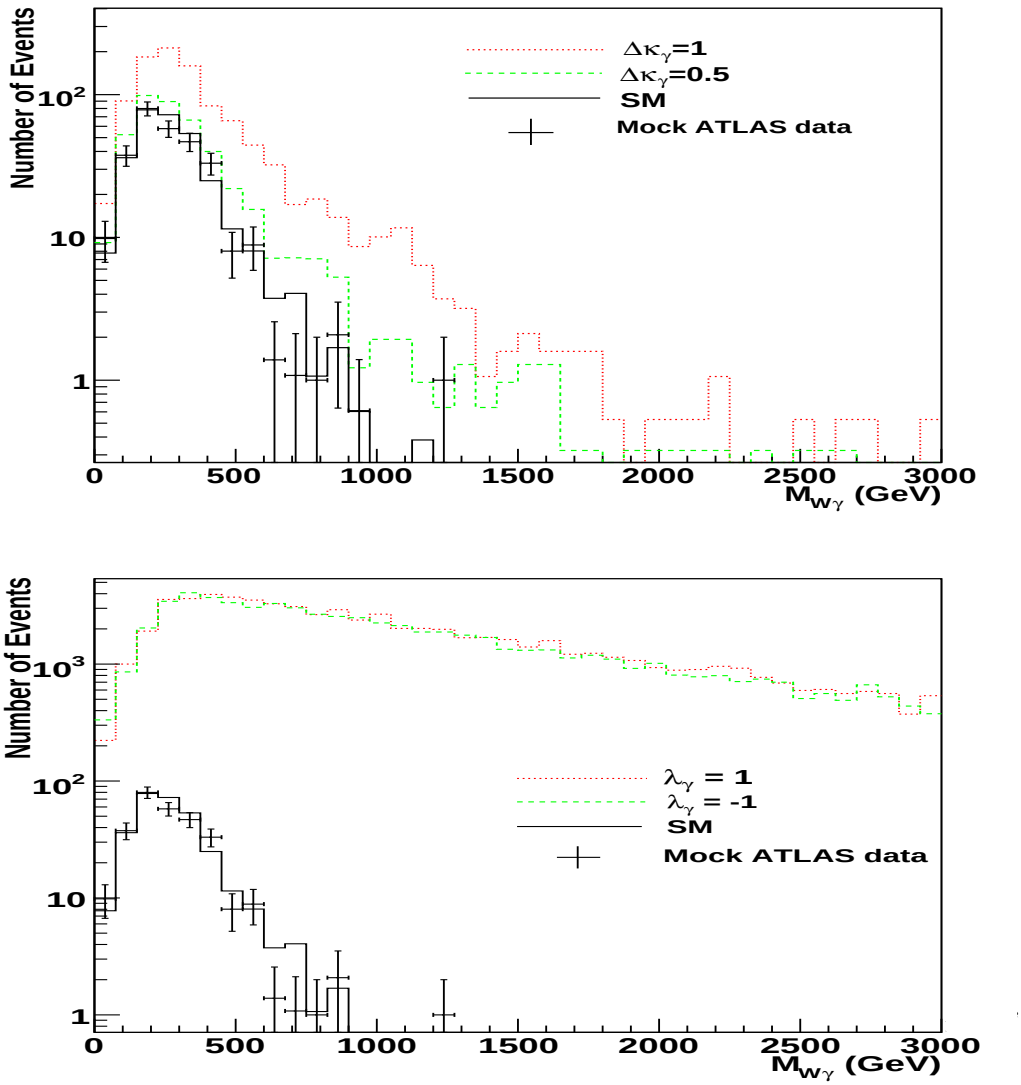

Figure 7.6: The top plot shows the $M_{W\gamma}$ distribution for the SM and $\Delta\kappa_\gamma$ reference samples. The bottom plot shows the $M_{W\gamma}$ distribution for the SM and λ_γ reference samples. Mock data corresponding to one ATLAS experiment (i.e. a 'data-like sample' corresponding to a luminosity of 0.5 fb^{-1}) and used in the fit in figure 7.9 are also included in both plots. The reference samples and ATLAS dataset include the background contribution. The reference samples are normalised to a luminosity of 0.5 fb^{-1}. (It should be noted that the log-likelihood fit is sensitive to the shape of the distribution only and not to the normalisation.)

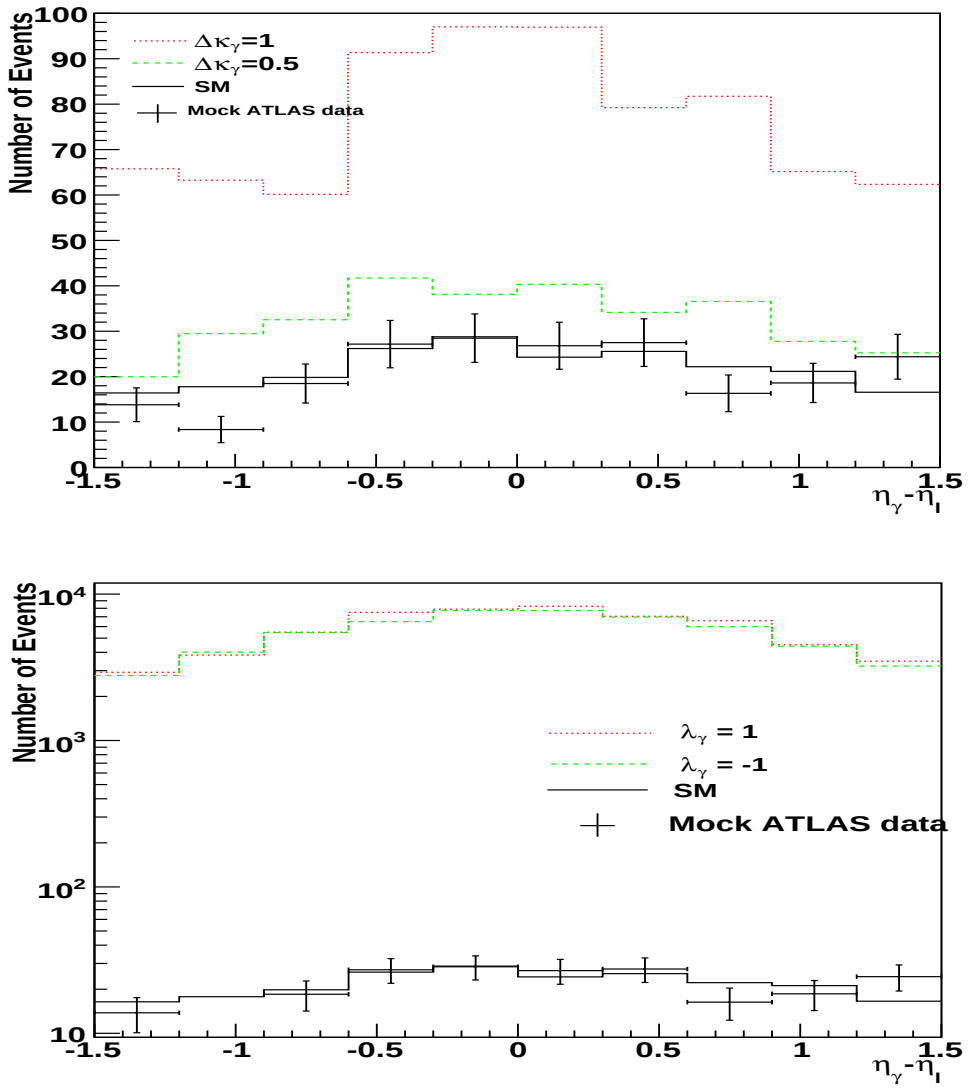

Figure 7.7: The top plot shows the $\eta_\gamma - \eta_l$ distribution for the SM and $\Delta\kappa_\gamma$ reference samples. The bottom plot shows the $\eta_\gamma - \eta_l$ distribution for the SM and λ_γ reference samples. Mock data corresponding to one ATLAS experiment (i.e. a 'data-like sample' corresponding to a luminosity of 0.5 fb^{-1}) and used in the fit in figure 7.9 are also included in both plots. The reference samples and ATLAS dataset include the background contribution. The reference samples are normalised to a luminosity of 0.5 fb^{-1}. (It should be noted that the log-likelihood fit is sensitive to the shape of the distribution only and not to the normalisation.)

In all cases as the respective P_T cuts were increased from the preselection values the sensitivity was degraded (table 7.2 shows the expected 95% confidence level as determined by the photon P_T^γ distribution). The final selection cuts chosen were therefore the same as the preselection cuts. This is not ideal as it indicates that possibly the preselection cuts are too harsh and interesting events are being lost. However, nothing could be done to loosen the preselection cuts as they were determined by the generator level cuts on the fully simulated background samples. These samples had been produced via the central production facility and it was not possible to regenerate them with looser cuts with the resources available. It is therefore possible that if these cuts could be loosened then the sensitivity to anomalous triple gauge couplings could be improved. However, it has also been shown at the Monte Carlo generator level that the enhancement of the anomalous couplings is predominantly in the high-P_T^γ region which this study examines. The change in the expected 95% confidence level spread as the P_T^γ cut is decreased is illustrated in figure 7.8. As the P_T^γ cut decreases the expected 95% confidence level decreases indicating an improved sensitivity. However, the rate of change of the sensitivity improvement is also decreasing indicating that the preselection cuts are in an acceptable position.

7.4.2 Choosing the most sensitive distribution to anomalous couplings

The statistical limits on the anomalous couplings were investigated by fitting the photon P_T, lepton P_T, $M_{W\gamma}$ and $\eta_\gamma - \eta_l$ distributions in turn. For each fit a statistically independent data sample corresponding to 0.5 fb^{-1} was used to represent the experiment (the 'data-like' sample). The expected 95% confidence limit for each of 50 such experiments was measured for each distribution and the mean values of these limits are tabulated in table 7.3. The smaller that the expected 95 % confidence limit interval is, the more sensitive the distribution is to the anomalous coupling. The photon transverse momentum distribution was found to be the most sensitive to

Photon P_T (GeV)	$\Delta\kappa_\gamma$ expected 95 % C.L.	λ_γ expected 95 % C.L.
> 100	0.36	0.042
> 105	0.37	0.043
> 110	0.39	0.043
> 115	0.41	0.044
> 120	0.45	0.044
Lepton P_T (GeV)	$\Delta\kappa_\gamma$ expected 95 % C.L.	λ_γ expected 95 % C.L.
> 20	0.36	0.042
> 25	0.36	0.043
> 30	0.37	0.043
> 35	0.38	0.043
> 40	0.39	0.044
Missing P_T (GeV)	$\Delta\kappa_\gamma$ expected 95 % C.L.	λ_γ expected 95 % C.L.
> 15	0.36	0.042
> 20	0.37	0.043
> 25	0.37	0.043
> 30	0.37	0.043

Table 7.2: The expected 95 % C.L. interval (from 50 experiments) for $\Delta\kappa_\gamma$ and λ_γ for various P_T cuts when measured using the photon P_T^γ distribution. When a cut is varied the other cuts are positioned at the preselection values.

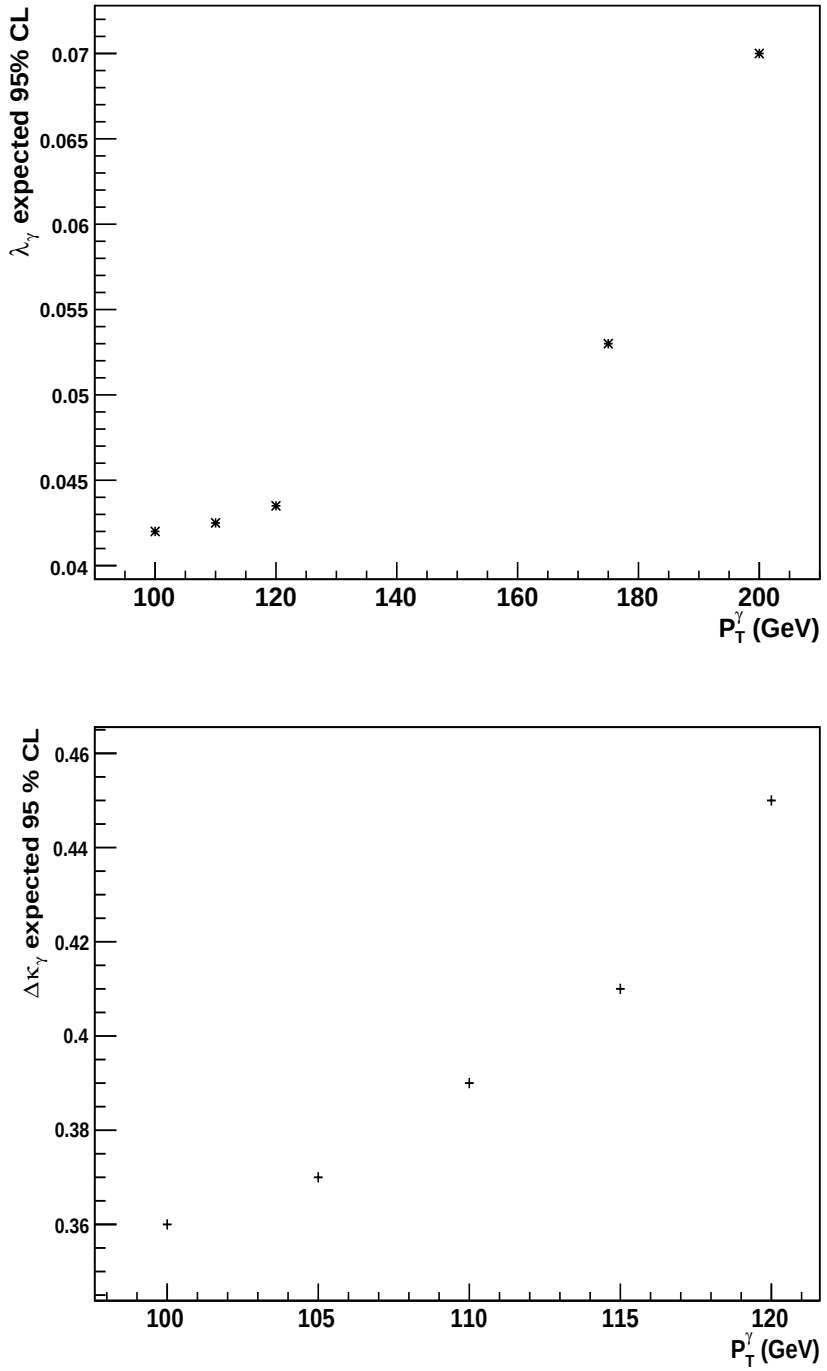

Figure 7.8: Top: The statistical sensitivity to the λ_γ anomalous coupling vs P_T^γ cut. Bottom: The statistical sensitivity to the $\Delta\kappa_\gamma$ anomalous coupling vs P_T^γ cut.

$\Delta\kappa_\gamma$ and λ_γ. The photon P_T distribution, shown in figure 7.4, was therefore chosen as the best one for the determination of anomalous couplings in this study.

Distribution	$\Delta\kappa_\gamma$ spread at 95 % C.L.	λ_γ spread at 95 % C.L.
P_T^γ	0.36	0.042
P_T^l	0.40	0.043
$M_{W\gamma}$	0.40	0.044
$\eta_\gamma - \eta_l$	0.37	0.043

Table 7.3: Table of the average width of the 95 % C.L. interval for 50 experiments.

For the P_T^γ distribution an example of the log-likelihood distribution resulting from the fit for one experiment is shown in figure 7.9. The mean result obtained from 50 experiments with Standard Model input data for either $\Delta\kappa_\gamma$ or λ_γ varying was:

$$\Delta\kappa_\gamma = 0.015^{+0.093}_{-0.097}, \qquad \lambda_\gamma = -0.002^{+0.010}_{-0.013}. \tag{7.7}$$

The statistical limits derived from 50 experiments at the 95 % confidence level for $\Delta\kappa_\gamma$ or λ_γ varying were:

$$-0.207_{stat95\%} < \Delta\kappa_\gamma < 0.151_{stat95\%}, \qquad -0.023_{stat95\%} < \lambda_\gamma < 0.019_{stat95\%}. \tag{7.8}$$

For both $\Delta\kappa_\gamma$ and λ_γ anomalous couplings varying individually the 68% and 95% confidence levels are consistent with the Standard Model prediction of 0. As expected the λ_γ coupling is more tightly constrained compared to the $\Delta\kappa_\gamma$ coupling.

By allowing both $\Delta\kappa_\gamma$ and λ_γ anomalous couplings to vary together a two parameter fit was made (bottom figure 7.9). The tighter constraint on λ_γ relative to $\Delta\kappa_\gamma$ is again illustrated.

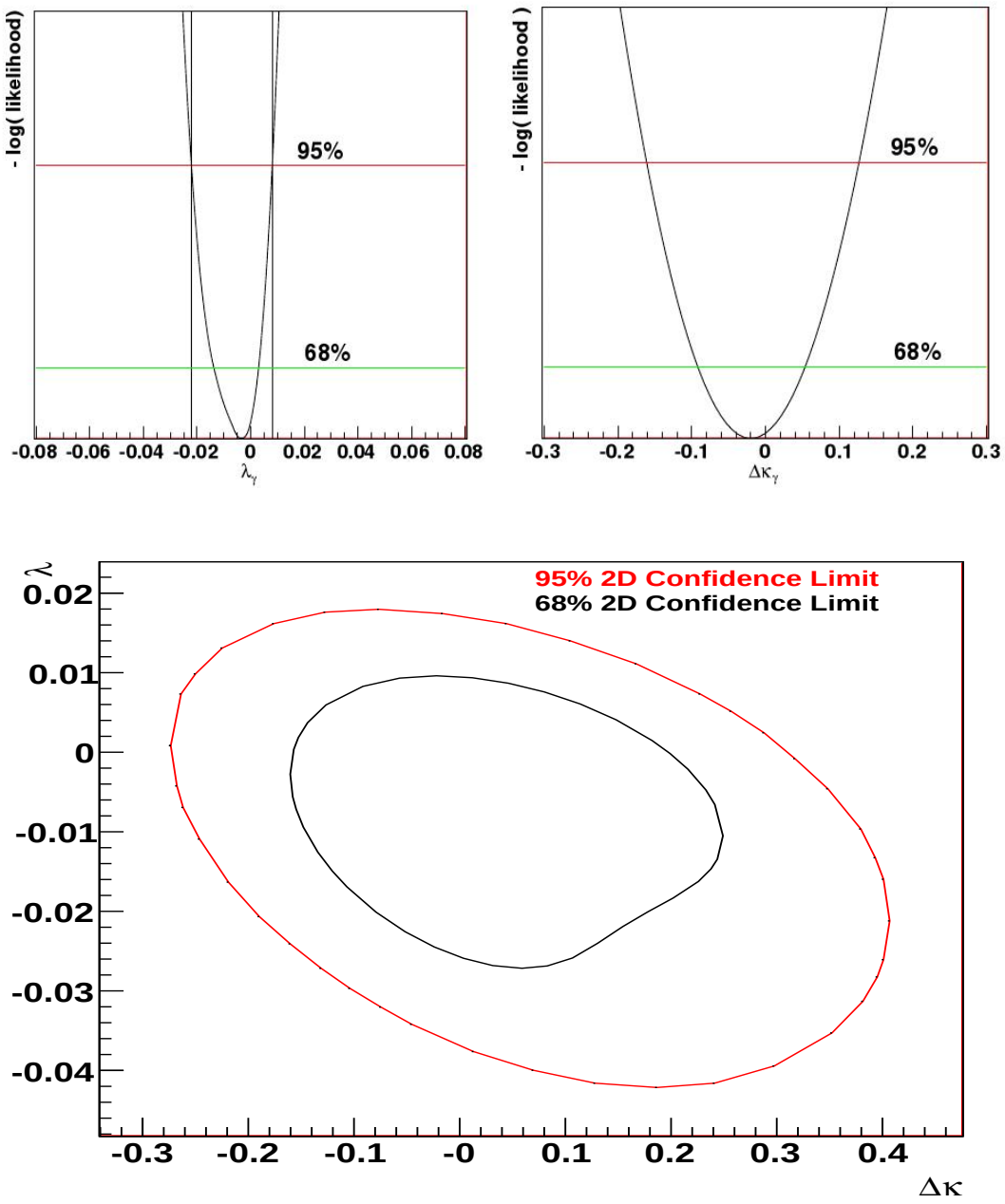

Figure 7.9: Typical log-likelihood curves for one experiment. The top plots show the 68% and 95% 1D confidence limits for λ_γ and $\Delta\kappa_\gamma$. The bottom plot shows the 68% and 95% 2D confidence limits, at log-likelihood intervals of +1.8 and +3 respectively, for λ_γ vs $\Delta\kappa_\gamma$. These figures correspond to the dataset used in figure 7.4.

7.5 Systematic Errors

The limits on the anomalous couplings will be determined by the statistical sensitivity combined with the effect of various sources of systematic error. These systematic errors will arise due to a lack of knowledge of the detector and the underlying physics approximations of the Monte Carlo models. However, certain systematic errors that only affect the normalisation of the data can be neglected as the likelihood fit used is insensitive to this, depending only on the shape of the distribution. Therefore, systematic errors such as luminosity can be ignored. The various other systematic errors that could affect the prediction of anomalous triple gauge couplings are now investigated.

In the case of finding the statistical error the log-likelihood fit was used to derive confidence limits that represent the error as explained above. In order to determine the systematic error from a specific source the template histograms used in the likelihood fit were altered to represent a specific new assumption. The likelihood fit was then redone for 50 data-like samples which were not modified (i.e. that used the original assumptions). This allowed the change in the central fitted value (i.e. the minimum of the log-likelihood) for $\Delta\kappa_\gamma$ and λ_γ to be observed for each data-like sample. The mean shift of the central value for each anomalous coupling was then used as the systematic error for the given error source. It was determined in all cases that the systematic error was small compared to the 68% C.L. statistical error (see table 7.4).

7.5.1 Background rate estimate uncertainty

This study has reduced the influence of the background by applying stringent cuts. However, the background rates as predicted by Monte Carlo are uncertain. This gives an uncertainty on the Standard Model photon P_T distribution shape as the

background and $W\gamma$ P_T^γ distributions have different shapes. This uncertainty could lead to an incorrect measurement that anomalous couplings are present in data, or to poorly estimated limits. After a period of running the experiment, the uncertainty on background normalisations will be reduced as the various backgrounds will be constrained by data in nearby kinematic regions insensitive to anomalous couplings. However, in an early measurement, such as this, the effect that different background rates can have will be enhanced.

The method used to estimate this systematic error was to halve or double the background rate normalisation in the template samples. For illustrative purposes the background contribution to the photon P_T distribution is shown in figure 7.10 for the Standard Model case. As described previously, the shift in the mean minimum value from the likelihood fit was studied. It was observed that doubling the background produced a larger systematic shift than halving it as shown in table 7.4. For $\Delta\kappa_\gamma$ this shift was approximately two orders of magnitude smaller than the 68 % confidence limit while for λ_γ it was approximately one order of magnitude smaller. The effect of varying the background rate on the sensitivity to anomalous couplings is therefore minor.

7.5.2 Parton Density Function systematics

Uncertainties in the parton densities (PDFs) in the proton also lead to uncertainties in the rates of processes and kinematic distributions at the LHC. In addition as the LHC will probe energies that are higher than the PDFs currently fitted, the PDFs used in this study will no doubt be modified as they are constrained at ATLAS and by other LHC experiments. This study examines the differences between the current PDFs and their effect on the systematic error. The default PDF used in the generation of the fully simulated $W\gamma$ datasets was CTEQ6l (82). This was compared with two different PDFs CTEQ6m (82) and MRST2002NLO (83). The method used to study the impact of these differences on the sensitivity to anomalous

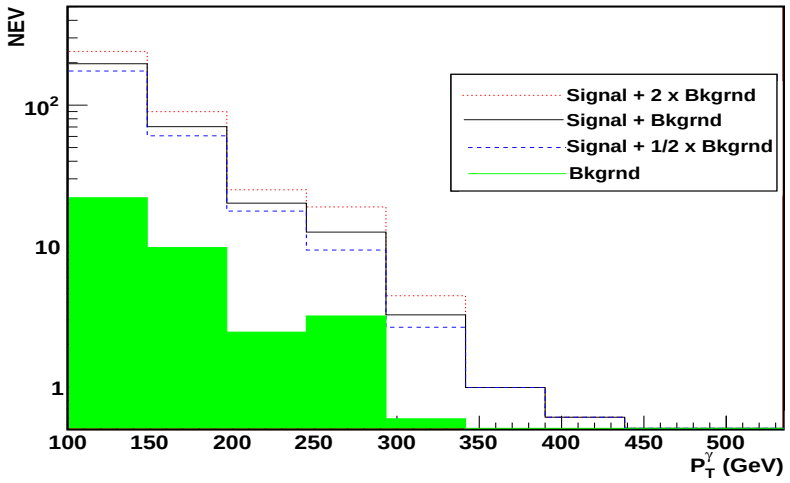

Figure 7.10: The P_T^γ distribution for the SM signal with different contributions of the background. Also shown is the background contribution alone (solid area). This plot was produced from fully simulated data and normalised to a luminosity of 0.5 fb^{-1}. The preselection cuts have been applied.

couplings is described below.

Ideally when studying the PDF systematic error, fully simulated data would be available for each PDF. Time constraints on producing a fully simulated dataset meant this was not feasible. Therefore, the photon transverse momentum was modelled at generator level with SHERPA for the SM and anomalous templates for each of the PDFs. For each PDF a bin-by-bin extraction of the generated photon P_T distribution was made. Using the CTEQ6l PDF (as used in the full simulation) as a reference the fully simulated samples were then reweighted with a different PDF. Fifty log-likelihood fits were then performed to obtain the mean shift. For both $\Delta\kappa_\gamma$ and λ_γ the mean shift was approximately 0.002 for both CTEQ6m and MRST2002NLO (see table 7.4). The effect of this shift is therefore relatively much more significant on the more sensitive λ_γ measurement. However, it is still small compared to the 68 % C.L. statistical error.

7.5.3 Higher-order uncertainty on the signal shape

The part of this uncertainty which is a scaling factor does not affect the likelihood fit. However, there is another part which affects the signal shape. By modifying the shape of the photon P_T distribution in the template samples the systematic shift can be studied. The extent to which the shape of the photon P_T distribution was modified was obtained by comparing the generator-level distributions from SHERPA with BHO or AYLEN. Correction factors were then applied bin-by-bin to the fully simulated Monte Carlo prediction.

The method used to study this systematic was to bin the generator level photon P_T distribution from SHERPA, BHO and AYLEN. A scaling factor for each bin was then obtained that changed the SHERPA distribution shape to that of the BHO or AYLEN shape. This scaling factor was then applied on a bin-by-bin basis to the fully simulated SHERPA photon P_T distribution. The systematic error that originated from using BHO was larger than the systematic error when using AYLEN, therefore the BHO systematic error was used. The systematic error obtained from using BHO was -0.0001 for $\Delta\kappa_\gamma$ and no shift was observed for λ_γ to the precision of four decimal places.

7.5.4 Photon energy scale and resolution error

There is an uncertainty on the photon energy scale predicted by the ATLAS simulation. The effect that this would have is that the ATLAS simulation could predict that observed photon energies are higher or lower than in data, parametrised by a scaling factor. In this analysis, should the photon energies in the templates be shifted relative to the real data, then it is possible that the presence of anomalous couplings would be incorrectly inferred.

In order to study this effect each photon in the fully simulated template samples

had its energy shifted by ±1%. This was done individually to each photon before any analysis cuts were applied. Using the likelihood fit the shift in the most likely value was found for both $\Delta\kappa_\gamma$ and λ_γ as shown in table 7.4.

In addition to the error on the photon energy scale, there is also an uncertainty on the photon energy resolution. The photon resolution indicates the degree to which the true photon energy is smeared out by the ATLAS detector. Depending upon how incorrect the photon resolution is, it can cause the P_T^γ distribution shape to change as photons near the boundary edge of a bin may be shifted into the next bin. Due to the fact that truth information is needed to study this effect it becomes complicated as true photons need to be matched to reconstructed photons. Further difficulties arise due to fake photons that do not have a true primary photon present. Therefore, in order to examine whether an incorrect photon resolution could cause a large systematic error, only the $W\gamma$ signal was examined as each of these events should have a primary photon present. In order to match successfully a true photon to a reconstructed photon they had to be within $\Delta R < 0.4$.

The photon resolution systematic error was studied by changing the reconstructed photon P_T to that of:

$$P_T(shifted) = (P_T(reco) - P_T(truth)) \times S + P_T(truth). \tag{7.9}$$

The appropriate value of S was 0.90 or 1.10 as previously found by ATLAS (64) (i.e. a 10% relative uncertainty in the photon energy resolution). The $P_T(shifted)$ value was changed for all photons before any other analysis cuts were applied. Only the template samples used this $P_T(shifted)$ value and all backgrounds were neglected. The likelihood fit on the photon P_T distribution was then used in order to observe the mean shift in the central fitted value of $\Delta\kappa_\gamma$ or λ_γ (table 7.4). It was observed that the maximum average shift produced for $\Delta\kappa_\gamma$ was 0.0325 and for λ_γ it was 0.0024.

7.5.5 Lepton energy scale error

The lepton energy scale was also investigated as a possible source of systematic error. The same method as used for the photon energy scale was employed. The results are found in table 7.4 and this systematic error was also observed to be small for both $\Delta\kappa_\gamma$ and λ_γ.

7.5.6 Jet P_T scale error

Due to the jet veto cut that was applied in selecting events, the jet P_T scale was investigated as a possible systematic error source. The same method as described for the photon energy scale was used but applied to the jet P_T. As the jet energy scale is usually the variable studied there was no previously defined value by which to shift the jet P_T scale. The amount of this shift was therefore approximated by using the value predicted from jet energy scale studies. Although it should be noted that ATLAS aims for a 1% uncertainty on the jet energy scale with early running it is more likely to be 4 to 5 % (84). For this study it is therefore more appropriate to use the larger energy scale uncertainty of 5 %. It was observed that the maximum shift produced for $\Delta\kappa_\gamma$ was 0.0162 and for λ_γ it was 0.0025.

7.6 Combining the statistical and systematic errors to give a prediction

For each component of the systematic uncertainty (table 7.4) the largest shift was used to represent the systematic error. These errors were taken to be symmetric. The combined systematic error was thus found by adding all the components in quadrature to be:

$$\pm 0.043 \text{ for } \Delta\kappa_\gamma \tag{7.10}$$

Systematic shift from the mean minimum (0.015) for $\Delta\kappa_\gamma$												
Background Rate		PDF uncertainty		NLO scale	Photon energy scale		Photon resolution		Lepton energy scale		Jet P_T scale	
k=1/2	k=2	CTEQ6m	MRST2002		99%	101%	90%	110%	99%	101%	95%	105%
0.0050	−0.0065	−0.0023	−0.0022	−0.0001	−0.022	−0.0051	−0.0325	−0.0021	−0.0029	−0.0043	0.0162	−0.0021
Systematic shift from the mean minimum (−0.002) for λ_γ												
Background Rate		PDF uncertainty		NLO scale	Photon energy scale		Photon resolution		Lepton energy scale		Jet P_T scale	
k=1/2	k=2	CTEQ6m	MRST2002		99%	101%	90%	110%	99%	101%	95%	105%
0.0007	−0.0012	−0.0016	−0.0013	0.0000	−0.0022	−0.0029	0.0024	−0.0024	−0.0025	0.0012	0.0005	−0.0025

Table 7.4: Estimated systematic errors, evaluated as mean shifts to the central fitted value. The method used to determine each systematic error is described in the text.

$$\pm 0.0055 \text{ for } \lambda_\gamma. \tag{7.11}$$

For both cases the statistical error can be seen to dominate. This indicates that the expected sensitivity will continue to improve with luminosity. However, as the experiment progresses it is also likely that the systematic errors will be better understood and some of the pessimistic values here will be reduced, thus also improving the sensitivity further.

7.6.1 Conclusions on the sensitivity to $\Delta\kappa_\gamma$ and λ_γ

For both $\Delta\kappa_\gamma$ and λ_γ a binned maximum likelihood fit to the photon P_T distribution was used to extract limits on the anomalous couplings. The photon P_T distribution, that contains both energy and angular information, was found to be the most sensitive distribution to use. Therefore, the photon P_T distribution was used. By combining in quadrature the statistical and systematic errors, that had been found by averaging over 50 experiments, a prediction for the sensitivity was found at the 1 standard deviation level (when allowing only one parameter to change at a time) to be:

$$\Delta\kappa_\gamma = 0.015^{+0.102}_{-0.106}, \qquad \lambda_\gamma = -0.002^{+0.011}_{-0.014}, \tag{7.12}$$

and at the 95 % confidence limit:

$$-0.23 < \Delta\kappa_\gamma < 0.17, \qquad -0.025 < \lambda_\gamma < 0.021. \tag{7.13}$$

Chapter 8

Conclusions

When protons are collided in the LHC, the ATLAS level-1 calorimeter trigger will be vital to the successful recording of the most useful events. Part of the work reported in this thesis was part of the testing of the cluster processor module and the calibration of the common merger module in the trigger, to attempt to ensure that the level-1 calorimeter trigger would operate reliably. The tests carried out on the cluster processor module have indicated that it will operate reliably over the temperature range tested. The prototype calibration mechanism for the common merger module has also shown that it can be successfully calibrated.

In the study of anomalous triple gauge bosons at ATLAS the trigger will play a vital role in identifying the $W\gamma$ events for data storage and analysis. The selection of these events will most likely be done via a combination of the photon, electron and muon triggers, all of which have thresholds that are set beneath the final cuts in the analysis. The Monte Carlo study reported in this thesis has attempted to measure how, after 0.5 fb^{-1} of ATLAS data has been collected, the sensitivity to anomalous couplings can be determined. A binned log likelihood fit using the photon P_T distribution was found to give the greatest sensitivity at the 1σ level (when allowing only one parameter to change at a time). The expected sensitivity evaluated

as the mean fit result over an ensemble of 50 Monte Carlo experiments was:

$$\Delta\kappa_\gamma = 0.015^{+0.102}_{-0.106}, \qquad \lambda_\gamma = -0.002^{+0.011}_{-0.014}, \tag{8.1}$$

and at the 95 % confidence limit:

$$-0.23 < \Delta\kappa_\gamma < 0.17, \qquad -0.025 < \lambda_\gamma < 0.021. \tag{8.2}$$

These results correspond to an integrated luminosity of 0.5 fb^{-1}, which is a reasonable expectation of what can be collected after approximately 1 year. In the study of anomalous triple gauge couplings at ATLAS it is also interesting to see how these results will evolve with luminosity and thus if a large improvement can be expected. To make a reliable estimate of the sensitivity at a higher luminosity would require significantly more simulated data and this is currently not available. However, another study using fast simulation (2), which has examined only the higher luminosity region, found that a factor of 10 increase in the luminosity would improve the sensitivity by a factor of 2. This indicates how the sensitivity can evolve with luminosity, however, direct comparison between the current study and the previous one can not be made because of the different form factors used to prevent unitarity violation. The LHC will have the potential to constrain the anomalous couplings better than current and previous experiments. After approximately three years of running, the ATLAS experiment should have constrained the $\Delta\kappa_\gamma$ coupling by at least an order of magnitude better than the current Tevatron experiments (31). For the λ_γ coupling, ATLAS should be able to constrain it by two orders of magnitude better than the Tevatron and one order of magnitude better than LEP (27).

Bibliography

[1] U. Baur and D. Zeppenfeld, Nuclear Physics B **308**, 127 (1988).

[2] M. Dobbs, *Probing the Three Gauge-boson Couplings in 14 TeV Proton-Proton Collisions*, PhD thesis, Physics and Astronomy, University of Victoria, 1997.

[3] D. de Florian and A. Signer, European Physical Journal C **16**, 105 (2000).

[4] W. Cottingham and D. Greenwood, *An Introduction to the Standard Model of Particle Physics* (Cambridge University Press, 1998).

[5] W. M. Yao *et al.*, Journal of Physics G **33**, 1+ (2006).

[6] E. Fermi, Zeitschrift fur Physik **88** (1934).

[7] M. Peskin and D. Schroeder, *An Introduction to Quantum Field Theory* (Addison-Wesley Publishing Company, 1995).

[8] M. Kaku, *Quantum Field Theory* (Oxford Student Union, 1993).

[9] A. Zee, *Quantum field theory in a nutshell* (Princeton University Press, 2003).

[10] M. Maggiore, *A Modern Introduction to Quantum Field Theory* (Oxford University Press, 2005).

[11] LHC - THE LARGE HADRON COLLIDER, http://lhc.web.cern.ch/lhc/, 2008.

[12] M. R. Whalley *et al.*, (2005), hep-ph/0508110.

[13] D. Bourilkov *et al.*, (2006), hep-ph/0605240.

[14] W. Giele *et al.*, (2002), hep-ph/0204316.

[15] R. Brunelire, Eur. Phys. J. C **33** (2004).

[16] K. Hagiwara, R. D.Peccei, and D. Zeppenfeld, Nuclear Physics **B**, 253 (1987).

[17] U. Baur, T. Han, and J. Ohnemus, Physical Review **D48**, 5140 (1993).

[18] E. Accomando, A. Denner, and S. Pozzorini, Physical Review **D65**, 073003 (2002), hep-ph/0110114.

[19] T. Gleisberg *et al.*, JHEP **02**, 056 (2004), hep-ph/0311263.

[20] R. W. Brown, D. Sahdev, and K. O. Mikaelian, Physical Review **D20**, 1164 (1979).

[21] M. A. Samuel and J. Reid, Phys. Rev. D **35**, 3505 (1987).

[22] F. Mamedov, AIP CONF.PROC. **541**, 202 (2000).

[23] U. Baur, S. Errede, and G. Landsberg, Physical Review **D50**, 1917 (1994).

[24] H. Aihara *et al.*, (1995), hep-ph/9503425.

[25] T. Barklow *et al.*, (1996), hep-ph/9611454.

[26] S. Haywood *et al.*, (1999), hep-ph/0003275.

[27] ALEPH, DELPHI, L3, OPAL and the LEP Electroweak Working Group, J. Alcaraz *et al.*, hep-ex/0612034 (2006).

[28] Electroweak boson pair production at CDF, in *Presented at the 27th International Conference on High Energy Physics, Glasgow, England, 21-27 Jul. 1994*, pp. 21–27, 1994.

[29] CDF, T. Aaltonen *et al.*, Phys. Rev. **D76**, 111103 (2007), arXiv:0705.2247 [hep-ex].

[30] D0, V. Abazov, Physical Review **D71**, 091108 (2005).

[31] D0, V. Abazov *et al.*, Physical Review **D74**, 057101 (2006), hep-ex/0608011.

[32] G. Aad *et al.*, The ATLAS experiment at the CERN Large Hadron Collider, https://twiki.cern.ch/twiki/bin/viewfile/Atlas/AtlasTechnicalPaper?rev=1;filename=Main_jins 2008.

[33] ATLAS Collaboration, various pictures from ATLAS, http://atlasexperiment.org/atlas_photos.html.

[34] C. Hill, Ion sources and electron guns, http://linac2.home.cern.ch/linac2/seminar/seminar.htmNEG, 2008.

[35] ATLAS Collaboration, ATLAS Detector and Physics Performance Technical Design Report, Vol 1, 1999.

[36] Idaho State University, Radiation related definitions, http://physics.isu.edu/radinf/terms.htm, 2008.

[37] C. Parungo and D.Brooks, *The pregnant surgical patient* (Harvard Medical School, 2007).

[38] F. Soloman and R.Marston, *The medical implications of nuclear war* (National academies press, 1986).

[39] ATLAS Level-1 Trigger Group, ATLAS Level-1 Technical Design Report, LHCC 98-14, 1998.

[40] ATLAS HLT/DAC/DCS Group, High-Level Trigger, Data Acquisition and Controls TDR, CERN/LHCC/2003-022, 2003.

[41] J. Garvey *et al.*, IEEE Trans. Nucl. Sci. **51**, 356 (2004).

[42] S. Hillier *et al.*, ATLAS Level-1 Calorimeter Trigger Cluster Processor Module, http://hepwww.rl.ac.uk/Atlas-L1/Modules/Modules.html, 2006, Module Specification version 2.0.3.

[43] I. P. Brawn and C. N. P. Gee, ATLAS Calorimeter First Level Trigger-Common Merger Module, http://hepwww.rl.ac.uk/Atlas-L1/Modules/Modules.html, 2006.

[44] P. Hanke, Specifications of the Pre-Processor Module (PPM) for the ATLAS Level-1 Calorimeter Trigger, http://hepwww.rl.ac.uk/Atlas-L1/Modules/Modules.html, 2003, Module Specification version 2.x.

[45] U. Schafer *et al.*, ATLAS Level-1 Calorimeter Trigger Jet/Energy Processor Module, http://hepwww.rl.ac.uk/Atlas-L1/Modules/Modules.html, 2006, Module Specification version 1.2.

[46] B. Taylor, IEEE **1**, 087 (1997).

[47] J. Christiansen, TTCrx reference manual, http://ttc.web.cern.ch/TTC/TTCrx manual3.8.pdf, 2003.

[48] COOL - LCG conditions database project, http://lcgapp.cern.ch/project/CondDB/, 2008.

[49] A. Camard, ATLAS NOTE (2003), ATL-LARG-2003-001.

[50] T. Gillman, TTCrx chip: temperature and voltage effects, Mainz L1CALO conference, 2005.

[51] W. Qian, TTC FanoutModule specification, hepwww.rl.ac.uk/Atlas-L1/Modules/TTC/TTCF, 2003, RAL.

[52] S. Catani, F. Krauss, B. R. Webber, and R. Kuhn, Journal of High Energy Physics **2001**, 063 (2001).

[53] P. Z. Skands, AIP Conf. Proc. **792**, 73 (2005), hep-ph/0507129.

[54] The GridPP collaboration, Journal of Physics G: Nuclear and Particle Physics **32 N1-N20** (2006).

[55] M. Mangano *et al.*, Annual Review of Nuclear and Particle Science **55**, 555 (2005).

[56] T. Sjöstrand *et al.*, Journal of High Energy Physics **2006**, 026 (2006).

[57] S. Mrenna, (1999), hep-ph/9902471.

[58] S. Frixione and B. R. Webber, JHEP **0206**, 029 (2002).

[59] Geant4 Collaboration *et al.*, Nuclear Instruments and Methods in Physics Research A **506**, 250 (2003).

[60] ATLAS Collaboration, Top level tags in the ATLAS geometry database, https://twiki.cern.ch/twiki/bin/view/Atlas/AtlasGeomDBTags, 2008.

[61] J. Virzi, A software package to convert SHERPA events into ATHENA readable events., http://atlas-sw.cern.ch/cgi-bin/viewcvs-atlas.cgi/offline/Generators/ReadSherpa_i/, 2007.

[62] TWIKI Monte Carlo Group ATLAS, SherpaForAtlas, https://twiki.cern.ch/twiki/bin/view/Atlas/SherpaForAtlas.

[63] T. Gleisberg, Sherpa v1.0.9, private communication, 2006.

[64] ATLAS Collaboration, *ATLAS Calorimeter Performance TDR* (ATLAS, 1997).

[65] ATLAS Computing Group, *ATLAS Computing TDR* (ATLAS, 2005).

[66] F. Derue and Serfon, ATLAS-PHYS-PUB-2005-016 (2005).

[67] T. I. Hollins, *SCT hybrid testing and the production of direct photons in the ATLAS experiment at the LHC*, PhD thesis, School of Physics and Astronomy, University of Birmingham, 2006.

[68] ATLAS Collaboration, Inner Detector Technical Design Report, Vol 1, 1997.

[69] U. Egede, *Ph.D. Thesis*, PhD thesis, Lund University, 1997.

[70] ATLAS collaboration, *ATLAS Muon Spectrometer TDR* (ATLAS, 1997).

[71] ATLAS, ATLAS muon spectrometer software.

[72] T. Lagouri *et al.*, Trans.Nucl.Sci. 51 , 3030 (2004), ATL-CONF-2003-011.

[73] D. Adams *et al.*, ATL-SOFT-2003-007 (2003).

[74] D. Adams *et al.*, ATL-SOFT-2003-008 (2003).

[75] D. Fassouliotis *et al.*, ATL-COM-MUON-2003-003 (2003).

[76] D. Adams, MuPerf TWIKI, https://twiki.cern.ch/twiki/bin/view/Atlas/MuPerf.

[77] ATLAS Collaboration, ATLAS Detector and Physics Performance Technical Design Report, Vol 1 - Chapter 9, 1999.

[78] D. Cavalli, ATL-PHYS-96-080 (1996).

[79] G. C. Blazey *et al.*, Run ii jet physics: Proceedings of the run ii qcd and weak boson physics workshop, 2000.

[80] R. Barlow, *Statistics: A Guide to the Use of Statistical Methods in the Physical Sciences* (Wiley, 2000).

[81] F. James, *MINUIT, Function Minimization and Error Analysis, Reference Manual*, Computing and Networks Division, CERN.

[82] J. Pumplin *et al.*, JHEP **0207**, 012 (2002).

[83] A. D. Martin, R. G. Roberts, W. J. Stirling, and R. S. Thorne, European Physical Journal C **28**, 455 (2003).

[84] S. Menke, (2007), arXiv:0706.1474 [hep-ex].